

METALTAIL



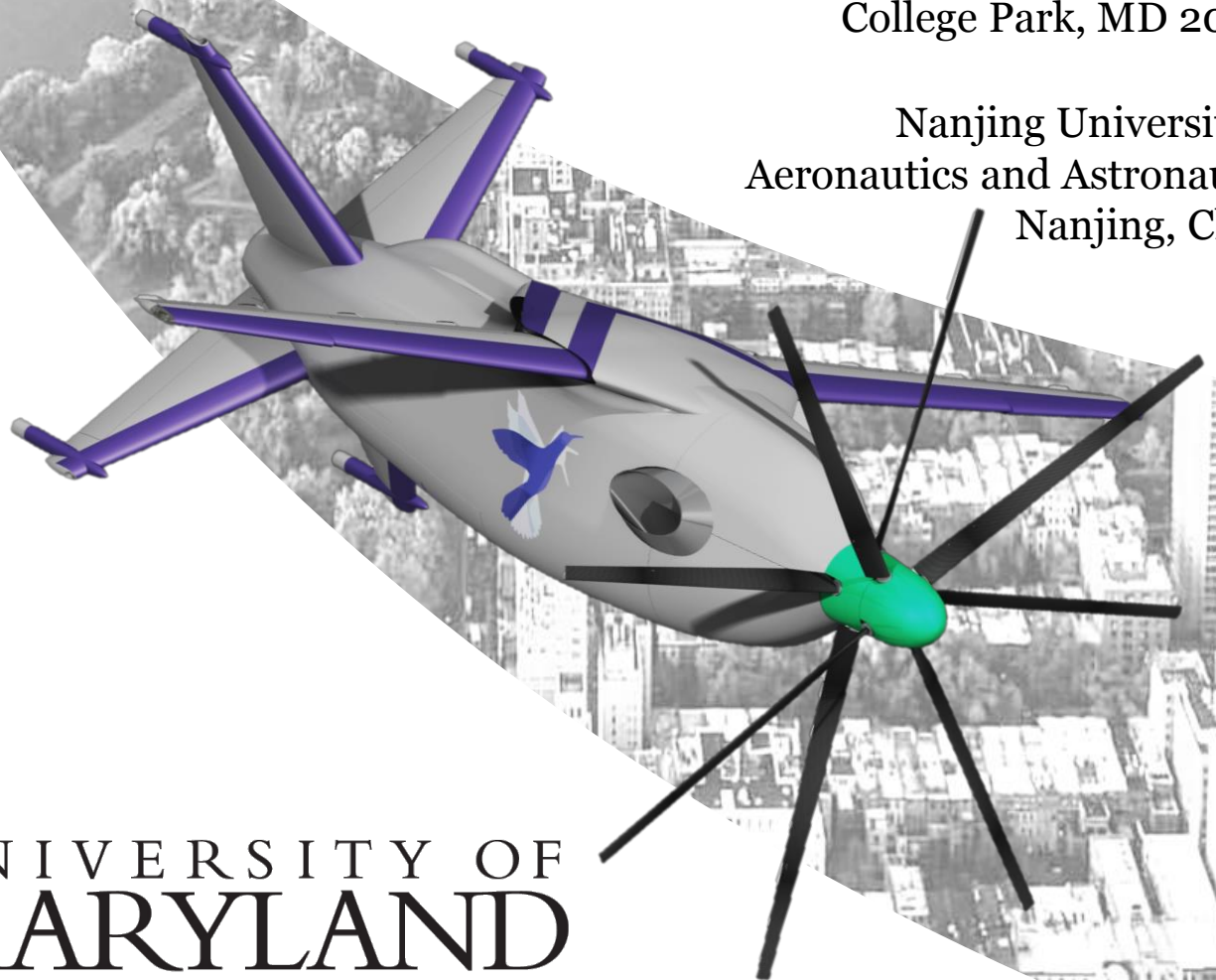
35th Annual AHS Student Design Competition

A Reconfigurable VTOL Aircraft

Sponsored by United States Army Research Laboratory

Alfred Gessow Rotorcraft Center
Department of Aerospace Engineering
University of Maryland
College Park, MD 20742

Nanjing University of
Aeronautics and Astronautics
Nanjing, China



UNIVERSITY OF
MARYLAND

ACKNOWLEDGEMENTS

The *Metaltail* design team wishes to acknowledge the following people for their invaluable discussion, guidance, and support throughout the course of this project.

University of Maryland Faculty

Dr. Inderjit Chopra – Alfred Gessow Professor and University Distinguished Professor, Director of Alfred Gessow Rotorcraft Center (AGRC), Dept. of Aerospace Engineering, University of Maryland, College Park

Dr. Vengalattore T. Nagaraj – Senior Research Scientist, Dept. of Aerospace Engineering, University of Maryland, College Park

Dr. Bharath Govindarajan – Asst. Research Professor, Dept. of Aerospace Engineering, University of Maryland, College Park

Dr. Anubhav Datta – Associate Professor, Dept. of Aerospace Engineering, University of Maryland, College Park

Industry Professionals

Dr. William Staruk – Research Scientist, STC, NASA Ames Research Center

Charley Kilmain – Manager, Mechanical Systems - H1 Program, Bell

Jillian Alfred – Supervisor, Handling Qualities, Bell

University of Maryland Personnel

Dr. Ashish Bagai

Dr. Vikram Hrishikeshavan

Dr. Ananth Sridharan

Stacy Sidle

Daniel Escobar

Tyler Sinotte

Bumseok Lee

Dylan Jude

Brent Mills

Peter Oas

Seyhan Gul

Yong Su Jung

Special thanks to:

Advanced Helicopter Concepts

Maryland State Police



Alfred Gessow Rotorcraft Center
Department of Aerospace Engineering
University of Maryland
College Park, MD 20742

Frederick Tsai
Graduate Student (Team Lead)
fredtsai.5@gmail.com

Eric Solomon
Graduate Student
esolomon1221@gmail.com

Chris O'Reilly
Graduate Student
chris@creativepracticality.com

Brandyn Phillips
Graduate Student
bphill@umd.edu

vklimche@umd.edu

Alexander Costenoble
Graduate Student
acstnbl@terpmail.umd.edu

Dr. Bharath Govindarajan
Faculty Advisor
bharath@umd.edu

Cheng Chi
Graduate Student (NUAA)
chi@umd.edu

Dr. Vengalatore Nagaraj
Faculty Advisor
vnagaraj@umd.edu

Dr. Inderjit Chopra
Faculty Advisor
chopra@umd.edu



Alfred Gessow Rotorcraft Center
Department of Aerospace Engineering
University of Maryland
College Park, MD 20740 U.S.A.

To the American Helicopter Society:

The members of the University of Maryland Graduate Student Design Team hereby grant AHS full permission to distribute the enclosed Executive Summary and Final Proposal for the 35th Annual Design Competition as they see fit.

Thank you,

The UMD Graduate Design Team

Contents

Acknowledgements	i
List of Figures	vi
List of Tables	ix
1 Introduction	1
2 Concept of Operations	3
2.1 Basis for Conceptual Operations	3
2.1.1 Organ Transportation	3
2.1.2 Rural Areas and Hospitals	4
2.2 Mission Profile	4
2.3 Multimission Capability	5
2.4 Maintenance	6
2.5 Storage and Long Distance Transportation	6
3 Configuration Selection	7
3.1 RFP Requirements	9
3.1.1 Voice of the Customer	9
3.1.2 Group 3 Similar Aircraft	10
3.2 Platform Reduction	10
3.2.1 Selection Criteria	11
3.2.2 Analytical Hierarchy Process (AHP)	12
3.2.3 Configuration Selection: Pugh Matrix	13
3.3 Fuselage Orientation	14
3.4 Reconfiguration Mechanisms	15
3.5 Configuration Convergence	19
3.5.1 Downwash Velocity	19
3.5.2 Geometric Constraint in Hover Configuration	21
3.5.3 Top Configuration Candidates	21
3.6 Final Configuration	22
4 Preliminary Vehicle Sizing	22

4.1	Sizing Mission	22
4.2	Design Drivers	23
4.3	Sizing Methodology	24
4.4	Parametric Study	25
4.4.1	Rotor Diameter	26
4.4.2	Rotor Aspect Ratio and Number of Blades	27
4.4.3	Tip Speed	28
4.4.4	Wing Sizing	28
4.5	Preliminary Sizing Results	29
5	Blade Aerodynamic Design	29
5.1	Design Goals	29
5.1.1	Blade Airfoil Requirements	30
5.2	Design Methodology	31
5.3	Blade Aerodynamic Design	32
5.3.1	Step 1: Baseline Blade	32
5.3.2	Step 2: Rotor RPM Variation	33
5.3.3	Step 3: Blade Taper Selection	33
5.3.4	Step 4: Blade Twist Selection	34
5.3.5	Step 4: Airfoil Selection	35
5.3.6	Final blade design	36
5.3.7	Coaxial Rotor Interference	38
6	Blade Structural Design	39
6.0.1	Blade Root Structure	39
6.0.2	Blade Internal Structure	40
6.0.3	Blade Manufacturing	41
6.0.4	Rotor Blade Sectional Properties	41
6.0.5	Aeroelastic Analysis	42
6.0.6	Ground and Air Resonance	43
6.0.7	Tip Clearance	43
6.0.8	CSD/CFD Analysis	44
7	Hub Design	45
7.1	Hub Selection	45
7.2	Hub Assembly	46
7.3	Swashplate Design	48
8	Propulsion System	50
8.1	Power Plant Design	50
8.1.1	Configuration Study	51
8.1.2	Turboshaft Engine Selection	52
8.1.3	Stuttgart Engineering STV 130 Turboshaft	53
8.2	Transmission Design	54
8.2.1	Configuration Study	54

.	54
8.2.2 Combining Coaxial Transmission	55
8.2.3 Gear Design and Analysis	56
Reduction Spur Gear Design	56
Bending Stress Analysis	57
Contact Stress Analysis	57
Split Power Bevel Gear Design	58
8.2.4 Gearbox Cooling and Accessories	59
Gearbox Cooling	59
Gearbox-powered Accessories	60
9 Wing Design	60
9.1 Wing aerodynamic Design	60
9.1.1 Planform Design	60
9.1.2 Airfoil Selection	61
9.2 Wing Structural Design	61
9.2.1 Internal Structure	62
9.2.2 Finite Element Analysis	62
9.2.3 Aeroelastic Analysis	63
9.3 Wing Sweep Mechanism Design	63
10 Airframe Analysis and Design	64
10.1 Airframe Aerodynamics	64
10.1.1 Fuselage Drag Area Estimation	64
10.1.2 CFD Analysis	65
10.2 Landing Gear	66
10.2.1 Oleo-Pneumatic Strut Sizing	66
11 Weight Analysis	66
12 Avionics System	67
12.1 Mission Requirements	67
12.1.1 Vehicle Design Budgets	69
12.2 Sensors	69
12.3 External Communications	71
12.4 Networking	71
12.5 Processors	72
12.6 Vehicle Systems Integration	73
12.7 Assured Autonomy	73
12.8 Controllability Requirements	73
12.9 Remote Human Pilot	74
12.10 Object Detection	74
12.10.1 Communication Modes	75
13 Health and Usage Monitoring System (HUMS)	75

14 Flight Dynamics and Controls	77
14.1 Flight Dynamics Model	77
14.1.1 Effect of Wing Sweep	78
14.2 Transitional Maneuvers	79
14.2.1 Transition Control Formulation	79
14.2.2 Takeoff and Hover Control	80
14.2.3 Transition Control Strategy	81
14.2.4 Hover-to-Cruise Transition	81
14.2.4.1 Climbing Hover-to-Cruise Transition	82
14.2.4.2 Level Hover-to-Cruise Transition	84
14.2.4.3 Effect of Hover-to-Cruise Transition Time	84
14.2.5 Cruise-to-Hover Transition	85
14.2.5.1 Climbing Cruise-to-Hover Transition	85
14.2.5.2 Level Cruise-to-Hover Transition	85
14.2.5.3 Effect of Cruise-to-Hover Transition Time	86
14.3 Control System	86
14.3.1 Autonomous Control and Navigation	88
14.3.1.1 Control	88
14.3.1.2 Path-Planning	88
15 Acoustics	88
15.1 FAA Noise Requirement	90
15.2 Noise Assessment	90
16 Vehicle Performance	91
16.1 Drag Estimation	92
16.1.1 Download Penalty	92
16.2 Hover Performance	92
16.3 Forward Flight Performance	93
16.4 Load Factor	95
16.5 Performance Metrics	95
17 Life-Cycle Cost Analysis	95
17.1 Aircraft Purchase Price	96
17.2 Direct Operating Cost	96
18 Summary	97

List of Figures

1.1	<i>Metaltail</i> performing transition on final approach in a megacity environment. . .	1
2.1	Time frame between organ recovery and transplant	3
2.2	Waiting list candidates by organ type in United States.	3
2.3	Critical access hospitals in the United States.	4
2.4	Mission Profile: Organ Transport	5
2.5	Modular and accessible design for easy maintenance and repairs.	6
2.6	<i>Metaltail</i> structural components without exterior skin.	7
2.7	Long distance transportation of 2.3 x 2.3 x 4.5 meter shipping crates.	7
3.1	Road map to configuration selection.	8
3.2	Vehicle catalog for configuration down-selection.	11
3.3	Relative ranking of key parameters through the Analytical Hierarchy Process (AHP).	13
3.4	Traditional fuselage orientation for takeoff and landing.	15
3.5	Tailsitter configurations.	16
3.6	Stopped rotor using a) Circulation control and b) mechanically control.	16
3.7	Tilt mechanisms for a) tiltrotor and b) tiltwing vehicles.	17
3.8	Sweep mechanisms on a) supersonic fighter and b) low speed oblique wing aircraft.	17
3.9	Folding mechanisms for a) wing and b) proprotor blades.	17
3.10	Extending mechanisms on a) rotor blades and b) wings.	18
3.11	Morphing mechanisms on a) rotor blades and b) wing flap.	18
3.12	Conceptual disassembling aircraft in Create The Future 2015 design contest.	19
3.13	Twenty potential configurations.	19
3.14	Disk loading vs. downwash velocities for existing VTOL denoted in black, VTOL designs for the RFP denoted in red.	20
3.15	Potential configurations reduced to ten.	21
3.16	Potential configurations reduced to five.	21
4.1	Sizing mission profile for medical transport.	23
4.2	Flowchart of the iterative sizing procedure.	24
4.3	Range of design points for the vehicle	25
4.4	Effect of varying rotor radius on vehicle properties	26
4.5	Effect of varying rotor properties on the takeoff mass	27
4.6	Effect of varying rotor tip speed on vehicle properties	28
5.1	<i>Metaltail</i> blade for both, the upper and lower rotor	30
5.2	Blade design process	31

5.3	Baseline blade efficiency comparison for cruise and hover	33
5.4	Effects of tip speed reduction on hover and cruise efficiency	34
5.5	Effects of taper on hover and cruise efficiency	34
5.6	Effects of bi-linear twist on cruise efficiency	35
5.7	Root airfoil selection.	36
5.8	Midspan airfoil selection.	37
5.9	Tip airfoil selection	37
5.10	Spanwise distributions on the <i>Metaltail</i> blade	38
5.11	Spanwise distributions on the <i>Metaltail</i> blade	38
5.12	Off-design performance of <i>Metaltail</i>	39
6.1	Rotor Blades	40
6.2	Anatomy of the blade root	40
6.3	Inner blade structure and materials	41
6.4	Sectional properties along the blade	42
6.5	Fan plots displaying frequencies at hover and cruise RPM	43
6.6	Aeroelastic Stability Boundaries	44
6.7	Tip clearance between upper and lower rotor blades	44
6.8	X3D analysis of rotor blade in hover	45
6.9	X3D analysis of rotor blade in cruise	45
6.10	X3D analysis of rotor blade root	46
7.1	Rotor hub assembly	47
7.2	Pitch horn and pitch link assemblies of each rotor	47
7.3	Bearing housing components clamp rotor blades to hub	48
7.4	Rotor load path through transmission gear housing	48
7.5	Swashplate assemblies	50
8.1	Approximate fuel + engine weight vs. cruise range (10 minutes total hover time)	52
8.2	STV 130 Turboshaft Engine	53
8.3	Gearbox section view	55
8.4	Power Splitting Spiral Bevel Gear Mesh	59
9.1	<i>Metaltail</i> wing planform (top view)	61
9.2	Finite element analysis of wing structure for <i>Metaltail</i>	62
9.3	Wing aerodynamic damping vs. forward flight velocity	63
9.4	<i>Metaltail</i> wing sweep mechanism actuator and linkages	64
10.1	Results from CFD analysis of isolated fuselage.	66
11.1	Center of gravity locations for <i>Metaltail</i>	68
12.1	Potential sensor choices categorized by usage	70
12.2	ARINC664 internal network design	72
12.3	YOLO Object Detection and Tracking	75
13.1	HUMS system architecture	76

14.1	<i>Metaltail</i> dynamics model.	78
14.2	Aerodynamic effects of sweeping the wing.	78
14.3	Phases of flight during one flight cycle.	79
14.4	Control of the vehicle in hover, climb, and transition.	80
14.5	Hover-to-cruise transition profiles.	81
14.6	Description of the climbing hover-to-cruise transition maneuver for $T = 42s$	82
14.7	Description of the level hover-to-cruise transition maneuver for $T = 42s$	83
14.8	Power variation with total maneuver time for different hover-to-cruise transition profiles.	84
14.9	Inbound transition profiles.	85
14.10	Description of the inbound climbing transition maneuver for $T = 75s$	86
14.11	Description of the inbound level transition maneuver for $T = 225s$	87
14.12	Power variation with total maneuver time for different cruise-to-hover transition profiles.	87
14.13	Deep Q-Learning control law generator and plant predictor.	89
14.14	Cycle of autonomous planning showing six-system environment model. Non-physical systems (green) are entirely software. Physical interfaces (red) transform software-generated data into physical movement. Dynamical system (yellow) is true physical motion. World model is a mapping of salient environment states.	89
15.1	FAA tiltrotor noise limits (Extrapolated from FAR 36.1103).	90
15.2	Noise levels for <i>Metaltail</i> in hover and cruise.	91
16.1	Effect of altitude and mass on hover performance.	92
16.2	Hover endurance variation with payload and altitude	93
16.3	Effect of speed on forward flight performance at 3000 m altitude.	94
16.4	Range and endurance achievable by <i>Metaltail</i>	94
16.5	<i>Metaltail</i> V-N diagram.	95

List of Tables

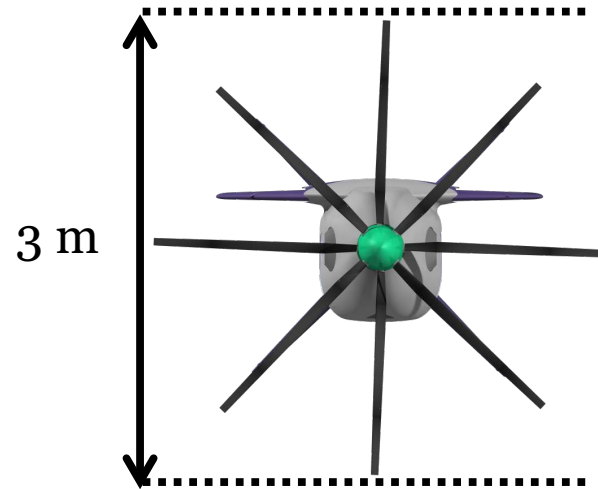
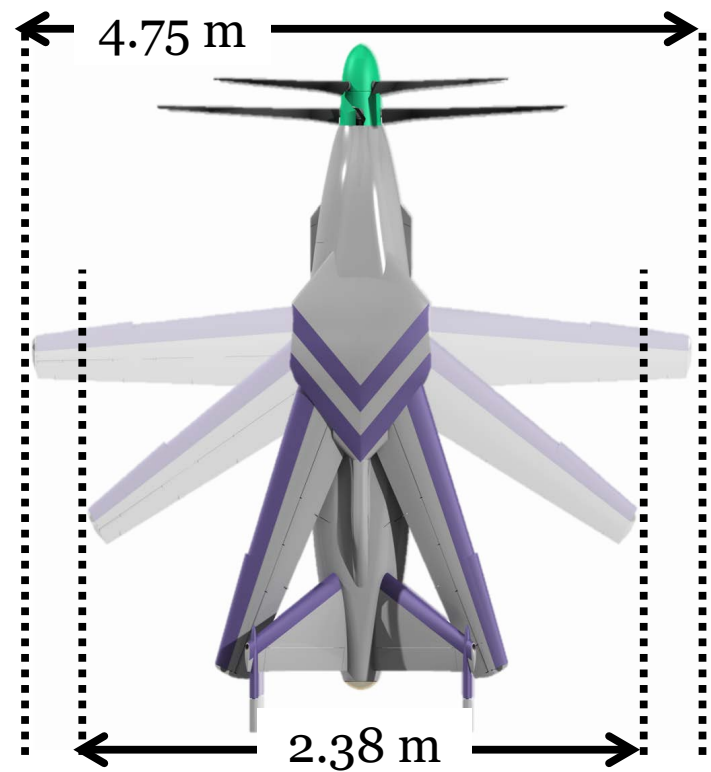
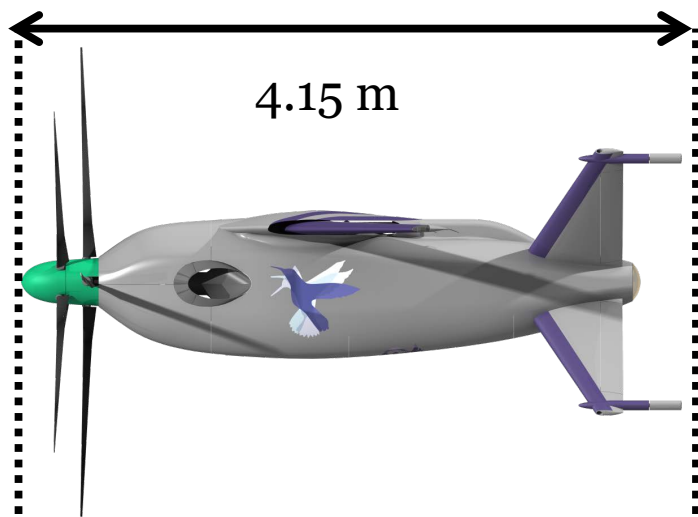
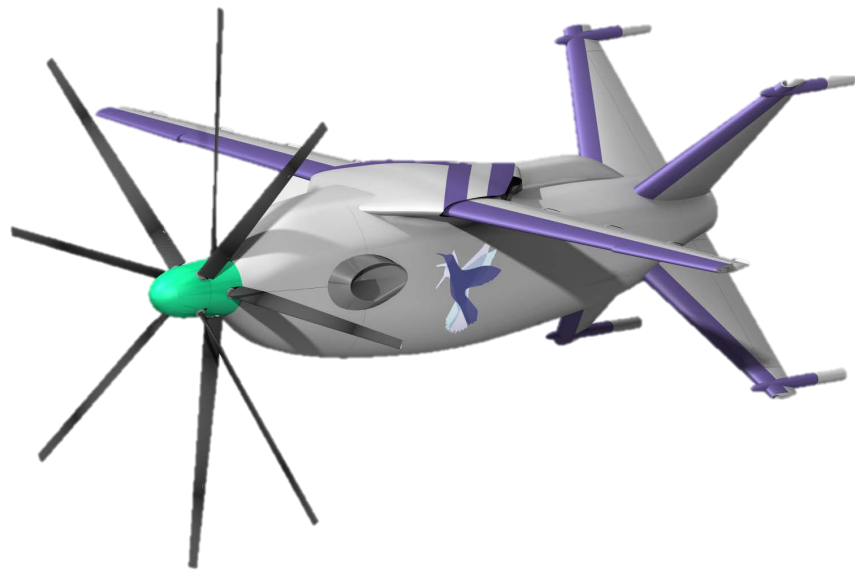
1.1	Overview of <i>Metaltail</i>	2
3.1	<i>Metaltail</i> comparison with Group 3-similar aircraft.	10
3.2	Parameter Weights from Analytical Hierarchy Process.	13
3.3	Pugh decision matrix shows the various rotorcraft platforms ranked against the weighted AHP criteria and final scoring.	14
3.4	Pugh decision matrix shows the various fixed wing platforms ranked against the weighted AHP criteria and final scoring.	14
4.1	Definition of the parameter space	26
4.2	Results of the sizing procedure	29
5.1	Rotor design specifications and flight conditions	30
5.2	Rotor design specifications and flight conditions	33
5.3	Power prediction comparison from BEMT and FVM analysis.	39
6.1	First five rotor frequencies at hover RPM	43
6.2	First five rotor frequencies at cruise RPM	43
7.1	Hub Selection	46
7.2	Swashplate Selection	49
8.1	Comparison of turboshaft engine options for the <i>Metaltail</i>	52
8.2	Reduction Spur Gear Geometry	56
8.3	Bending Stress Analysis Factors and Margins	57
8.4	Contact Stress Analysis Factors and Margins	58
8.5	Spiral Bevel Gear Geometry	59
11.1	<i>Metaltail</i> Weight Estimates	67
12.1	Avionics Design Specifications	69
12.2	Sensors Design Specifications	71
12.3	External Communications Design Specifications	71
12.4	Networking Design Specifications	72
12.5	Estimated processor required instructions per second (IPS)	72
12.6	Processors Design Specifications	73
12.7	Maximum allowable latency of avionics subsystems	74

12.8	Maximum allowable latency of avionics subsystems. Inertial estimates based off of typical pose filter rates. Actuator response and object detection bottlenecked by pose estimation. Path refactoring based off of typical values for human response while piloting UAV. Health monitoring bottlenecked by plan refactoring.	74
12.9	Data Rate Budget	74
12.10	Data Rate Budget. Estimates shown for 12 GNSS/IMU states, 20 filter states, 20 system health states. Allowed offboard stream rates reflect average upload rates for east coast US cities (2017, SpeedTest).	74
15.1	Maximum noise level on the ground plane, 150 meters below the aircraft.	91
16.1	Summary of <i>Metaltail</i> airspeeds at 3000 m altitude.	95
16.2	Summary of <i>Metaltail</i> performance metrics.	96
17.1	Parameters used to calculate aircraft purchase price.	97
17.2	Parameters used to calculate direct operating costs per year.	97

***Metaltail* Requirements and Compliance**

Mission Profile Compliance	Design Solution	Section
Group 3 unmanned VTOL	<i>Metaltail</i> weights 556 kg (under the required 600 kg), is unmanned, and demonstrated excellent hover capabilities.	3, 13
Main lifting device must be a reconfigurable system	Coaxial rotor is main lifting device in hover configuration with wings stowed. Wings swing out with respect to body axes to provide lift in forward flight.	9.3, 14.1
Vehicle must reconfigure on its own	An electric motor turns a leadscrew to actuate the wing extension and retraction.	9.3
Reconfiguration must be reversible	The motor which turns the leadscrew may operate in either direction.	9.3
Reconfiguration must be able to take place during ground operations	The power of the wing extension mechanism is sufficient to overcome the weight of the wings. Swinging the wings does not cause any instability from CG shift.	9.3
Reconfiguration must be able to take place during flight	The power of the wing extension mechanism is sufficient to overcome the aerodynamic force acting on wings. Swinging the wings does not cause control instability from CG or center of pressure shift.	9.3, 14.1
No part of the vehicle can be removed or jettisoned	No parts are removed or jettisoned during flight, as seen by weight analysis breakdown.	13
Aircraft must be controllable and stable at all times including transition period	Control schemes can trim aircraft during transition, as well as mitigate gusts.	14.2
Design should be new and novel	Swing wings were largely abandoned in the late 1970s. Swing wings from this period focused on drag reduction at high Mach number, while mitigating center of pressure shift. However, <i>Metaltail</i> uses the shift in the center of pressure to increase control authority, in addition to meeting geometric constraints.	1, 3
Any powerplant and fuel type may be used, provided it meets technology limitations	A real engine with TRL 6 is used in <i>Metaltail's</i> design.	8.1
Be able to operate in a megacity-type environment	Operation between city environments is incorporated into <i>Metaltail's</i> mission profile.	2.2
In hover configuration, maximum horizontal dimension is limited to no more than 3 meters	<i>Metaltail</i> in hover configuration fits within a 3 meter diameter cylinder, to provide clearance and control response between closely spaced tall buildings.	3-view foldout
Maximum gross takeoff weight is 600 kg	<i>Metaltail's</i> MTOW is 556 kg	13
Operating altitude of 3000 meters standard atmosphere	<i>Metaltail</i> is able to hover at 3100 meters standard altitude, and cruise at higher altitudes.	16.2
Maximum airspeed greater than 333 kph (180 kts)	<i>Metaltail's</i> maximum airspeed varies from 454 kph at SLS to 511 kph at 3000 m, well above the lower limit of 333 kph.	16.3
Can carry minimum of 100 kg payload	<i>Metaltail</i> is designed for a mission requiring a 100 kg payload and 100 kg fuel, for a total useful load of 200 kg.	4.1, 16.3

Documentation Requirement Compliance	Section
Vehicle Configuration Trade Studies	3.2, 3.5
Description of Reconfigurable Systems	
a) Comparison with Traditional Systems	3.1.2, 3.4
a) Transition Phase	14.2
c) Performance Metrics	16.5
Vehicle Weight Breakdown	13
Estimation of Parasitic Drag	10.1
Aeromechanical Analysis of Rotor	6.1.5-6.1.8
Analysis of Rotor Dynamics	5.3
Structural Load Analysis	6.1.8, 7, 9.2-3, 10.2
Performance Calculations	16
CONOPS	2
Additional Graduate Student Tasks:	
a) Stress Analysis & Fatigue Substantiation	6.1.8, 7, 9.2-3, 10.2, 16.4
b) Aeroelastic Stability Boundaries	6.1.5
c) Flight Control & Reconfigurability	14



1 Introduction

Since the first practical helicopter achieved the dream of powered vertical takeoff and landing (VTOL) in the 1930s, inventors and engineers have sought to push the forward flight envelope of VTOL aircraft to higher speeds. While modern helicopters have become sleeker and lighter, aerodynamic limitations of rotors in edgewise flight have kept rotorcraft from achieving the forward flight speeds of their fixed-wing counterparts. From these roadblocks, came the advent of compound rotorcraft in the 1950s, which combined rotor systems with features of fixed-wing aircraft, such as wings and propulsors (Piasecki 16H-1 Pathfinder). However, compound rotorcraft, by design, have separate lift and propulsion systems that trade off efficiencies for each flight mode, which decreases the overall efficiency of such vehicles. At the same time, investigations were carried out on reconfigurable vehicles that could use their main lifting device(s) in multiple flight modes, such as tiltwing (Vertol VZ-2) and tiltrotor (Bell XV-3) concepts. However, these reconfigurable concepts faced challenges due to insufficient technology maturity at the time. It has only been within the past thirty years that advancements in physical and digital technologies have allowed these reconfigurable designs to be realized.

Pursuant to these improvements, the *2018 AHS Student Design Competition* Request for Proposal (RFP) sponsored by the U.S. Army Research Lab calls for a reconfigurable autonomous vehicle in the Group 3 designation of Unmanned Aerial Vehicles (UAVs) suitable for operation in megacity-type environments. This RFP draws on the imagination and innovation of the 1970s/1980s era Sikorsky S-72/NASA Rotor Systems Research Aircraft (RSRA) and the DARPA/Lockheed X-Wing circulation control rotor. Though the RSRA/X-Wing configuration never flew, the vision of reconfiguring major systems to achieve efficient performance in hover and forward flight inspires the University of Maryland design solution.

Through innovative design and harnessing proven technology growth in materials, controls, avionics, and propulsion systems, the University of Maryland Graduate Student Design Team proudly presents *Metaltail*, a tailsitter configuration with a coaxial hingeless rotor and swing wings. *Metaltail* offers unprecedented speed for VTOL-capable UAVs and multi-mission capability. Named after a group of Peruvian high-altitude hummingbirds in the genus *Metallura*, *Metaltail* is designed such that its reconfigurable swing wings are the driving feature that enables the vehicle to transition from hover to forward flight and vice versa. Much like the RSRA/X-Wing vehicle, *Metaltail* aims to demonstrate the efficacy of current technology to enable transitions between hover and high-speed forward flight through reconfigurable systems.

The design philosophy focused on controllability of the aircraft in all flight conditions,

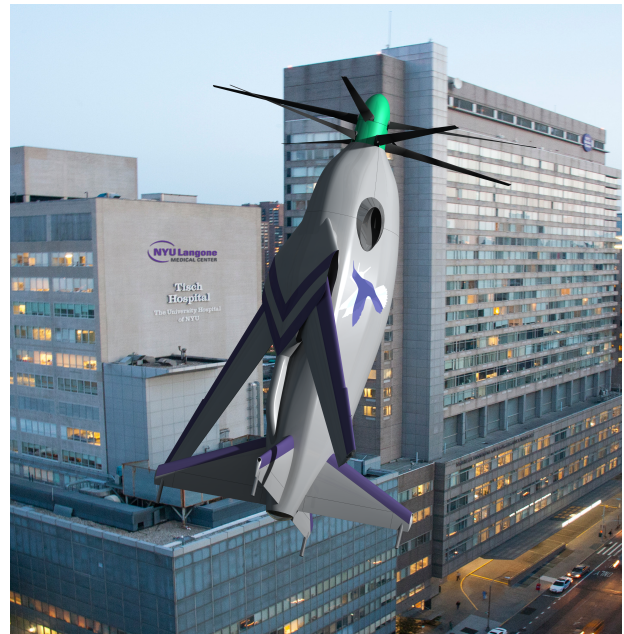


FIGURE 1.1: *Metaltail* performing transition on final approach in a megacity environment.



emphasizing safe operations for megacity missions, and using newly developed technologies to obtain unprecedented performance. This approach resulted in *Metaltail*, a 552 kg autonomous UAV capable of carrying 110 kg of payload up to 900 km within 2.5 hours with a max speed of 445 km/h.

This report will outline the methodology used to arrive at the final configuration, as well as highlight the features of the vehicle that elevate its performance over any fixed-configuration system. An overview of *Metaltail* features is shown in Table 1.1.

TABLE 1.1: Overview of *Metaltail*

Features	Summary
Unique Coaxial Hub	<i>Metaltail's</i> coaxial hingeless hub is uniquely designed with the upper swashplate located inside the rotor shaft for space and weight reduction.
Efficient Proprotor	Using bilinear twist and three distinct blade airfoils along the radius, <i>Metaltail's</i> rotors perform exceptionally in both hover and forward flight modes with a Figure of Merit (FM) of 0.77 and propulsive efficiency of 0.83.
Twin Diesel Turboshaft Engines	<i>Metaltail's</i> two state-of-the-art turboshaft engines run on diesel, reducing costs and increasing utility, providing 260 horsepower flat-rated up to 9,144 meters.
Coaxial Transmission	Adhering to American Gear Manufacturers Association (AGMA) standards, <i>Metaltail's</i> transmission is a coaxial output combining gearbox.
Swing Wing Mechanism	<i>Metaltail's</i> wing sweep range of 68° assists in transition maneuvers from hover to high-speed forward flight and in reverse. Offers a geometric advantage by decreasing footprint in hover configuration for mega-city operations.
Modular Multi-mission Payload	<i>Metaltail's</i> payload compartment is removeable and offers customized payload packages for multi-mission capability.
Reliable Autonomy	<i>Metaltail's</i> guidance, navigation, and control (GNC) system uses nonlinear stochastic control theory with baseline avionics assembled from off-the-shelf (OTS) products for best value and serviceability.
X-Tail Configuration	<i>Metaltail's</i> tailsitter configuration rests on a titanium X-tail with shock-absorbing oleo struts as the landing gear.



2 Concept of Operations

It is important to develop a thorough understanding and appreciation for *Metaltail's* operations, starting with its primary mission to various operations both during flight and on the ground, as well as inspection, maintenance, and handling. It is also prudent to consider any regulations that may restrict *Metaltail's* operations. As there are currently no well-defined autonomous UAV regulations, *Metaltail* meets the regulations set forth by the Federal Aviation Administration (FAA) requirements of FAR 23 for normal airplanes and FAR 27 for normal helicopters, which broadly constrain vehicle design limits and operational limits.

2.1 Basis for Conceptual Operations

2.1.1 Organ Transportation

In the United States, since 1988, 683,000 organ transplants have been performed; however, 8,000 deaths occur every year in the United States because organs cannot be transported in a timely manner[1]. Figure 2.1 shows that viable organs have a very small window of time before degradation prevents their use. As of May 2018, 114,726 people are in need of a lifesaving organ transplant as shown in Figure 2.2. Typical modes of delivery are loosely based on distance: ground transportation within 80 km, rotorcraft up to 320 km, and fixed-wing aircraft for over 320 km. *Metaltail's* maximum speed of 445 km/h can both cover the ground transportation range and double the rotorcraft range for deliveries. With its advanced autonomous systems, *Metaltail* reduces the need for human pilots to operate during nighttime or degraded visual environment, both decreasing the risk to pilots and increasing the number of deliveries. With *Metaltail's* high speed and autonomous navigation, packages can be delivered quickly and safely with high reliability.

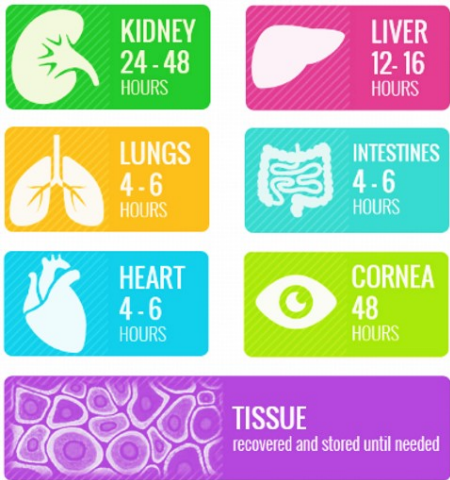


FIGURE 2.1: Time frame between organ recovery and transplant

Organ	Candidates
Kidney	95,139
Liver	13,949
Pancreas	882
Kidney / Pancreas	1,661
Heart	3,997
Lung	1,432
Heart / Lung	50
Intestine	245
Total	114,726

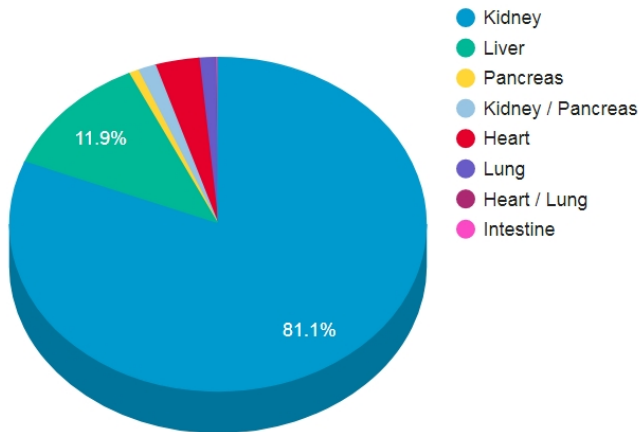


FIGURE 2.2: Waiting list candidates by organ type in United States.



2.1.2 Rural Areas and Hospitals

Citizens in difficult-to-access rural areas depend on critical access hospitals (CAH) to serve their medical emergency needs. The criteria for a hospital to be a CAH are: (1) must be over 56 km from another hospital, (2) must be over 24 km from another hospital in mountainous terrain or areas with only secondary roads, (3) must possess at most 25 inpatient beds, (4) must provide 24-hour emergency services with medical staff on-site or on-call. Shown in Figure 2.3, as of 16 April 2018, there are 1,346 CAHs in the United States.

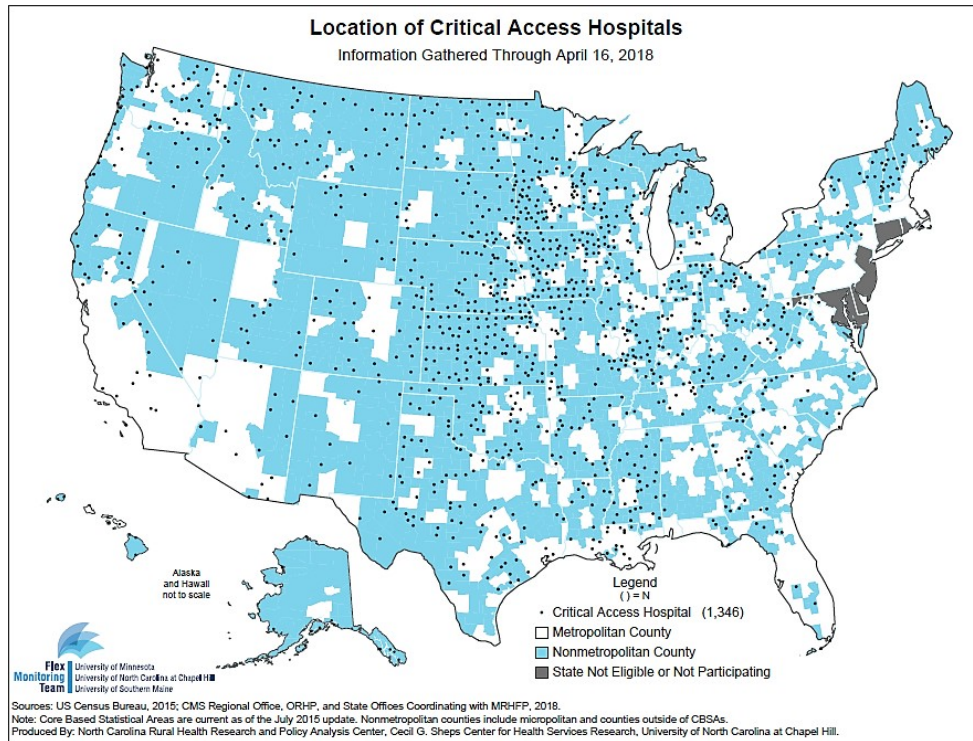


FIGURE 2.3: Critical access hospitals in the United States.

CAHs often have logistical difficulty with blood products. Blood is expensive and it expires - platelets and thawed plasma last only five days. The smallest CAHs stock just two to six units (one to three liters) of red blood cells and no frozen plasma or platelets. Consequently, a single patient with massive bleeding can deplete the blood supply. These difficulties coupled with inaccessibility of the area results in higher mortality rates compared to non-CAHs. With *Metaltail's* payload capacity of 110 kg, it can carry 200 units of blood including the specialty storage containers designed for temperature, pressure, and humidity control. *Metaltail* can be used to transport blood products from major medical facilities with ample supplies to CAHs, mass casualty scenes, and offshore ships with passengers in need of critical care.

2.2 Mission Profile

Metaltail is a VTOL platform with omnidirectional maneuverability in hover with superior forward flight capabilities as compared to contemporary platforms. Its capabilities allow for safe takeoff and landing in a mega-city environment. The main mission prescribed for *Metaltail* is an organ transport mission from a megacity to a regional hospital 370 km away.



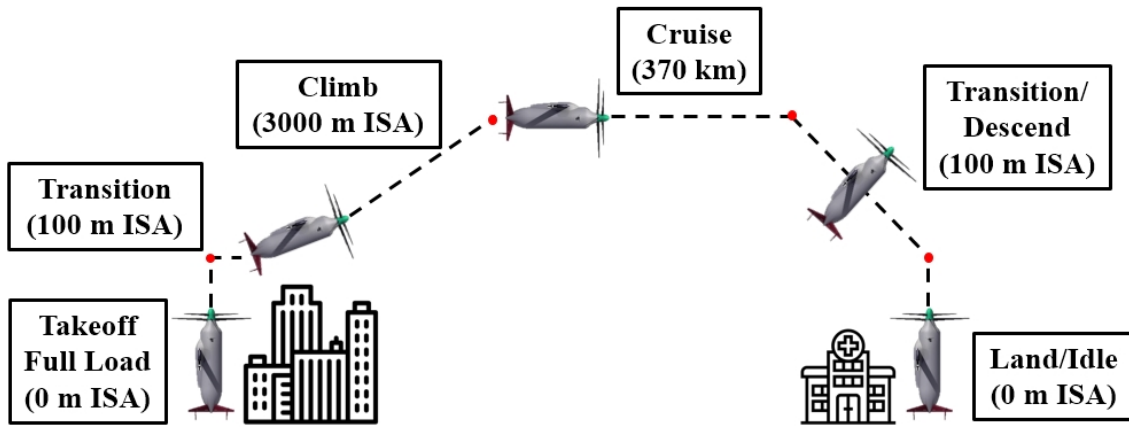


FIGURE 2.4: Mission Profile: Organ Transport

2.3 Multimission Capability

As a reconfigurable aircraft, *Metaltail* is designed for both efficient hover and high-speed forward flight; therefore, the mission capability of *Metaltail* can be expanded to include hover-specific missions, low speed missions, and high-altitude missions up to 5000 m mean sea level (MSL). *Metaltail's* removeable payload bay expands its capabilities even further with the ability to attach an additional 70 liter fuel tank and various payload packages. With an additional 70 liters of fuel, *Metaltail's* hover endurance increases by 2 hours and cruise endurance increases by 3 hours. For detailed information of payload bay design and operation, refer to Section 5.11.

Metaltail could perform the following are missions better than current aircraft designs:

- **Monitoring:** Helicopters are commonly used for surveillance such as traffic congestion, law enforcement pursuit, disaster monitoring, and other emergencies. With an interchangeable suite of sensors and cameras as well as attachable auxiliary fuel tanks, *Metaltail* is capable of providing exceptional monitoring services at greater endurance for cityscapes. Airplane mode can also be leveraged for high-altitude and/or high-speed reconnaissance missions.
- **Maritime Search and Rescue:** *Metaltail* can provide up to XX hours of support for maritime emergency operations in day or night conditions. Whether *Metaltail* is taking off from shore or from a carrier, its speed and endurance will allow for a large search area and once persons are located, *Metaltail's* communication systems can guide pilots for extraction. *Metaltail* can carry life jackets or flotation devices and drop them for casualties in the water.
- **Survey Services:** *Metaltail* would excel at missions requiring data collection and surveying. Global system mapping of terrain or atmospheric data collection at high altitudes require specific cameras and data collection systems to be on the aircraft, which exploits *Metaltail's* strength of payload flexibility.
- **Communications Relay:** *Metaltail* can bridge the gap between communication systems limited by line-of-sight (LOS) by creating a new LOS path. Multiple *Metaltail* vehicles can act as linking points and relay communications up to far greater range and around obstacles.



- **Urban Firefighting:** For urban environments, high-rise buildings and skyscrapers are particularly at risk of uncontrolled blazes. Fire engines and first responders may not have quick and safe access to the upper floors of a tall building. *Metaltail*, with its fast deploy time, small geometric footprint, and hover capabilities, can be first on the scene launching and dropping fire extinguishing grenades to suppress the fire while first responders prepare their measures.

2.4 Maintenance

As with all vehicles, regularly scheduled maintenance and any unscheduled maintenance will be required to keep *Metaltail* working in peak condition. All tools, fasteners, and fittings used for the vehicle are industry standard components for convenience. Figure 2.5 displays the maintenance setup and the location of hatches to the internal areas of the engine, the payload bay, and the avionics compartment in the tail.

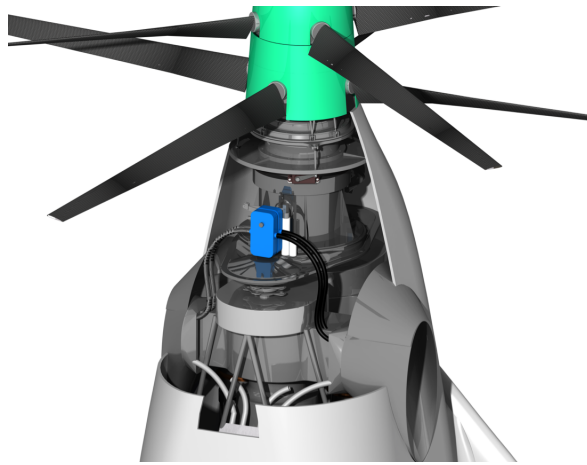


FIGURE 2.5: Modular and accessible design for easy maintenance and repairs.

The upper and lower spinners are removable to allow the maintenance crew to work on the rotors, if necessary. To slide the lower spinner off the nose, the upper rotor blades must first be removed by unbolting the upper rotor hub component clamping down the blade root sleeve. The lower rotors can also be removed by the same procedure if replacement or repair is needed. To access the servo motors below the lower swashplate, the mechanic must approach the area through the engine hatch.

The swing wing mechanism can be accessed for maintenance and repair by removing the fairing covering the wingbox. The wingbox and wings can be detached from the fuselage by removing the bolts fastening the wingbox to the airframe as shown in Figure 2.6.

2.5 Storage and Long Distance Transportation

Metaltail is designed such that the fully assembled aircraft can fit in a $2.3 \times 2.3 \times 4.5$ meter shipping crate and be loaded into a semi-trailer truck or a B747-8F freighter aircraft. For a standard 48 foot freight trailer, three *Metaltail* vehicles can fit end to end in custom shipping containers on pallets; for B747-8F aircraft, 22 crates can fit in the main cargo hold as shown in Figure 2.7. All shipped vehicles will have instructional booklets included.



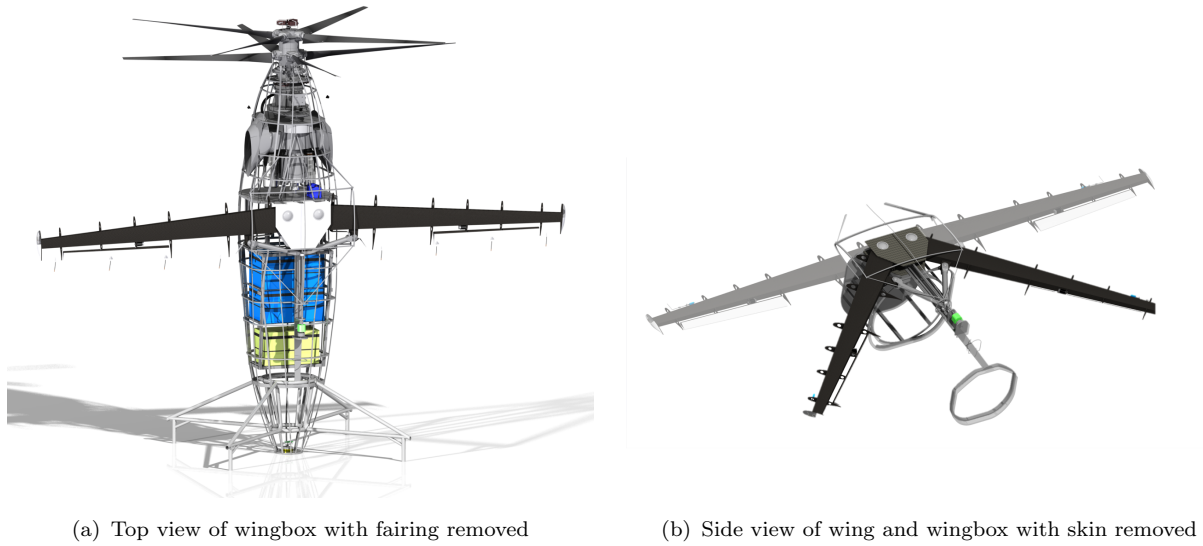


FIGURE 2.6: *Metaltail* structural components without exterior skin.

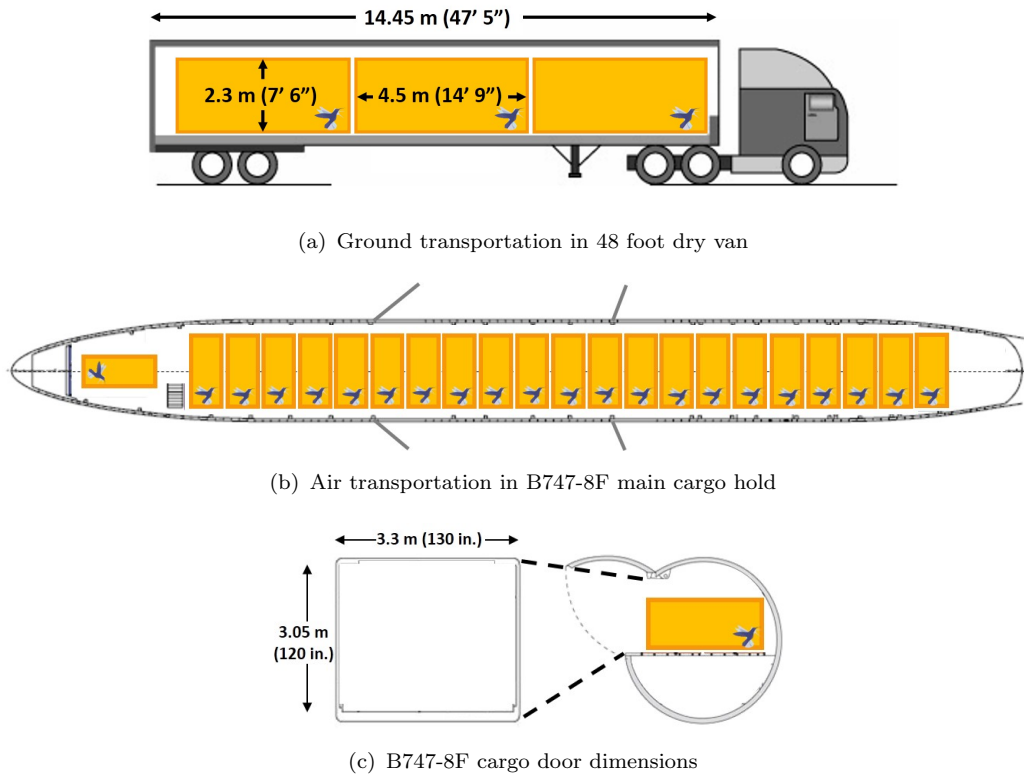


FIGURE 2.7: Long distance transportation of 2.3 x 2.3 x 4.5 meter shipping crates.

Metaltail's blades must be prepared for loading by setting each rotor to the same phase as the X-tail fins. This allows for the blades to fit diagonally into the freight container. *Metaltail* will lie on a custom wood frame, which will keep the vehicle secure during transportation. Hard points along the fuselage can be used to lash down the body and keep it from shifting axially.



3 Configuration Selection

Metaltail, a coaxial, swing wing, tailsitter aircraft, was carefully designed with speed, range, safety, and reliability in mind. Using a top-down design approach, the major components of the configuration was settled first, then each component and its subcomponents underwent further refinement. The road map in Figure 3.1 provides an overview of this top-level, first-order process, and this chapter explains the logic behind each of the steps taken to arrive at the final configuration.

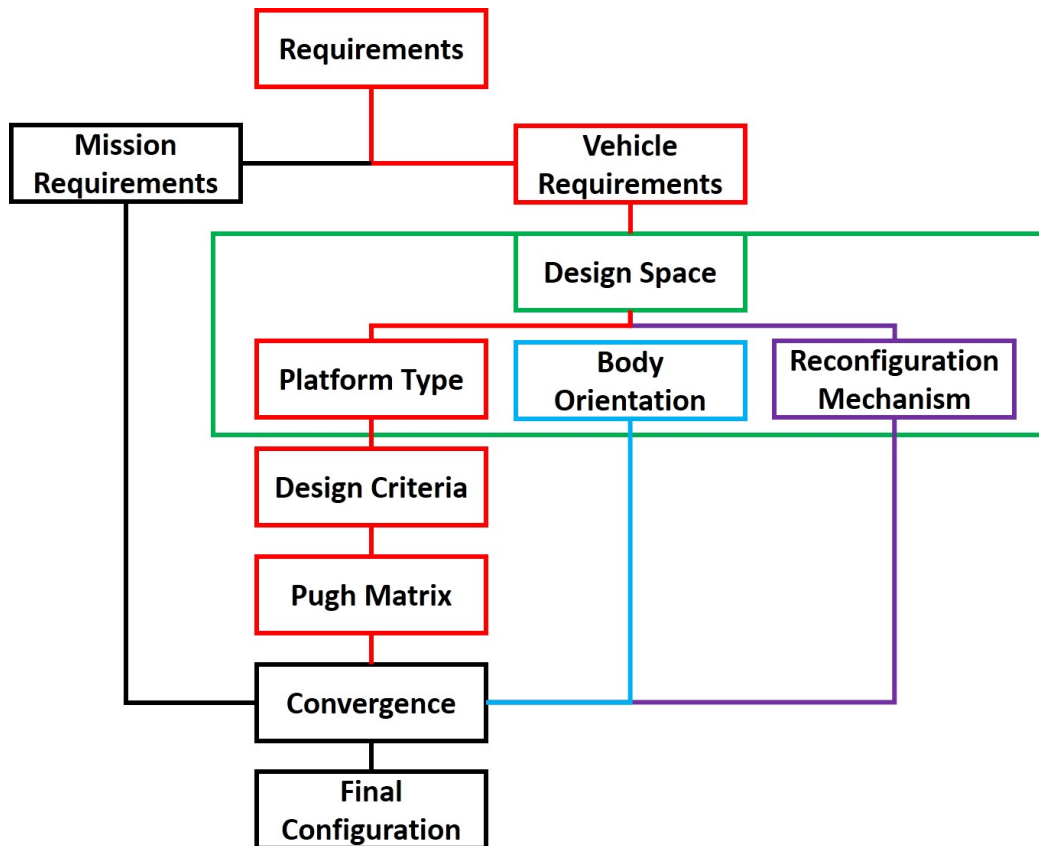


FIGURE 3.1: Road map to configuration selection.

Beginning with the requirements of the RFP, the path splits into vehicle requirements and mission-related requirements, defined in Section 3.1.1. The green box encloses the entire design space, which are the variables that are studied and eliminated if they do not satisfy requirements. The design space encompasses vehicle platform type, body orientation, and reconfiguration mechanisms. The red path denotes how the rotorcraft and fixed-wing platforms were narrowed down to a select few candidates, described in Section 3.2. The blue path is the body orientation design space, traditional or tailsitter orientations, defined in Section 3.3. The purple path defines the reconfiguration mechanisms design space, explained in Section 3.4. The path track is the mission requirements of the RFP that constrains the final candidates of the configuration. All the paths converge to obtain the final configuration, presented as *Metaltail*.



3.1 RFP Requirements

3.1.1 Voice of the Customer

To achieve a feasible and superior design, the requirements must first be thoroughly understood as the voice of the customer, which guides the design process and ensures a customer-centric final product. This section presents the RFP requirements, divided into vehicle and mission requirements, analyzes the meaning and how *Metaltail* meets the requirement. Note that while all the requirements in the RFP are defined, not all are essential for first-order configuration selection.

The vehicle requirements are:

- **Main lift device must be reconfigurable:** The vehicle is required to reconfigure its main lifting device by changing shape, orientation, or location relative to a body fixed frame. A standard compound aircraft with fixed lifting devices will not be acceptable. *Metaltail's* swing-wing mechanism satisfies this requirement.
- **Reconfigurable system must be a key feature:** The reconfigurable system must be a fundamental element of the vehicle, not simply an enhancement. Section 5.11 fully articulates the function of *Metaltail's* swing-wing system.
- **Reconfigurable system must be reversible, able to be executed multiple times without support, and take place during both ground operations and flight:** *Metaltail's* wings can be swept up to 68° while on the ground and across all flight modes. This actuation is fully reversible and repeatable.
- **Maximum airspeed of 333 km/h (180 knots) or greater:** Requires the vehicle to have a low drag area in forward flight. A streamlined fuselage with few interference drag components and single propulsive device would be preferred for high speed flight, which favors a monoplane platform. *Metaltail* meets this requirement with a maximum speed of 445 km/h.
- **Max gross takeoff weight (MGTOW) limited to 600 kg:** The Department of Defense (DoD) classifies a Group 3 UAV as MGTOW greater than 55 kg, but less than 600 kg. It specifies normal operating altitude under 5,500 m and maximum speed less than 463 km/h. However, per the RFP speed requirement, the configuration is not bound by the Group 3 classification for maximum speed. *Metaltail* has a total gross take off weight of 552 kg. *Metaltail's* weight breakdown can be found in Section 5.11 and comparisons to aircraft similar to the Group 3 classification are found in Sec. 3.1.2.
- **Payload capacity of 100 kg or greater:** At a minimum, the vehicle is required to carry 1/6th of its max weight limit. *Metaltail* can carry up to a 110 kg payload. Carrying capacity affects fuselage size, CG placement, and airframe design. Section 5.11 contains payload bay design and payload integration.
- **Operating altitude of 3000 meters standard atmosphere:** This constraint determines the amount of power necessary to have the vehicle operate at 3000 meters. Space for the powerplant factors into the vehicle design.



- **Any powerplant or fuel may be used provided it meets technology limitations:** *Metaltail* uses two newly developed yet flight-tested Stuttgart STV130 engines powered with Diesel fuel. More information on the powerplant is contained in Sec. 8.

For mission requirements:

- **Ability to operate in a megacity-type environment:** This introduces precise geometric clearances due to narrow city streets and confined spaces as well as noise considerations, gust tolerance, and extra safety measures. Vehicle size is limited to 3x3 meter square when in hover configuration. These constraints limit the ability of the vehicle to perform in other spaces, such as open airspace. Section 3.5.1 explains why this requirement bounds the vehicle design.
- **Aircraft must be controllable and stable at all times including transition period:** For the operation of *Metaltail*, no tumbling maneuvers are performed. More on the transition and controls can be found in Ch. 14.

3.1.2 Group 3 Similar Aircraft

Table 3.1 displays a brief overview of aircraft that are similar to Group 3 vehicle weight class and a comparison of their characteristics to *Metaltail's* attributes.





Metaltail		TigerShark Block 4 UAV		R22 Helicopter		Pipistrel Panthera	
							
Span	4.75 m	Span	6.55 m	Rotor Diameter	7.67 m	Span	10.86 m
Length	4.1 m	Length	4.57 m	Length	8.74 m	Length	8.07 m
Empty Weight	300 kg	Empty Weight	113 kg	Empty Weight	399 kg	Empty Weight	815 kg
MTOW	552 kg	MTOW	272 kg	MTOW	635 kg	MTOW	1,315 kg
Useful Load	252 kg	Useful Load	159 kg	Useful Load	236 kg	Useful Load	500 kg
Top Speed	445 km/h	Top Speed	222 km/h	Top Speed	188 km/h	Top Speed	407 km/h

TABLE 3.1: *Metaltail* comparison with Group 3-similar aircraft.

Metaltail is the smallest by dimension, possesses a top speed twice the speed of an R22, and ranks second in useful load (fuel and payload) to Pipistrel Panthera, which is twice *Metaltail's* weight.

3.2 Platform Reduction

Metaltail is a merger between a coaxial rotorcraft and a monoplane fixed-wing, combining the hover efficiencies of the coaxial rotor with the speed of a monoplane. This section reviews the process of converging to *Metaltail's* configuration platforms. In the design space, the different aircraft platforms, namely rotorcraft and fixed-wing vehicles, are organized as shown in Figures 3.2(a) and 3.2(b). These two platforms are the basic models of aircraft: rotorcraft combines lift and propulsion in one device while fixed-wing aircraft generates them separately.





FIGURE 3.2: Vehicle catalog for configuration down-selection.

Using the Analytical Hierarchy Process (AHP) to organize and prioritize RFP design parameters, a qualitative understanding of configuration down-selection parameters was established. A Pugh decision matrix was implemented that ranked each of the platforms in the design space. From those rankings, two rotorcraft (single rotor, coaxial rotor) and five fixed-wing platforms (monoplane, delta wing, tandem wing, biplane, and box wing) were selected and further down-selection (Sections 3.3, 3.4, 3.5) was performed by incorporating mission requirements and the inputs from body orientation and reconfiguration mechanism.

3.2.1 Selection Criteria

From analysis of the RFP and design requirements of megacity operations, fifteen key criteria were determined to be vital for configuration selection. They were prioritized in an Analytical Hierarchy Process (AHP) matrix to use in configuration comparisons. These criteria are defined below, in alphabetical order.

- **Controllability:** Effectiveness in disturbance rejection and stability in flight modes.
- **Cost:** Total cost over the vehicle's life cycle from designing, manufacturing, and operation to environmental impacts.
- **Cruise Speed:** Either velocity for best range or velocity for best endurance. High lift-to-drag ratio would improve this speed.
- **Durability:** Ability to withstand wear from normal operating conditions and continue to function. A measure of lifespan, high durability directly increases operational life.



- **Empty Weight Fraction:** Ratio of vehicle weight, excluding fuel and payload, to overall total weight, where the lower the fraction, the more fuel or payload can be carried.
- **Footprint:** A geometric measure of the vehicle, as projected vertically onto the ground, used to guide solutions for 3x3 meter hover constraint in RFP.
- **Hover Altitude:** The maximum height at which the vehicle can perform hover.
- **Hover Endurance:** The amount of time the vehicle can perform hover at 3000 meters per the RFP.
- **Max Speed:** Maximum level flight velocity as allowed by vehicle profile and power availability.
- **Noise:** Auditory disturbances emanating from the vehicle's propulsion systems, which can cause annoyance to bystanders in megacity environments.
- **Payload:** Larger carrying capacity of vehicle than the minimum requirement of 100 kg.
- **Range:** Maximum distance the vehicle can travel between takeoff and landing, limited by fuel capacity.
- **Reliability:** An assessment of vehicle subsystems' probability of failure over a given operational period.
- **Safety:** The vehicle's capability to actively or passively ensure the safety of the public should any components or systems fail.
- **Technological Maturity:** Qualitative assessment of the vehicle's inherent barriers that necessitate further development. Technology maturity is quantified by the United States Department of Defense (DoD) Technology Readiness Levels (TRLs).

3.2.2 Analytical Hierarchy Process (AHP)

Having identified design criteria, the AHP was used to qualitatively compare the relative importance of each criteria to the specified mission. The AHP technique uses pair-wise comparisons between criteria and assigns relative weights to each criteria after comparisons are made. In the AHP matrix, a given criteria in the left-most column is independently compared against each criteria across the top row. A value greater than one (> 1.0) means the left-column criterion is more important than the corresponding top-row. Similarly, a value of less than one (< 1.0) denotes the left-column criterion is less important than the associated top row.

The AHP matrix in Table. 3.2 shows the normalized priority vector resulting from the comparisons made in the AHP matrix. Values within each column are normalized by the column sum, then averaged by row. The averaged result is a normalized priority value for each row, which can be ordered to provide a final ranking. Figure 3.3 ranks the criteria by descending importance. It should be noted that all the criteria listed are important for a successful final design, and that the AHP focuses the discussion on specific priorities for configuration selection.



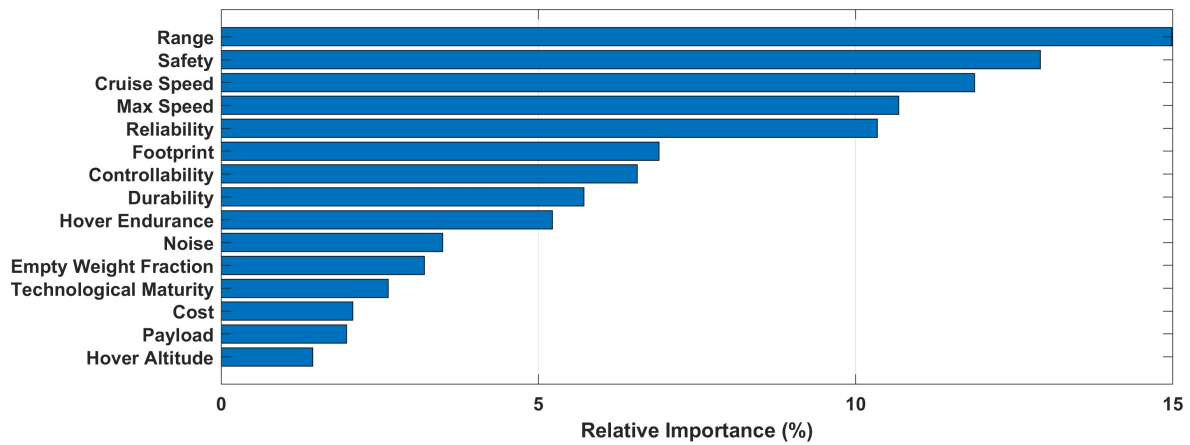


FIGURE 3.3: Relative ranking of key parameters through the Analytical Hierarchy Process (AHP).

TABLE 3.2: Parameter Weights from Analytical Hierarchy Process.

Prioritization Matrix	Cruise Speed	Max Speed	Range	Payload	Hover Endurance	Hover Altitude	Safety	Reliability	Empty Weight Fraction	Durability	Controllability	Noise	Footprint	Technological Maturity	Cost	Normalized Priority
Cruise Speed	1.00	2.00	1.00	5.00	4.00	5.00	2.00	1.00	3.00	1.00	2.00	4.00	4.00	3.00	4.00	0.119
Max Speed	0.50	1.00	2.00	5.00	5.00	6.00	3.00	2.00	3.00	2.00	2.00	4.00	5.00	5.00	4.00	0.107
Range	1.00	0.50	1.00	4.00	5.00	5.00	2.00	2.00	3.00	2.00	2.00	5.00	5.00	5.00	5.00	0.150
Payload	0.20	0.20	0.25	1.00	0.30	2.00	0.50	0.20	1.00	0.30	0.20	0.50	2.00	3.00	2.00	0.020
Hover Endurance	0.25	0.20	0.20	3.33	1.00	4.00	2.00	2.00	2.00	2.00	1.00	2.00	1.00	4.00	4.00	0.052
Hover Altitude	0.20	0.17	0.20	0.50	0.25	1.00	0.20	0.20	1.00	0.20	0.50	0.50	0.40	0.50	0.50	0.014
Safety	0.50	0.33	0.50	2.00	0.50	5.00	1.00	2.00	3.00	1.00	1.00	3.00	2.00	4.00	4.00	0.129
Reliability	1.00	0.50	0.50	5.00	0.50	5.00	0.50	1.00	2.00	2.00	1.00	3.00	3.00	4.00	4.00	0.103
Empty Weight Fraction	0.33	0.33	0.33	1.00	0.50	1.00	0.33	0.50	1.00	0.50	0.30	1.00	1.00	3.00	3.00	0.032
Durability	1.00	0.50	0.50	3.33	0.50	5.00	1.00	0.50	2.00	1.00	0.50	2.00	3.00	3.00	4.00	0.057
Controllability	0.50	0.50	0.50	5.00	1.00	2.00	1.00	1.00	3.33	2.00	1.00	3.00	4.00	4.00	4.00	0.066
Noise	0.25	0.25	0.20	2.00	0.50	2.00	0.33	0.33	1.00	0.50	0.33	1.00	3.00	1.00	1.00	0.035
Footprint	0.25	0.20	0.20	0.50	1.00	2.50	0.50	0.33	1.00	0.33	0.25	0.33	1.00	0.50	0.30	0.069
Technological Maturity	0.33	0.20	0.20	0.33	0.25	2.00	0.25	0.25	0.33	0.33	0.25	1.00	2.00	1.00	0.50	0.026
Cost	0.25	0.25	0.20	0.50	0.25	2.00	0.25	0.25	0.33	0.25	0.25	1.00	3.33	2.00	1.00	0.021

The ranking shows that range is the most important vehicle design criterion, followed by safety, cruise speed, max speed, reliability, footprint, controllability, durability, hover endurance, noise, empty weight fraction, technological maturity, cost, payload, and hover altitude. The insight provided is that range, safety, cruise speed, max speed, and reliability are the five criteria that account for over 60% of design considerations. Hence, before the configurations are pooled together, the design goals are focused on those that can provide speed, range, safety and reliability.

3.2.3 Configuration Selection: Pugh Matrix

Using the AHP results, Pugh decision matrices were made for both rotorcraft platform and fixed-wing platforms from Figure 3.2. With range being the most important criteria, each platform was evaluated relative to the tiltrotor with all its values set to zero. A positive number denotes relatively better performance compared to the baseline and a negative number denotes poorer performance. By doing so, each Pugh matrix isolates the best configuration for rotorcraft and



fixed-wing separately, leaving the reconfigurable mechanism bridging the two platforms together to be incorporated later on. Tables 3.3 and 3.4 show the results of these comparisons.

TABLE 3.3: Pugh decision matrix shows the various rotorcraft platforms ranked against the weighted AHP criteria and final scoring.

Rotorcraft	Weights	Tiltrotor	Single Rotor	Coaxial Rotor	Tandem Rotor	Multi-Rotor	Synchropter	Ducted Fan	Cyclocopter	Spinning Body
Range	0.150	0	-3	-2	-3	-4	-3	0	-2	-2
Safety	0.129	0	2	1	1	0	-1	1	-1	-2
Cruise Speed	0.119	0	-2	-1	-1	-2	-3	0	-1	-2
Max Speed	0.107	0	-2	-1	-2	-2	-3	0	-2	-3
Reliability	0.103	0	2	1	1	1	0	1	-1	-2
Footprint	0.069	0	1	2	0	-1	1	-1	0	-1
Controllability	0.066	0	1	1	0	2	1	-2	1	-3
Durability	0.057	0	1	0	0	3	-1	0	0	-2
Hover Endurance	0.052	0	3	2	2	2	1	1	0	-1
Noise	0.035	0	1	0	0	-1	-1	1	1	0
Empty Weight Fraction	0.032	0	1	0	1	-2	2	-2	-1	-1
Technological Maturity	0.026	0	2	0	1	1	0	-1	-2	-3
Cost	0.021	0	2	0	1	1	0	-1	-1	-2
Payload	0.020	0	-1	1	1	-2	1	-1	-3	-2
Hover Altitude	0.014	0	-1	0	0	1	1	0	-1	0
Score		0	0.040	0.035	-0.346	-0.686	-1.062	-0.011	-0.943	-1.947

Results	
Rotorcraft Platform	Score
Single Rotor	0.040
Coaxial Rotor	0.035
Tiltrotor	0.000
Ducted Fan	-0.011
Tandem Rotor	-0.346
Multi-Rotor	-0.686
Cyclocopter	-0.943
Synchropter	-1.062
Spinning Body	-1.947

TABLE 3.4: Pugh decision matrix shows the various fixed wing platforms ranked against the weighted AHP criteria and final scoring.

Fixed Wing	Weights	Tiltrotor	Monoplane	Biplane	Tandem Wing	Multi Wing	Flying Wing	Blended Wing	Delta Wing	Lifting Body	Box Wing
Range	0.150	0	2	1	2	-1	1	1	1	-1	1
Safety	0.129	0	2	1	1	0	-1	0	0	-2	0
Cruise Speed	0.119	0	2	-1	-1	-2	-1	0	3	3	0
Max Speed	0.107	0	3	-1	0	-2	-1	0	3	3	1
Reliability	0.103	0	2	1	1	-1	-1	0	1	-1	0
Footprint	0.069	0	1	2	2	-1	-1	-1	1	2	1
Controllability	0.066	0	1	0	1	0	-2	-1	0	-3	1
Durability	0.057	0	2	1	1	-1	0	0	1	0	0
Hover Endurance	0.052	0	-3	-3	-3	-3	-3	-3	-3	-3	-3
Noise	0.035	0	1	0	0	-1	1	1	0	-2	1
Empty Weight Fraction	0.032	0	2	0	0	-1	-1	0	0	0	0
Technological Maturity	0.026	0	2	2	1	-1	-1	-1	1	-1	0
Cost	0.021	0	3	2	2	1	-1	-1	2	-1	0
Payload	0.020	0	1	1	1	-1	-1	0	-1	-2	1
Hover Altitude	0.014	0	-3	-3	-3	-3	-3	-3	-3	-3	-3
Score		0	1.605	0.266	0.562	-1.123	-0.772	-0.197	0.904	-0.250	0.246

Results	
Fixed Wing Platform	Score
Monoplane	1.605
Delta Wing	0.904
Tandem Wing	0.562
Biplane	0.266
Box Wing	0.246
Tilt-rotor	0.000
Blended Wing	-0.197
Lifting Body	-0.250
Flying Wing	-0.772
Multi Wing	-1.123

From the rotorcraft group, the single rotor and coaxial lift–offset rotor scored nearly the same and both were scored higher than the baseline tiltrotor. From the fixed wing group, the monoplane, delta wing, tandem wing, biplane, and box wing platforms were improved designs over the tiltrotor, but the monoplane ranked far above the rest. Platforms that fell below the baseline were eliminated from consideration: ducted fans, tandem rotor, multi-rotor, cyclocopter, synchropter, spinning body, blended wing, lifting body, flying wing, and multi-wings. Therefore, two rotorcraft (single rotor/coaxial rotor) and five fixed-wing (monoplane, delta wing, tandem wing, biplane, and box wing) platforms advanced to the convergence step in Section 3.5.

3.3 Fuselage Orientation

The design space contains fuselage orientations: traditional and tailsitter. This is a separate category in the design space because any one of the platforms can be either of these orientations.



Decoupling the platforms from these orientations allow for focused analysis on the merits of the orientations alone:

- **Traditional:** A traditional vehicle fuselage is one where the body stays oriented relatively in the same place with respect to the earth from take-off to landing. Almost all manned aircraft are designed this way because human factors demand a fuselage that does not go through large changes in orientation to preserve comfort and pilot visibility. To combine VTOL with fixed wing forward flight for a traditionally oriented fuselage, either a compound configuration such as in Figure 3.4(a) or some reconfiguring mechanism such as the tiltwing in Figure 3.4(b) would have to be implemented. *Metaltail* does not use this type because of the geometric constraint stated in the requirements Section 3.1.



(a) Airbus Helicopters X3 compound helicopter



(b) NASA GL-10 Grease Lightning unmanned tiltwing

FIGURE 3.4: Traditional fuselage orientation for takeoff and landing.

- **Tailsitter:** *Metaltail* is a tailsitter configuration because of space-saving benefits and its autonomous feature. A tailsitter is a VTOL aircraft that takes off and lands on its tail section but transitions into a propeller configuration in forward flight. Tailsitters are mostly used by unmanned aircraft since the absence of a pilot eliminates the need to consider pilot attitude. For these vehicles, transitioning from vertical flight to forward flight does not necessarily require a compound configuration or a reconfigurable mechanism. These vehicles normally depend on tumbling maneuvers or large control surfaces to achieve forward flight. Examples of tailsitters are shown in Figures 3.5(a) and 3.5(b).

3.4 Reconfiguration Mechanisms

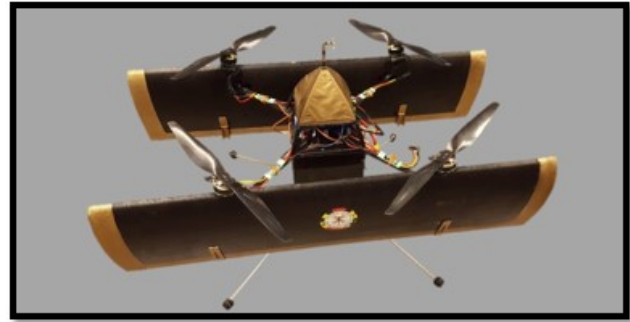
Metaltail uses a sweep mechanism on its wing, colloquially referred to as a swing wing, taking advantage of aerodynamic effects due to the shift in center of pressure. For more information on the physics and mechanism design, refer to Chapter 9. The enabling mechanism allows for reconfiguration of lifting and/or propulsive devices between operating states of the vehicle, namely hover mode to forward flight mode and vice versa. These mechanisms, described below, reconfigure the vehicle by a combination of changing orientation, location, and shape of a component or system of components.

- **Arresting Mechanisms:** Arresting mechanisms act on rotary components by changing orientation from rotating to non-rotating. By stopping a rotor's rotation, the rotor can be





(a) Convair XFY-1 "Pogo"



(b) University of Maryland Quad Biplane Tailsitter (QBiT)

FIGURE 3.5: Tailsitter configurations.

converted into a wing for forward flight. Examples include the Sikorsky X-Wing, which used a circulation control system, and X-50 Dragonfly as shown in Figure 3.6. By having a rotary wing become a fixed wing, multiple complexities can arise due to high structural loads and the requirement to invert one blade so that both blades are aligned in the same direction in wing-borne flight. These complexities lead to high weight penalties, and because of this arresting mechanisms were not selected for the final design.



(a) Sikorsky RSRA/X-Wing



(b) Boeing X-50 Dragonfly, concept

FIGURE 3.6: Stopped rotor using a) Circulation control and b) mechanically control.

- **Tilting Mechanisms:** Tilting mechanisms typically enable rotary systems to change their orientation and locations relative to a lateral body fixed axis. They are implemented as reconfiguration devices for tilt-rotors, tilt-wings, tilt-jets, tilt-ducts, and tilt-props, such as the V-22 Osprey and the Airbus A³ Vahana shown in Figure 3.7.
- **Sweeping Mechanisms:** Sweeping mechanisms are similar to tilt, however, they change the orientation and distribution of lift along the plane of the device. When implemented on wings, they are known as swing wings. Sweep-back benefits are more pronounced for transonic or supersonic aircraft because sweep delays the onset of shock waves and increases the critical Mach Number of the wing section. Swing wings are not typically used for subsonic aircraft since sweep can cause aerodynamic instabilities in level flight and the additional weight penalty of the mechanism is too large for a fixed cruise speed design: as sweep increases, the center of pressure moves farther aft of the center of gravity, producing a nose down pitching moment on the vehicle. However, *Metaltail* uses this





(a) V-22 Osprey

(b) Airbus A³ Vahana

FIGURE 3.7: Tilt mechanisms for a) tiltrotor and b) tiltwing vehicles.

aerodynamic effect as an advantage to enable transition. Swing wings are used on highly maneuverable aircraft, such as the F-14 Tomcat and the NASA AD-1, as seen in Figure 3.8.



(a) F-14 Tomcat



(b) NASA AD-1

FIGURE 3.8: Sweep mechanisms on a) supersonic fighter and b) low speed oblique wing aircraft.

- Folding Mechanisms:** Folding mechanisms change the orientation and location of components by folding the devices out-of-plane. This mechanism is typically used for stowing components of the vehicle during different operational modes or while on ground. Usually acceptable for short duration deployment, otherwise the weight penalty outweighs any potential benefits. NASA's Spanwise Adaptive Wing (SAW) project is experimenting with active wing folding for performance gains, and Joby S2 combines stopped rotors with folding blades as shown in Figure 3.9.



(a) NASA SAW



(b) Joby S2

FIGURE 3.9: Folding mechanisms for a) wing and b) proprotor blades.



- Extending Mechanisms:** Extending mechanisms have mostly been theoretical or wind-tunnel scale due to the difficulties in tailoring structural properties for components performing the extension. Projects like the Boeing DiscRotor, Figure 3.10(a), using telescoping rotor blades, have been attempted but ceased to advance beyond conceptual design. The Variable Diameter Tilt-Rotor (VDTR), from Sikorsky, advanced only up to the stage of wind tunnel testing. Small UAVs have been built with telescoping wings like the MIT Lincoln Lab UAV in Figure 3.10(b); however, the complexity of this mechanism results in low reliability, durability, and technological maturity.



FIGURE 3.10: Extending mechanisms on a) rotor blades and b) wings.

- Morphing Mechanisms:** Morphing mechanisms have been used since the days of the Wright brothers and their wing warping concept. A morphing system manipulates the shape of the lift device to gain improved performance in a given condition by using smart materials or structures. Changes to wing or blade camber, twist, or size are all possible with morphing technology; however, these mechanisms are typically used for enhancements rather than as a necessity for vehicle function. The Bell concept helicopter FCX-001 uses morphing blade geometries and NASA's Adaptive Compliant Trailing Edge (ACTE) project tests a morphing flap as a control surface, as shown in Figure 3.11.



FIGURE 3.11: Morphing mechanisms on a) rotor blades and b) wing flap.

- Disassembling Mechanisms:** Disassembling and assembling mechanisms are novel concepts that are just starting to attract attention, and can be quite versatile for aircraft by changing any combination of orientation, location, and shape of any system. The intention is for these mechanisms to be used with swarm technology, where multiple small



vehicles can combine to construct one large machine to perform a task that cannot be completed with smaller vehicles. These mechanisms depend on precise controls and reliable connecting structures. Considering this concept is still in its conceptual stage, its reliability, controllability and TRL can not be expected to be acceptable for this design. An example of this concept is shown in Figure 3.12, where two tailsitter-style propeller drones are first attached to the payload, then detached to initiate takeoff. After takeoff, the drones transition to level flight along a circular path to hover the payload. For forward flight, the drones maneuver to face the same direction.

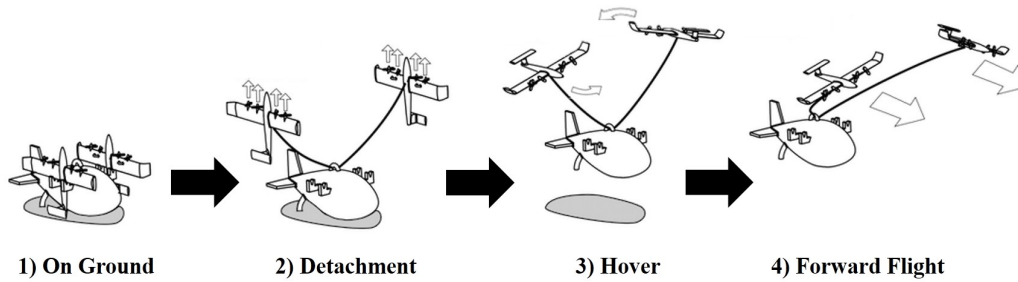


FIGURE 3.12: Conceptual disassembling aircraft in Create The Future 2015 design contest.

3.5 Configuration Convergence

From Pugh decision matrix results, the pool was reduced to twenty configurations shown in Figure 3.13. Further reduction required incorporating mission requirements, body orientation and reconfiguration mechanism.

		Fuselage Orientation	
		Traditional	Tailsitter
Platform	Single Rotor	Monoplane	Monoplane
		Delta Wing	Delta Wing
		Tandem Wing	Tandem Wing
		Biplane	Biplane
		Box Wing	Box Wing
	Coaxial Rotor	Monoplane	Monoplane
		Delta Wing	Delta Wing
		Tandem Wing	Tandem Wing
		Biplane	Biplane
		Box Wing	Box Wing

FIGURE 3.13: Twenty potential configurations.

3.5.1 Downwash Velocity

Downwash velocity is an important factor that directly affects any people or objects in the vehicles flight path. High downwash introduces both noise and safety concerns. These concerns are of great importance because of the requirement to operate inside megacities with dense populations, where any impact on the ground below the vehicle needs special consideration. Disk loading versus downwash velocities for various VTOL aircraft was evaluated based on



momentum theory considerations and then compared with potential vehicles designed for the RFP, as shown in Figure 3.14.

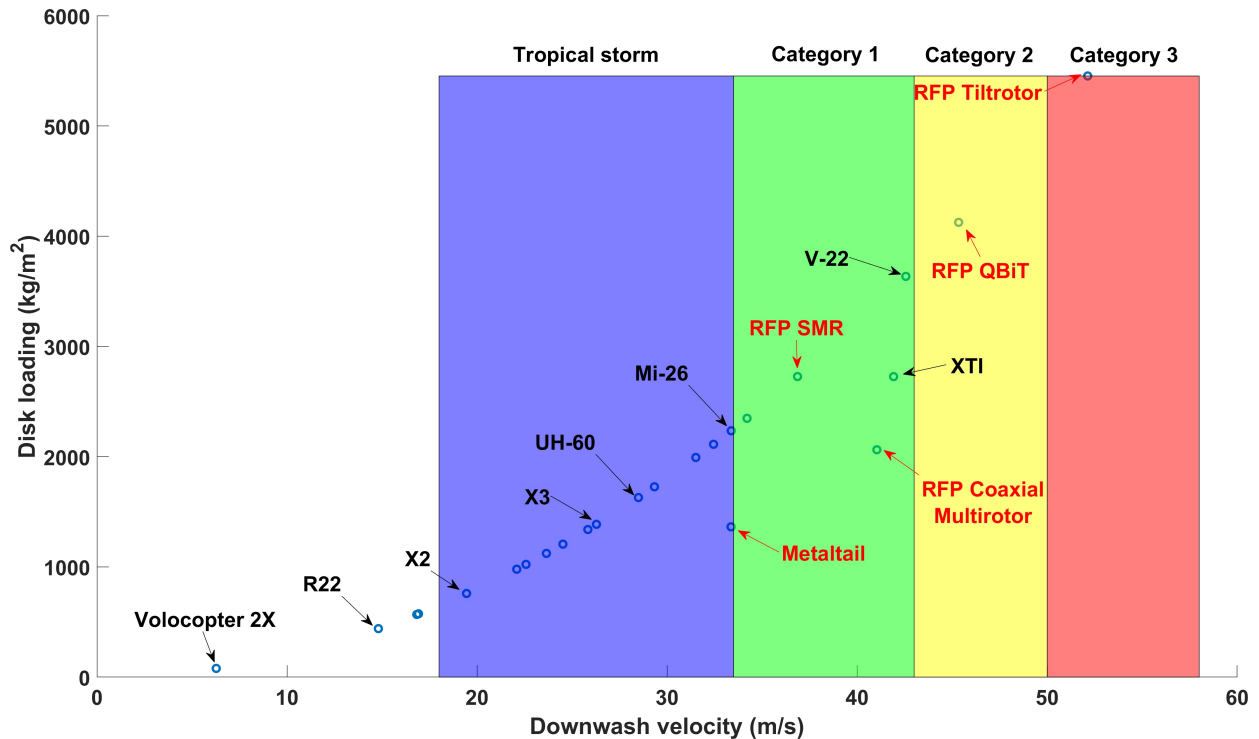


FIGURE 3.14: Disk loading vs. downwash velocities for existing VTOL denoted in black, VTOL designs for the RFP denoted in red.

All the vehicles labeled in red were analyzed with the 3×3 meter geometric constraint which increased the disk loading and downwash velocities significantly for a 600 kg vehicle. The shaded regions denote wind speeds of storm systems on the Saffir–Simpson hurricane wind scale (SSHWS). A tropical storm is classified as winds from 18 m/s to 32 m/s, a category one hurricane from 33 m/s to 42 m/s, a category two hurricane from 43 m/s to 49 m/s, and above 50 m/s is a category three hurricane, which is an acceptable cutoff to limit the study. These results show that *Metaltail*, with a coaxial rotor, has the lowest downwash velocity when compared to an SMR, a coaxial multirotor, a quad multirotor, and a tiltrotor, because it is able to minimize the disk loading, and therefore downwash, for a given geometric constraint, i.e. maximum rotor dimension. Additionally, an added benefit of the coaxial rotor having the lowest disk loading of the RFP vehicles is higher hover efficiency. This meant that any single rotor platform in the upper half of Figure 3.13 was dismissed, eliminating ten potential configurations and leaving only coaxial configurations as shown in Figure 3.15.



		Fuselage Orientation	
		Traditional	Tailsitter
Platform	Coaxial Rotor	Monoplane	Monoplane
		Delta Wing	Delta Wing
		Tandem Wing	Tandem Wing
		Biplane	Biplane
		Box Wing	Box Wing

FIGURE 3.15: Potential configurations reduced to ten.

3.5.2 Geometric Constraint in Hover Configuration

By virtue of having a horizontal dimension limitation in hover, the traditional fuselage orientation was eliminated. Capitalizing on the unhindered space in the vertical dimension, a tailsitter's fuselage can be extended beyond three meters, facilitating a slender fuselage design. This requirement and subsequent decision caused the selection space to converge to five candidates shown in Figure 3.16.

		Fuselage Orientation
		Tailsitter
Platform	Coaxial Rotor	Monoplane
		Delta Wing
		Tandem Wing
		Biplane
		Box Wing

FIGURE 3.16: Potential configurations reduced to five.

3.5.3 Top Configuration Candidates

The remaining configurations were:

- **Coaxial Monoplane Tailsitter:** A coaxial monoplane tailsitter combines the best platforms from the Pugh matrices. A single wing has the least amount of aerodynamic drag penalties and provides a reliable design for reconfigurable systems; therefore, this configuration was selected to be *Metaltail*.
- **Coaxial Delta Wing Tailsitter:** Essentially the Convair XFY-1 “Pogo” vehicle, this configuration has been tested and proven to be flight worthy through many tests in the 1950s. However, issues arose with this configuration for low-speed forward flight velocities. Delta wings are exploited for transonic and supersonic flight, which was not an operating condition required by the RFP, which was why this configuration was not selected.
- **Coaxial Tandem Wing Tailsitter:** Much like the biplane, a tandem wing possesses two wings that contribute to lift, however, they are spread longitudinally along the fuselage. These wings can be in the same plane or staggered with one wing higher or lower than the



other. This configuration eliminates the need for a horizontal stabilizer as the wings can act together to achieve stability and control. However, tandem wings' small aspect ratio wings are more influenced by three-dimensional aerodynamic effects as well as have higher induced drag compared to a larger aspect ratio wing at the same coefficient of lift.

- **Coaxial Biplane Tailsitter:** A biplane uses two wings stacked on top of each other such that their lift vectors are close together, and in addition, a horizontal stabilizer is still required. This configuration reduces footprint by decreasing the wing span and increases maneuverability at the cost of increased drag from support frames and struts between the wings. These components produce interference drag that significantly decreases the maximum speed.
- **Coaxial Box Wing Tailsitter:** A box wing or closed wing design reduces the effects of wingtip vortices and increases structural stiffness as compared to cantilever wings. At the small scale the benefits of a box wing are easily identifiable but at this scale the structural negatives begin to limit any potential gains. Additionally, incorporating a fundamental reconfigurable aspect for a box wing greatly increases the complexity and discouraged the pursuit of this configuration.

3.6 Final Configuration

Metaltail's final configuration is a coaxial, single swing wing, tailsitter aircraft. The coaxial rotor provides a lower disk loading as well as reduces downwash velocity, while the tailsitter orientation exploits the unbounded vertical dimension in hover configuration. The reconfigurable swing wing acts as the main lift device in forward flight, enabling agile yet controllable transition maneuvers, and maintains the horizontal dimension of the vehicle in hover to fit within a 3×3 meter square. By employing a top-down approach with well-defined requirements and a large design space, a simple yet elegant solution to the RFP was achieved.

4 Preliminary Vehicle Sizing

A sizing code was developed in-house using the methodology of Tischenko [2]. The AFDD model was used to calculate the component weights, and modified momentum theory (including induced and profile losses) was used to calculate the required power [3]. The basic AFDD model was found to be sufficient for a first-order estimate of component weights, with exact weights being determined during detailed design.

4.1 Sizing Mission

The mission chosen to size the vehicle, given in detail in Sec. 2.2, was based on a round-trip between two large urban hospitals. NYU Medical Center in New York City and Children's National Medical Center in Washington, DC were chosen as representative examples. These two hospitals are approximately 200 nmi (370 km) apart. A target cruise speed for best range of 180 kts was chosen based on L/D calculations, yielding a travel time of slightly over an hour in one direction. This travel time is considerably less than land-based transport over the same distance. Higher speeds, led to larger and heavier aircraft. *Metaltail's* small size allows it to operate with just the right amount of urban footprint to be useful and avoid the complex logistics of transport to and from airports.



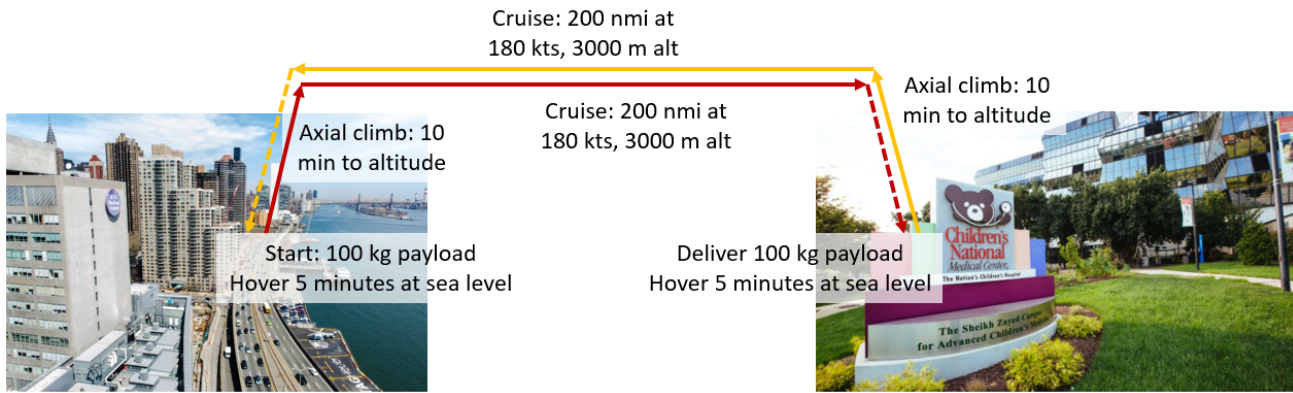


FIGURE 4.1: Sizing mission profile for medical transport.

The sizing mission stipulates that *Metaltail* transports 100 kg of high-priority cargo (e.g. organs) from NYU Medical Center, unload its entire payload at Children’s National, then return empty to NYU without refueling. The sizing mission assumes that the vehicle performs an axial climb up to its cruising altitude before transitioning to horizontal wing-borne flight. However in practice, *Metaltail* would only perform an axial climb up to the altitude necessary to avoid buildings or other obstacles, then transition to horizontal flight to complete its climb to cruise altitude. Hover segments were included to simulate taxi and ground operations. An overview of the complete flight mission profile is shown in Figure 4.1. Note that additional fuel to ensure a 20% margin for the mission was calculated within the weight module, so is not included in the mission itself.

4.2 Design Drivers

1. **Rotor diameter:** The requirement to operate within a 3 meter span in hover places the principle constraint on the size of the vehicle. As noted in Section 3.6, a single coaxial main rotor was chosen to use the available area in the most efficient manner. The effect of using a smaller single rotor is examined in Section 3.5. However, to reduce the downwash from the rotor, it was desired to incorporate as large a rotor as possible to reduce the disk loading. High downwash is a concern particularly for operating in a megacity environment and from imperfect landing zones, where loose objects may be present which could cause damage to people, buildings, or the vehicle if caught in the rotor wake and thrown at high speed.
2. **Wing span:** While there is a requirement on the maximum span of the vehicle in hover, there are no requirements on the height of the vehicle, or the span of the vehicle in cruise. A higher aspect ratio wing is always more efficient but requires a relatively larger span. To allow an efficient wing planform, while remaining within the hover span limit, the wing of *Metaltail* folds back in hover and extends in cruise. With this folding mechanism, the span of the wing is no longer a major constraint.
3. **Blade loading:** An additional concern was ensuring that any vehicles predicted by the sizing code would be physically plausible. To that end, it was assumed that the blades would stall at $C_T/\sigma \approx 0.16$, so any vehicles with higher blade loading were removed from consideration. Because the blade loading was calculated in hover, a more conservative target of $C_T/\sigma \approx 0.1$ was chosen to ensure that there would be sufficient blade loading margin during the transition to wing-borne flight, and to provide sufficient control authority during gusts.



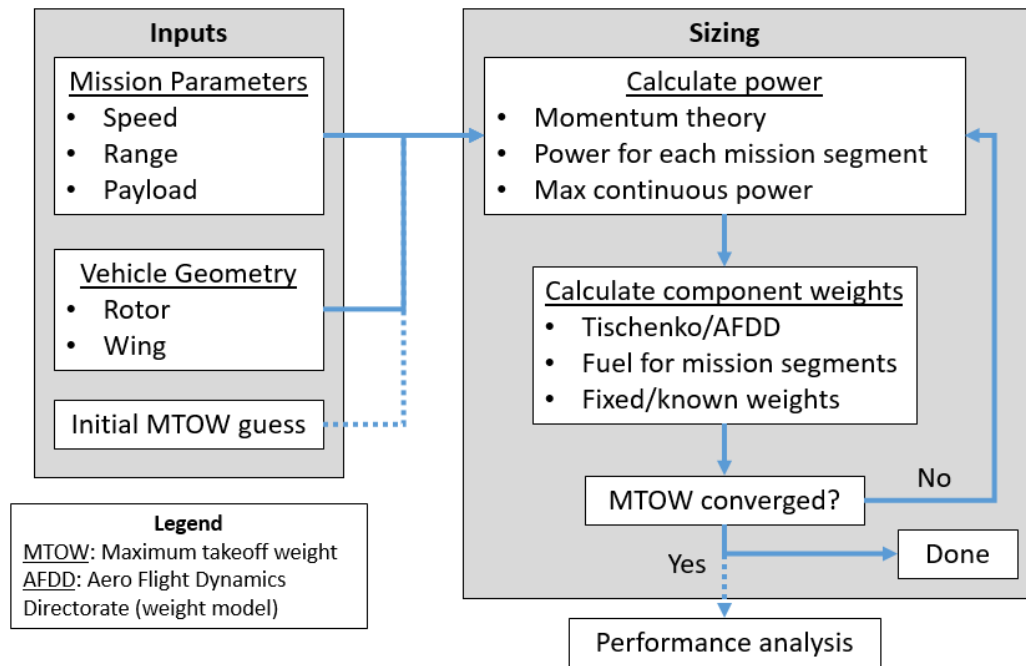


FIGURE 4.2: Flowchart of the iterative sizing procedure.

4.3 Sizing Methodology

An in-house methodology was developed to size the vehicle is based on Tischenko’s method [2], as shown in Figure 4.2. Most of the component weights were determined using the US Army’s AFDD empty weight model. Once an engine had been selected (see Section 8.1.1), the engine weight was fixed, as the chosen engine has a significantly higher specific power than the historical trend. Within the sizing loops, the vehicle configuration defined which components were necessary and which were not. An overview of the iterative methodology is shown in Figure 4.2.

The methodology requires a set of inputs which describe the vehicle geometry, and the mission which the vehicle is expected to perform. Because the rotor is size-limited, the rotor radius is taken as one input. To complete the rotor geometry, the aspect ratio and number of blades (per each of the two disks of the coaxial rotor) was specified. All other rotor parameters (e.g. disk loading, solidity) are then calculated within the code. Since the wing is not as strongly constrained as the rotor, its inputs are wing loading and aspect ratio. The dimensions of the wing are then calculated within the code. The sizing mission (Sec. 4.1) is specified in terms of its segments (e.g. hover, climb, cruise).

Within the sizing loop, the first step is to calculate the power and fuel required to complete the sizing mission. The power is calculated based on a modified momentum theory method, taking into account inefficiencies due to profile and induced losses. The coaxial rotors are considered thrust-balanced, and an empirical correction factor $\kappa_{int} = 1.14$ is included in the induced power to account for interference between the rotors. In airplane-mode forward flight, two different power calculations may be used: (1) Momentum theory “axial climb” calculations, with thrust being equivalent to drag instead of weight, and (2) Fixing efficiency based on the known or target propeller efficiency, then $P = Tv/\eta_{prop}$.

The first method is more mathematically rigorous as the configuration is iterated, but perhaps



somewhat conservative (over-predicts the required power). The latter method relies on having a reasonable estimate of propeller efficiency. The drag area for the fuselage was estimated as a function of the takeoff weight[4]. The wing drag is also calculated, including a correction for the wing aspect ratio, and the total drag is taken as the sum of the wing and fuselage drag.

Using the discretized sizing mission, two values of power are calculated for each mission segment; the maximum power, calculated with the full fuel load at the beginning of the segment, and the mid-weight power, calculated with half the fuel required for the particular segment consumed. The maximum power is used to size the installed power for the vehicle, with the requirement that the maximum (continuous) power never exceed 80% of the installed power, and that relative to sea level (SL), the power available at altitude is $P_{alt}/P_{SL} = (\rho_{alt}/\rho_{SL})^{0.7}$. It was assumed that the average power for the mission segment is equal to the mid-weight power, which is a reasonable assumption. Then the fuel for the segment is calculated for the engine running at the mid-weight power constantly for the time taken to complete the mission segment.

Once the power required and fuel weights are calculated, the individual component masses are calculated using the AFDD method. It should be noted that all technology factors were set to be $\chi = 1.0$. The takeoff weight is calculated as the sum of the component weights, fuel weight, and initial payload weight. Finally, the takeoff weight at the end of the iteration is compared to the weight at the start of the iteration. If the difference between the two values is below the specified tolerance, then the sizing is considered converged. If not, the process repeats, replacing the previous initial takeoff weight with the value computed by the previous iteration.

4.4 Parametric Study

A summary of the parameters studied and their ranges are shown in Table 4.1. These input parameters define the design of the rotor, affecting the required power and thus the overall size of the vehicle.

A sample of the design points examined is shown in Fig. 4.3 in terms of maximum take off weight (MTOW) versus blade loading (C_T/σ).

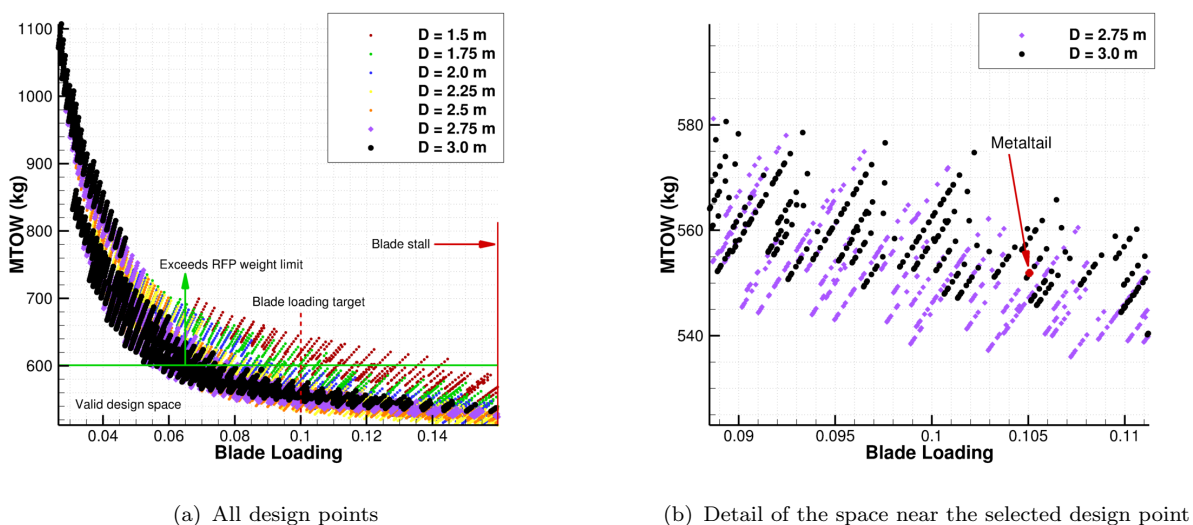


FIGURE 4.3: Range of design points for the vehicle



TABLE 4.1: Definition of the parameter space

Parameter	Minimum		Maximum	
	Value	Limit	Value	Limit
Main rotor diameter	1.5 m	Hover power	3.0 m	RFP limit
Blade aspect ratio	4.0	Low aero efficiency	20.0	Structural
Number of blades	3	Blade loading	5	Tracking & balancing
Rotor tip speed	200 m/s	Blade loading	240 m/s	Acoustics, tip Mach

The final parameters are shown at the end of this chapter, in Table 4.2. All parameter variation presented in this section is performed about the final design point.

4.4.1 Rotor Diameter

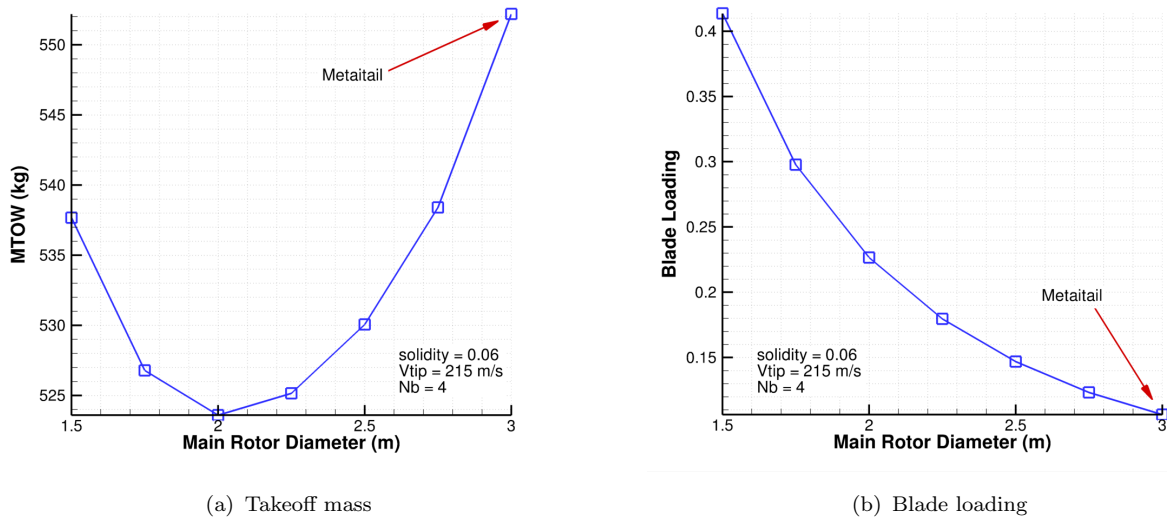


FIGURE 4.4: Effect of varying rotor radius on vehicle properties

The rotor diameter was varied between a minimum of 1.5 m and a maximum of 3.0 m. The maximum value is clearly defined by the constraints placed on the vehicle, while the minimum value was chosen which allowed the observation of MTOW with diameter. A smaller rotor would theoretically allow the vehicle to operate from more confined spaces, so the largest value could not necessarily be assumed to be optimal without analysis.

Plots of takeoff weight (MTOW) and blade loading (C_T/σ) versus rotor diameter are presented in Figures 4.4(a) and 4.4(b), respectively. To generate these plots, the rotor solidity, σ , (i.e. number of blades and aspect ratio) was held constant, and a fixed propeller efficiency, η_p , was specified.

As shown in Figure 4.4(a), it is possible to arrive at a lighter vehicle by specifying a lower rotor diameter, with the minimum takeoff mass predicted to occur for a vehicle with a diameter slightly larger than 2 meters, although the maximum weight savings is limited to approximately 5%. This decrease in weight is driven primarily by the smaller (thus lighter) blades and hub. However, decreasing the size of the rotor correspondingly increases C_T , so many of these solutions are not physical (Fig. 4.4(b)).



While it would be possible to find a physical solution with a lighter weight than the 3 m diameter design, this is not necessarily desirable for ground operations. A minimum disk loading is preferred to reduce the downwash from the rotor to the degree possible, which is important for operating from environments that may have loose objects, or operating in the vicinity of people on the ground. The disk loading was decided to be of greater concern to the chosen missions (see Ch. 3) than achieving a minimum weight, as long as the weight was no greater than the maximum allowed. Thus, it was decided to use a rotor with the 3.0 m diameter.

4.4.2 Rotor Aspect Ratio and Number of Blades

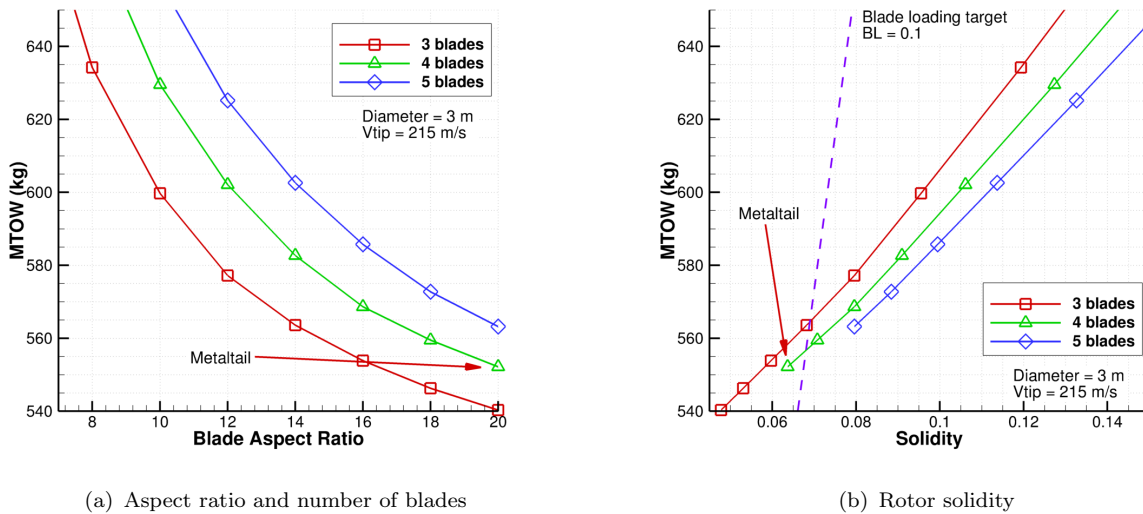


FIGURE 4.5: Effect of varying rotor properties on the takeoff mass

The rotor aspect ratio and number of blades are related through solidity, $\sigma = N_b/\pi AR$, and it is the solidity which most strongly affects the performance of the vehicle. The blade aspect ratio was varied from a minimum of 4.0 to a maximum of 20.0, and designs with 3, 4, and 5 blades were considered. It was estimated that a blade with an aspect ratio greater than 20 would not be structurally sound, and the minimum value of 4.0 was chosen to capture a wide parameter space. A 2-bladed rotor was not considered because it would require a large chord (low aspect ratio) to achieve reasonable blade loading. A 5-bladed rotor provided sufficient solidity even with the highest possible aspect ratio, so it was deemed unnecessary to examine rotors with a greater number of blades than 5.

The effect of varying these parameters on the takeoff mass is shown in Figure 4.5. (*Note:* Installed power varies directly with takeoff mass, so is not shown for brevity.) Observe that the association of takeoff mass is stronger with solidity (Fig. 4.5(b)) than with aspect ratio and the number of blades independently (Fig. 4.5(a)). Note that solidity is defined as the solidity of a single rotor, so the total solidity of the coaxial system is 2σ .

In general, lowering the solidity (higher aspect ratio, fewer blades) lowers the takeoff mass. This is because: (1) a lower solidity rotor has fewer, thinner blades, thus decreasing the weight of the rotor and the hub, and (2) a lower solidity rotor results in less profile drag, decreasing the power required, which decreases fuel and propulsion system masses. However, as the solidity



decreases, the blade loading increases (Fig. 4.5(b)) for the same vehicle weight. The final design parameters were selected by the following process:

1. The largest possible aspect ratio was chosen to minimize the takeoff weight (Fig. 4.5(a)) while remaining structurally sound.
2. The number of blades was selected such that $C_T/\sigma \approx 0.1$ at the chosen aspect ratio.

The aspect ratio was selected to be 20.0—the maximum considered strong enough for the initial design. Based on an aspect ratio of 20.0, a 4-bladed rotor resulted in a blade loading of $C_T/\sigma = 0.105$, which provides sufficient stall margin for maneuverability and gusts.

4.4.3 Tip Speed

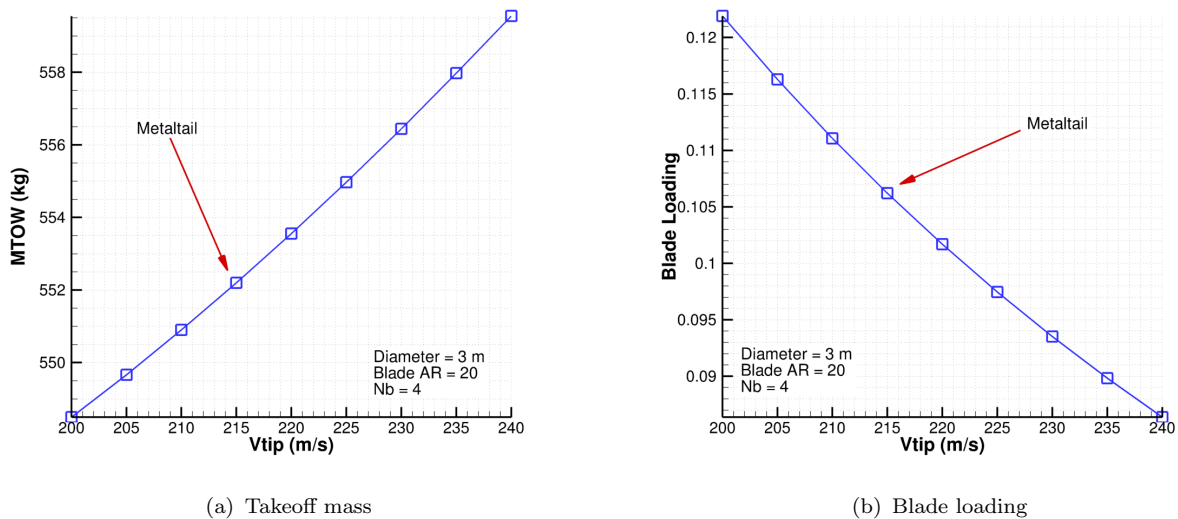


FIGURE 4.6: Effect of varying rotor tip speed on vehicle properties

The tip speed of the main rotor was varied from 200 m/s to 240 m/s. This range was chosen to reflect typical values for a helicopter of comparable size to *Metaltail*. The effect of varying the tip speed on the takeoff mass and blade loading is shown in Figure 4.6.

As the tip speed is decreased, the blade profile drag, and thus the power required, also decreases. The decrease in required power decreases both the powertrain and fuel weights. However, recall that $C_T/\sigma \propto 1/V_{tip}^2$, thus decreasing the tip speed increases the blade loading. A compromise design was chosen with a 215 m/s tip speed, relaxing the target blade loading slightly, such that the final $C_T/\sigma = 0.105$, only slightly larger than the target value, but still well within the safe margin for maneuvers.

4.4.4 Wing Sizing

The AFDD model was used for an initial estimate of the wing weight. While the AFDD model accurately represents traditional aircraft wings with metal construction, the wing of *Metaltail* is constructed of composite materials, and has a unique structure due to the requirement for variable sweep. Since the AFDD model does not apply to this type of wing, a detailed



TABLE 4.2: Results of the sizing procedure

Design Parameters	
Parameter	Value
Rotor diameter	3.0 m
Blade aspect ratio	20.0
Number of blades	4
Rotor tip speed	215 m/s
Wing aspect ratio	12.0
Wing loading	2873 N/m ²
Vehicle sizes and weights	
Parameter	Value
MTOW	552 kg
Empty mass	319 kg
Fixed equipment	29 kg
Fuel mass	104 kg
Wing span	4.76 m

analysis was performed (see Chapter 9), taking into account aerodynamics, structural weight, and material stresses[4]. From this analysis, a wing loading of 2873 N/m² and aspect ratio of 12 were determined, which corresponds to a wing with 4.76 m span.

4.5 Preliminary Sizing Results

The results of the sizing procedure are summarized in Table 4.2 for the vehicle with the sizing mission shown previously. Overall, the design of *Metaltail* is a lighter vehicle than the maximum allowable weight, while still completing the stringent sizing mission, with sufficient margins to ensure a safe design.

5 Blade Aerodynamic Design

5.1 Design Goals

The *Metaltail* coaxial prop-rotor design enables efficient hover and high-speed flight, providing exceptional performance in both flight regimes. The design was driven by the critical importance of high-speed capability for the design mission and the prolonged duration of the cruise segment. Therefore, a priority was given to designing a prop-rotor with higher cruise efficiency, rather than hovering efficiency.

The design of a prop-rotor, that achieves efficient high-speed cruise while maintaining efficient hover, is challenging due to the difference in the flow environment at the rotor. A significant difference exists between, high-speed cruise and hover, inflow angles along the blade of a prop-rotor. Compared to high-speed cruise, the prop-rotor in hover experiences relatively low inflow angles near the blade root. The local Mach number at the two flight regimes may differ significantly, depending on the cruise speed. Because of the significant differences between operating conditions in hover and cruise, the optimal blade geometry also differs for each regime.

Metaltail is a coaxial prop-rotor with bi-linear twist, 2:1 (ratio of chord, root to tip) linear taper,



variable RPM and three airfoils along the blade, shown in Fig. 5.1. The detailed design of prop-rotor blades will be discussed in the following sections. The baseline blade characteristics, shown in Fig. 5.2, were modified to examine the key trends and the effects of various geometric blade parameters on the figure of merit and the propulsive efficiency. The summary of the design conditions are shown in Table 5.1.

5.1.1 Blade Airfoil Requirements

Several features are important for the airfoil used on the rotor blade: It should have a high lift-to-drag for efficiency, and a wide drag bucket and gentle stall characteristics for situations where the airfoil must operate away from its design point. Several airfoils which met these requirements were considered, all of which had a thickness to chord ratio of approximately 12%: the SC1095, VR7 and VR12, canonical rotor airfoils; the NACA 2412, which is simple to model; the Clark Y, a canonical propeller airfoil; and the SD7062, a fixed-wing airfoil with a design point close to the operating condition of *Metaltail's* rotor.

At the root of the blade, it is necessary to thicken the blade to ensure that the blade has the required structural properties. Additionally, a thicker cambered airfoil may actually have more gentle stall characteristics than a thinner cambered airfoil, particularly at large negative angles of attack. For these reasons, the airfoils considered for the root are all 20% thick versions of the airfoils tested for the main section. To obtain these airfoils from the base airfoil, the coordinates of the airfoil were stretched about the chord line.

The tip of the rotor blade moves considerably faster than the inboard blade sections, and so Mach effects must be considered when selecting an airfoil for the tip. For this reason, thinner 8% airfoils were considered: the VR8 and VR15, NACA 2408, SD7032, and a thinned version of the Clark Y.

Through proper selection of the root, main section, and tip airfoil sections, it is possible to design a blade which operates in an efficient condition over a greater portion of its span, thus increasing the overall efficiency of the rotor.

TABLE 5.1: Rotor design specifications and flight conditions

	Hover	Cruise
Tip Speed	215 <i>m/s</i>	183 <i>m/s</i>
C_T	0.0068	0.0016
C_T/σ	0.1061	0.0247
Altitude	Sea-level (ISA)	3000 <i>m</i> (ISA)
Cruise speed	-	333 <i>km/h</i>

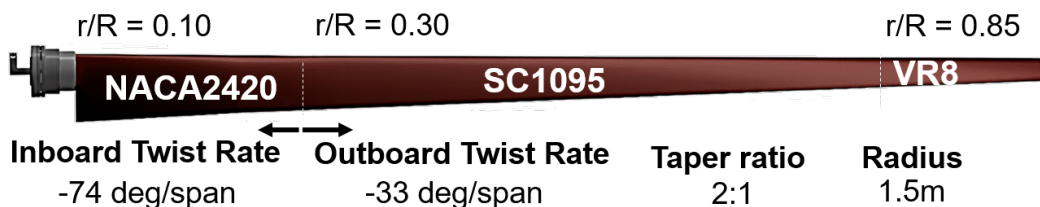


FIGURE 5.1: *Metaltail* blade for both, the upper and lower rotor



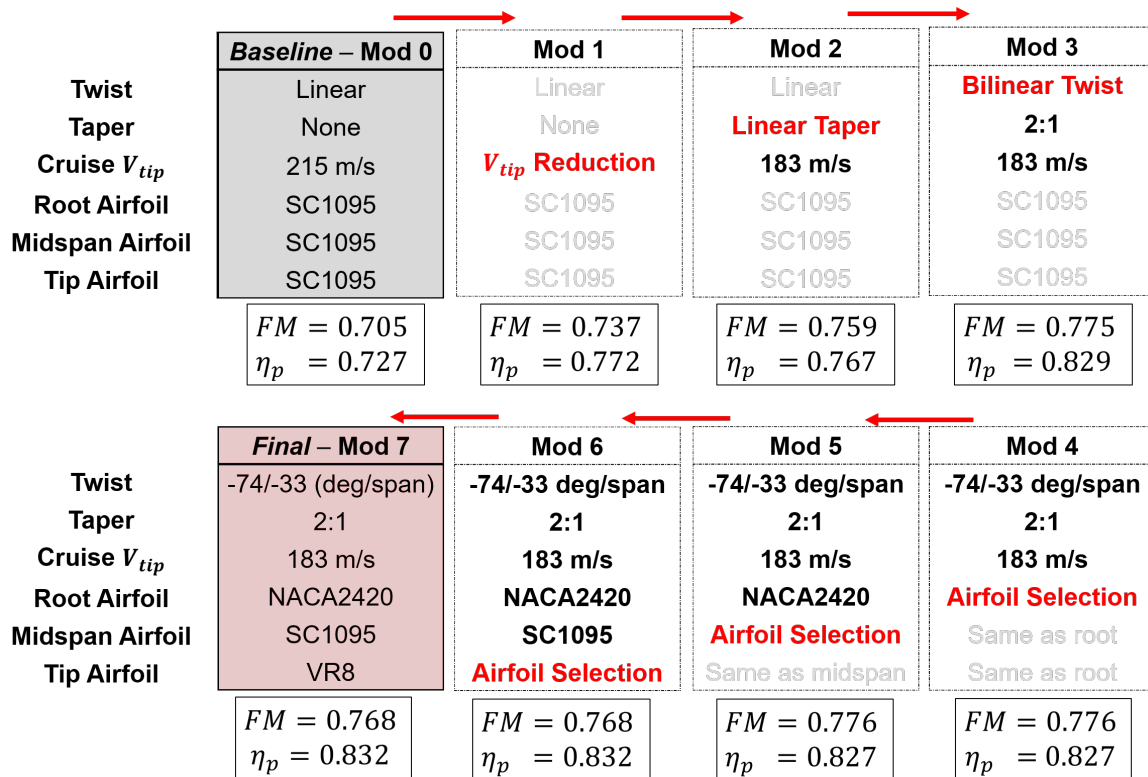


FIGURE 5.2: Blade design process

5.2 Design Methodology

An in-house blade element momentum theory (BEMT) analysis was used to conduct parametric blade studies and to evaluate the performance of an isolated rotor in hover and axial flight. An in-house, Free-Vortex Method (FVM) analysis was used to quantify the effects of interference for the coaxial rotor configuration. Unlike in a typical BEMT analysis, no small angle assumptions were made due to the large inflow angles experienced during axial regime near the blade root. The current analysis included Prandtl's tip-loss factors and airfoil tables containing variation in C_l and C_d with Mach number, for 15 airfoils. The blade design process, performed for an isolated rotor, consists of seven steps, shown in Fig. 5.2 and described as following:

1. A rectangular blade with linear twist and a constant airfoil along the blade was used as preliminary design (Mod 0).
2. Reduction in cruise tip speed, by fifteen and twenty percent of the hover tip speed, was investigated (Mod 1).
3. Taper of the blade was varied at a equivalent thrust-weighted solidity (Mod 2).
4. Bi-linear twist was implemented (Mod 3).
5. Variable airfoil sections were tested along the blade (Mod 4, 5 and 6).
6. Final blade selection (Mod 7).



At the end of each design step, Figure of Merit (FM), Eq. 5.1, and propulsive efficiency (η_p), Eq. 5.2, were used as metrics to quantify the efficiency of the design in hover and cruise, respectively.

$$FM = \frac{C_T^{3/2}/\sqrt{2}}{C_p} \quad (5.1)$$

$$\eta_p = \frac{\lambda_c C_T}{C_p} \quad (5.2)$$

After the selection of the final blade design, the performance of the final rotor was analyzed at a range of cruise speeds and blade loadings. The FVM analysis was used to model the coaxial configuration and explore the effect of interference on performance.

5.3 Blade Aerodynamic Design

Trade studies were conducted to determine the linear twist slope, cruise tip speed and taper for a baseline blade before proceeding to a design of a blade with bi-linear twist. These trade studies were performed with one airfoil, SC1095, along the span of the blade. Once bi-linear twist was implemented, and the updated baseline blade was determined, airfoil trades studies were conducted to determine the best combinations of airfoils along the blade.

5.3.1 Step 1: Baseline Blade

A rectangular blade with linear twist and a constant airfoil along the span was considered for preliminary blade design, represented as Mod0 in Fig. 5.2. Blades with the same twist rates were analyzed at both hover and cruise (at 100 percent of the hover tip speed), at their respective design thrust coefficients. The thrust coefficient for hover and cruise are defined in Eq. 5.3 and Eq. 5.4, respectively. The operating conditions for the baseline blade are shown in Table 5.1. A parametric study was conducted to quantify the effects of twist rate on the efficiencies in both cruise and hover. The twist rates ranged from -20 degrees/span to -45 degrees/span, as shown in Fig. 5.3. The preliminary study showed that the efficiencies at hover and cruise can be relatively high (FM and η_p greater than 0.75) at their respective optimum twist rates. For hover, the highest figure of merit of 0.810 occurred at -22 degrees/span, whereas highest cruise efficiency of 0.7864 occurred at -45 degrees/span. As the twist rate increased past -25 degrees/span, the figure of merit dropped significantly due to an increase of angles of attack at the blade root. Similar behavior was observed for cruise, the efficiencies dropped significantly beyond the optimal twist rate, due to the increase of the blade root angle of attack. One way that the blade can operate at the optimum twist rate in both flight conditions, is by morphing to blade to employ variable twist. However, to morph the blade to accommodate the large variation in the required twist between the two operational states would require a very complex mechanism and is beyond any practical means. The baseline design was chosen to compromise between the hover and cruise efficiency, FM of 0.705 and η_p of 0.727, with -34 degrees/span twist rate varying linearly along the rectangular blade. Further modifications are needed to significantly increase the efficiency of the rotor to the design metrics.

$$C_{Thover} = \frac{MTOW}{\rho A (V_{tip})^2} \quad (5.3)$$



$$C_{T\text{cruise}} = \frac{L/D}{\rho A (V_{tip})^2} \quad (5.4)$$

TABLE 5.2: Rotor design specifications and flight conditions

	Hover	Cruise
Tip Speed	215 m/s	215 m/s
C_T	0.0068	0.0016
C_T/σ	0.1061	0.0247
Altitude	Sea-level (ISA)	3000 m (ISA)
Cruise speed	-	333 km/h

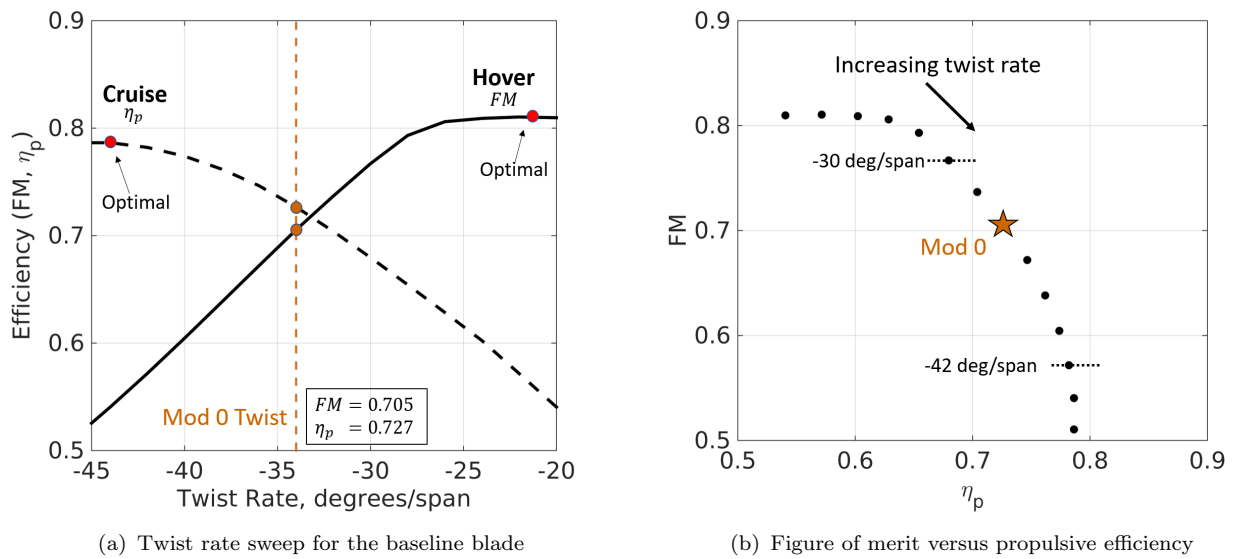


FIGURE 5.3: Baseline blade efficiency comparison for cruise and hover

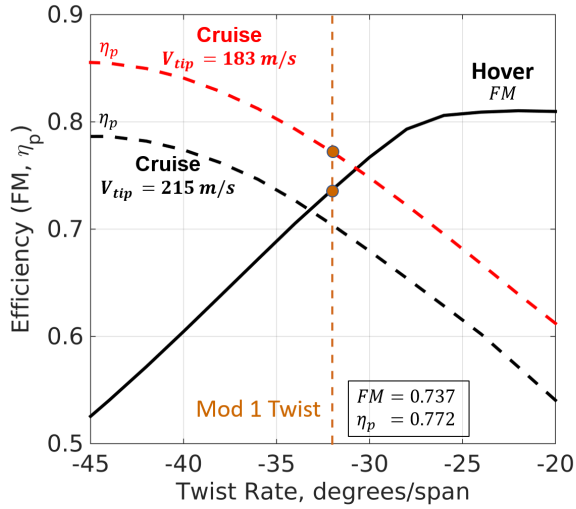
5.3.2 Step 2: Rotor RPM Variation

A study was conducted to investigate the effect of tip speed reduction on the cruise efficiency, at cruise thrust. Figure 5.4 shows the effects of reducing cruise tip speed by 15%, while keeping the hover tip speed at the design tip speed. The maximum tip speed reduction was constrained to 15% of hover tip speed, to limit the engine off-design penalties. Reducing the tip speed during cruise, significantly increased the propeller efficiency, shown in Fig. 5.4. Improvement in efficiency stemmed from improvement in the sectional thrust loading and reduction of the tip Mach number. All following studies were conducted with cruise tip speed at 85 percent of hover tip speed.

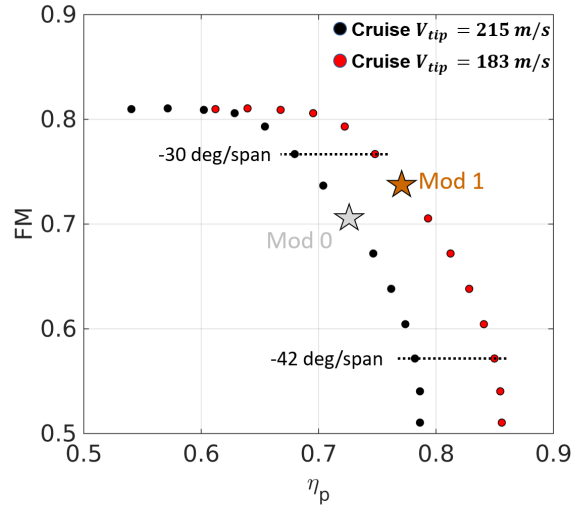
5.3.3 Step 3: Blade Taper Selection

A trade study was conducted to explore the effect of taper ratio on the hover and cruise efficiencies. Taper ratio is defined as the ratio of root to tip chord length. Taper ratio was varied between 1:1 (baseline) and 2:1, keeping equivalent thrust weighted solidity constant. The





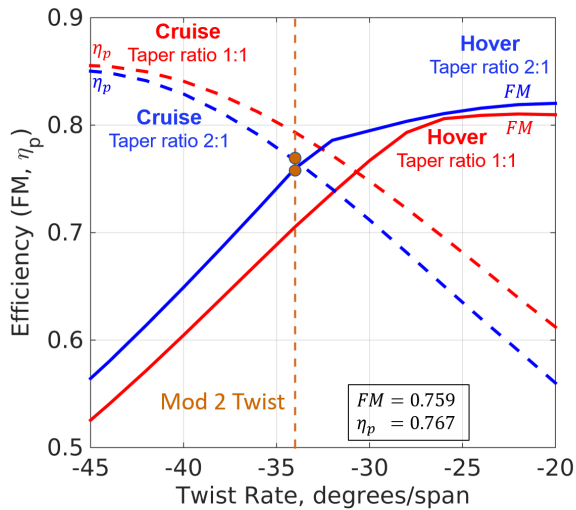
(a) Effects of reduced cruise tip speed on efficiency



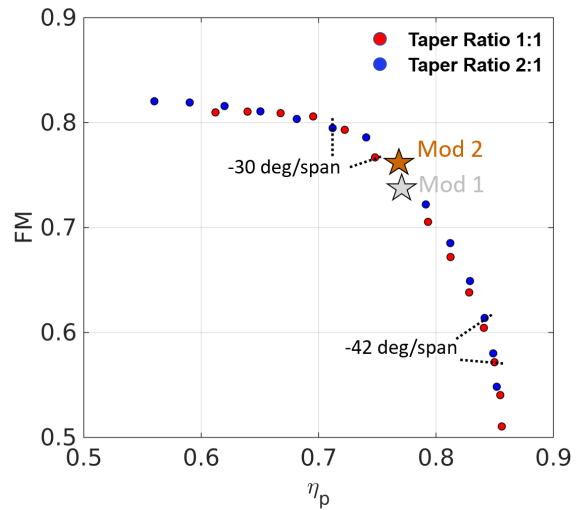
(b) Figure of merit versus propulsive efficiency

FIGURE 5.4: Effects of tip speed reduction on hover and cruise efficiency

results of the taper study, for baseline and 2:1 blade, are shown in Fig. 5.5(b). Figure of merit increases significantly with an increase in taper ratio for higher twist rates by decreasing the inboard angles of attack. A penalty was incurred during cruise with an increase in the taper ratio, due to increase in profile drag. However, the overall efficiency of the design increased. Consecutive studies were conducted with taper ratio of 2:1.



(a) Effect of taper.



(b) Effects of taper on efficiency metrics

FIGURE 5.5: Effects of taper on hover and cruise efficiency

5.3.4 Step 4: Blade Twist Selection

An approach to establishing a baseline bi-linear twist distribution for a prop-rotor blade is to align the blade sections with the local flow, based on the inflow encountered at the design cruise condition. Equation 5.5 was used to obtain non-linear twist distribution along the blade for



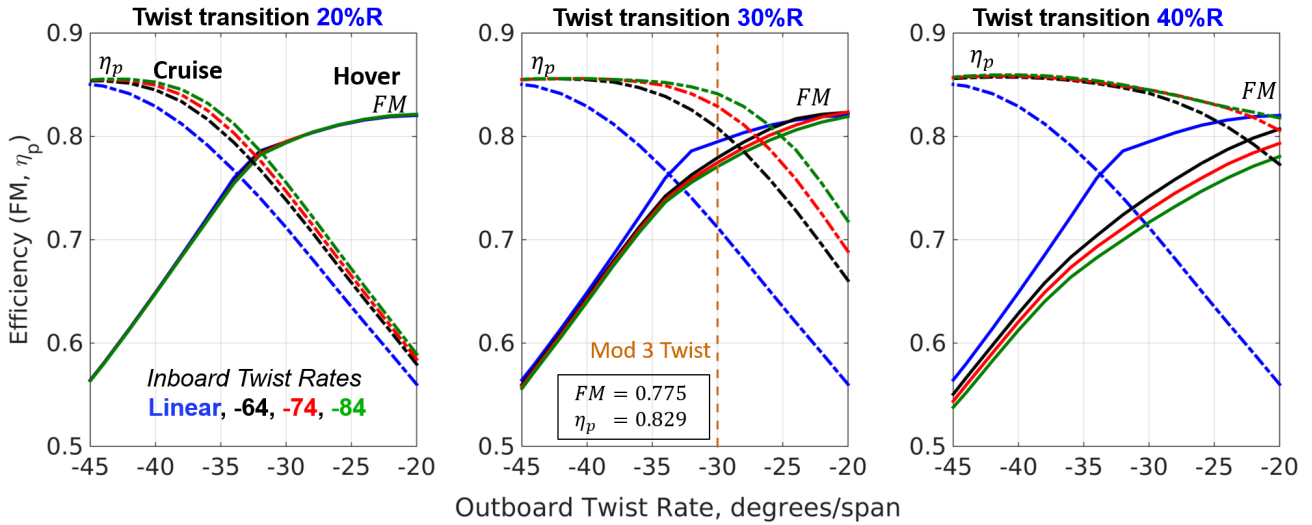


FIGURE 5.6: Effects of bi-linear twist on cruise efficiency

cruise [5], [6], [7]. In hover, this non-linear twist distribution creates extremely high angles of attack at the blade root. The non-linear twist can be approximated using two-piece, linear twist variation, joint at a particular spanwise station. Parametric studies were conducted to determine inboard and outboard twist slopes, as well as the twist transition location.

$$\varphi = \arctan\left(\frac{V_c + v_i}{V_{tip}}\right) \quad (5.5)$$

Figure 5.6 shows the results for the parametric studies which explored the effect of inboard and outboard twist rates and the transition location. Three inboard twist slopes that were compared are -64, -74 and -84 degrees/span. Outboard twist slopes ranged from -45 to -20 degrees. The transition locations that are investigated, as shown in Fig. 5.6, are $x/R = 0.2$, $x/R = 0.3$ and $x/R = 0.4$. Increasing the inboard slope and moving the twist transition outboard, significantly increases the efficiency in cruise, due to the alignment of the blade section with the local flow. In hover, the increase in the inboard slope and the transition location, decreases the figure of merit, because more of the blade is operating at large angles of attack. A blade design with an inboard twist rate of -74 degrees/span, an outboard twist rate of -33 degrees/span and a transition location at $x/R = 0.3$ was chosen for an the new baseline, favoring cruise efficiency. Further, parametric sweeps were conducted with this combination of parameters.

5.3.5 Step 4: Airfoil Selection

Parametric studies were conducted to first select the root airfoil, then midspan and finally the tip airfoil. Previous studies were conducted using only one airfoil, SC1095, along the blade span. However, the maximum thickness to chord ratio of SC1095 is 9.5 percent, which is not practical in the root region of the blade due structural reasons. Five root airfoils were considered for the root region of the blade: NACA0026, NACA2420, Clark Y, VR12 and VR7. The latter three were modified to have thickness to chord ratio of 20 percent, which was found to be sufficient to give the root blade structural functionality. The transition between the root airfoil and the midspan airfoil, SC1095, occurred at $x/R = 0.3$, the airfoil transition location was made to coincide with



the location of twist transition. SC1095 airfoil was implemented in the midspan and the tip of the blade for this parametric study, to isolate the effect of the root airfoil. Figure 5.7(a) shows the efficiency of the updated baseline blade (inboard slope = -74 degrees/span, twist transition = 0.3R) versus various outboard twist slopes for the five root airfoils. NACA0026, the thickest airfoil performed poorly compared to the other root airfoils due increased drag. NACA2420 and modified Clark Y performed the best out of the five airfoils which were considered. NACA2420 was chosen for the root section of the blade.

Once the root airfoil was chosen, a parametric study was conducted to determine the midsection airfoil. The root airfoil was kept constant while, the effects of the midspan airfoil were explored. Figure 5.8(b) shows efficiency comparison for various midspan airfoils, with a root airfoil, NACA2420. A blade with a combination of NACA2420 at the root and SC1095 outboard was chosen as a new baseline because it performed best out of the other combinations.

Finally, trade study was conducted to determine the effect of implementing a thinner airfoil at the tip. All of the tip airfoils had thickness to chord ratio of 8 percent, with an exception of the SC1095 whose thickness to ratio was 9.5 percent. The airfoil transition from midspan to tip happened at $x/R = 0.85$. Out of the five airfoils that were considered, VR8 provided additional increase in the efficiencies in both hover and cruise, as shown in Fig. 5.9, thus, VR8 was chosen for the blade tip.

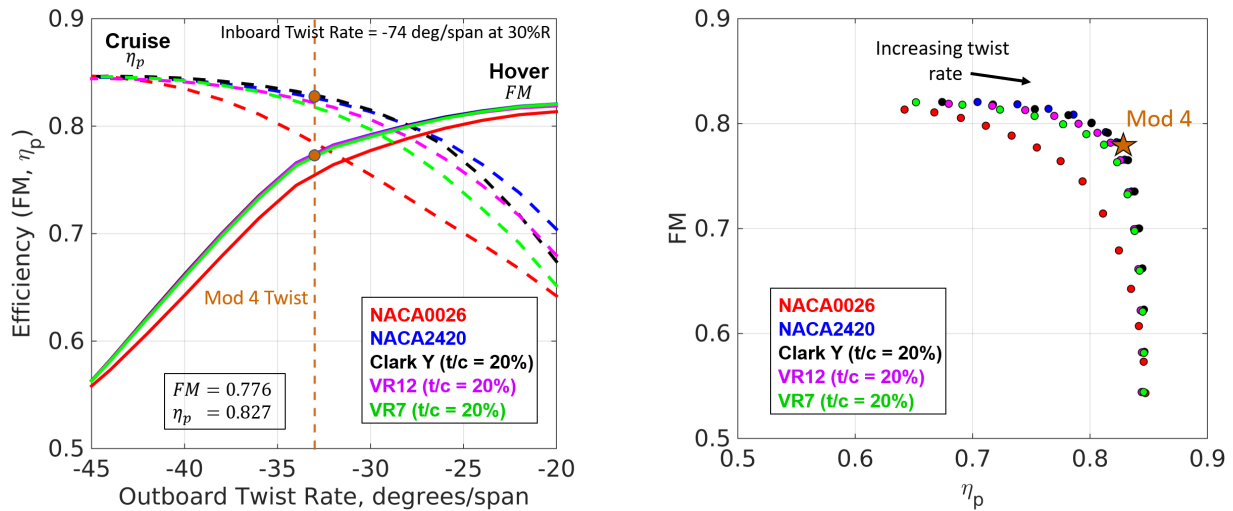


FIGURE 5.7: Root airfoil selection.

5.3.6 Final blade design

The final blade design consists of a blade with 2:1 taper, bi-linear twist and three airfoils along the span of the blade, shown in Fig. 5.1. The chord and twist distributions, with respect to $x/R = 0.75$, are shown in Fig. 5.10. The figure of merit and propulsive efficiency of the final blade are 0.768 and 0.832, respectively. The spanwise aerodynamic loading, for hover and cruise, on the *Metaltail* rotor blade is shown in Figs. 5.11(a) and 5.11(b). In cruise, the inboard part of the blade are operating an autorotative state, producing power, which contributes to the efficiency of the design in cruise. Spikes in airloads occur near the airfoil transition junctions because of lack of smoothing between the airfoil transition. The off-design performance, for hover and cruise,



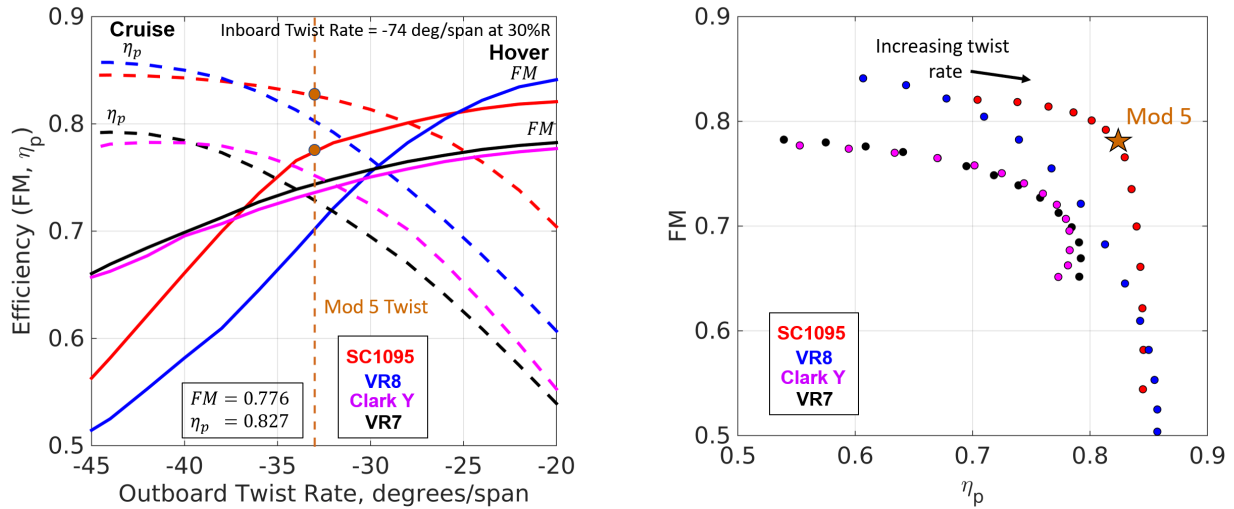


FIGURE 5.8: Midspan airfoil selection.

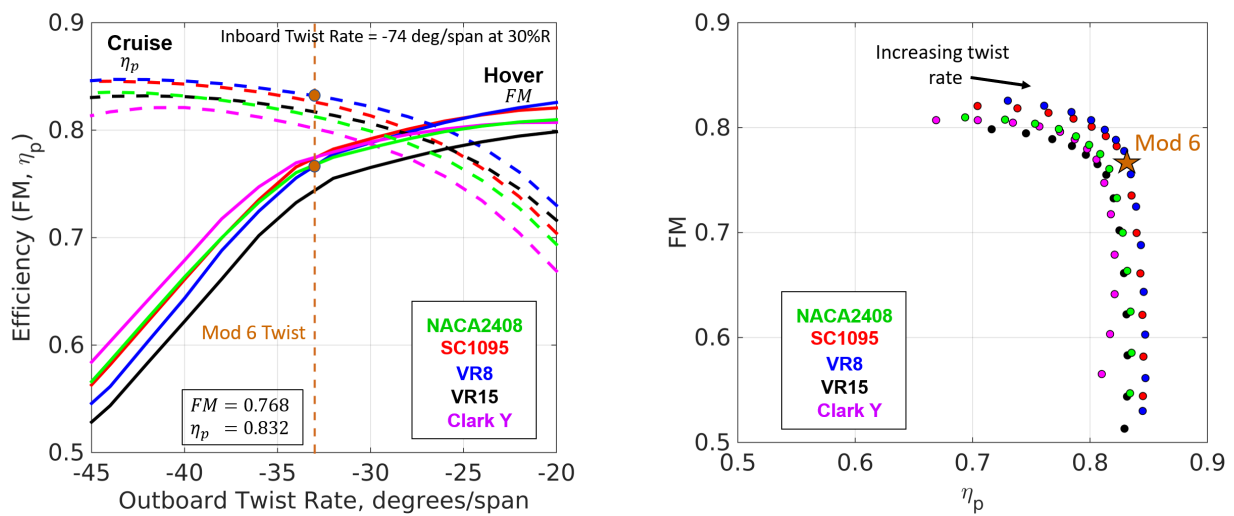
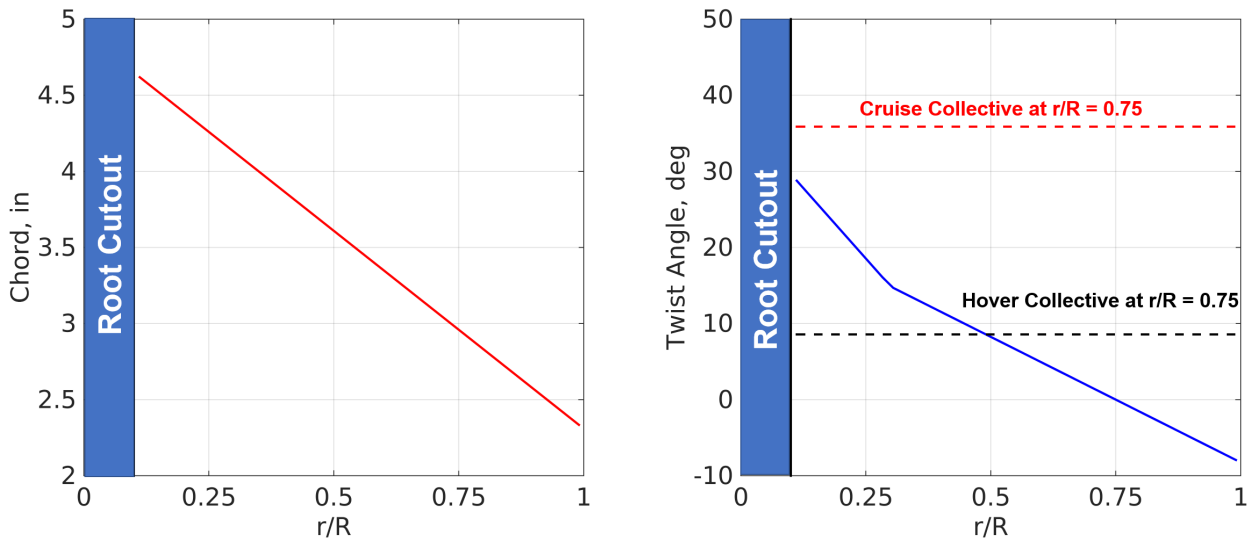


FIGURE 5.9: Tip airfoil selection

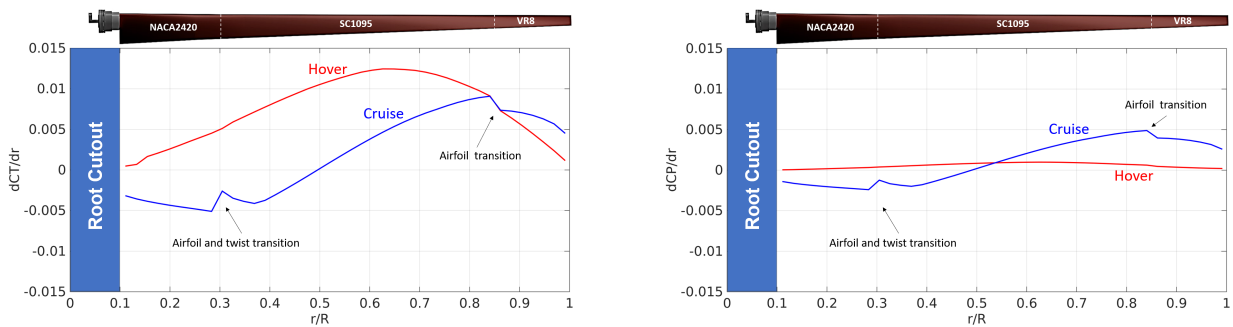
is shown in Fig. 5.12. Exceptional cruise performance is achieved for wide range of speeds, at various altitudes.





(a) Spanwise distribution of thrust on the *Metaltail* blade (isolated rotor). (b) Spanwise distribution of power on the *Metaltail* blade (isolated rotor).

FIGURE 5.10: Spanwise distributions on the *Metaltail* blade



(a) Spanwise distribution of thrust on the *Metaltail* blade (isolated rotor). (b) Spanwise distribution of power on the *Metaltail* blade (isolated rotor).

FIGURE 5.11: Spanwise distributions on the *Metaltail* blade

5.3.7 Coaxial Rotor Interference

Only an isolated rotor was considered in hover and cruise for the BEMT, at the design thrust coefficients without torque balancing. However, the *Metaltail* design employs a coaxial rotor with torque balancing. An in-house free vortex method analysis was used to quantify the effects of the coaxial rotor interference. The power per rotor, predicted using BEMT and FVM, is shown in 5.3. FVM predicts higher power for both hover and cruise. However, as shown in Table 5.3, if the BEMT is modified to account for the interference, using a typical interference factor of 1.15, BEMT predicts power within 2 percent of FVM. Therefore the designed blade works well in coaxial setting.



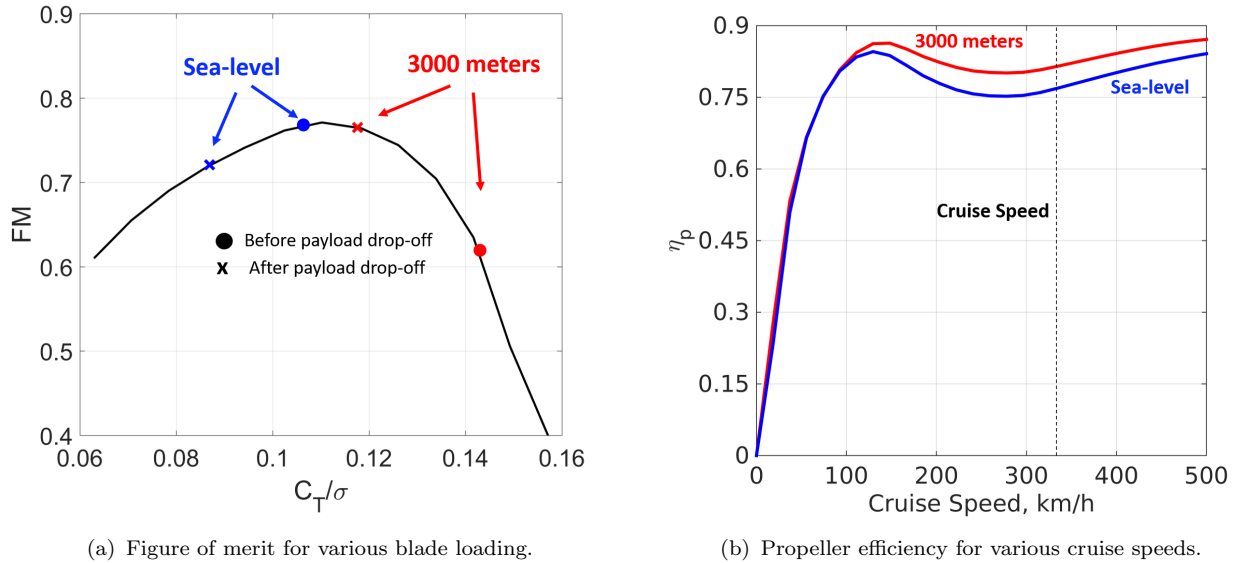
FIGURE 5.12: Off-design performance of *Metaltail* .

TABLE 5.3: Power prediction comparison from BEMT and FVM analysis.

Analysis	Hover Power, HP	Cruise Power, HP
BEMT (Isolated rotor)	59.2	50.5
BEMT (Coaxial, $K_{int} = 1.15$)	68.1	58.0
FVM (Coaxial)	69.6	57.7
% Error ($FVM_{coaxial} - BEMT_{coaxial}$)	2.2	0.5

6 Blade Structural Design

Blades of both upper and lower rotors of the coaxial system are shown in Figure 6.1. They consist of three major sections: wedge blade root with titanium sleeve, an inboard thicker section contributing most of the structural stiffness, and an outboard thinner section providing the primary part of the aerodynamic force. The only difference between upper and lower rotor blades are their root assemblies, which have different pitch horn lengths due to the control system design discussed further in Chapter 14. The internal structure, material selection and root structure are chosen such that the blades can withstand the hub moments generated during transition and during non-level trimmed flight, and have adequate tip clearance in edgewise flight.

6.0.1 Blade Root Structure

From 7% to 10% span of the blade is the root section, shown in Figure 6.2. A wedge root structure is chosen for the blade to maintain a clear airfoil shape while providing adequate root stiffness. The blade spar and the outer cylindrical titanium sleeve are connected through a wedge structure. Inside the outer sleeve, an inner titanium insert wedges up into the spar. The spar fibers are separated in multiple bundles and flared outwardly away from one another to facilitate the wedge structure. Tapered S-2 glass fiber wedges are inserted in between bundles of carbon fiber such that the fibers fill the cavity of the titanium outer sleeve. This design serves as a



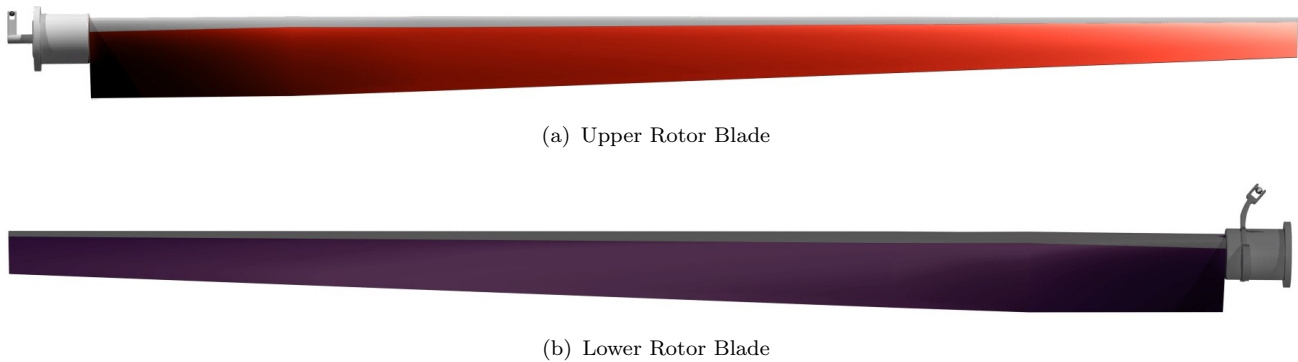


FIGURE 6.1: Rotor Blades

mechanical retention system preventing removal of the blades in outboard direction. The inner titanium base insert is pressed into the middle bundle to enclose the wedge and connected to the outer sleeve with bolts. The root assembly is connected to the hub through a thrust bearing and roller bearing which bear centrifugal force and bending moment, respectively.

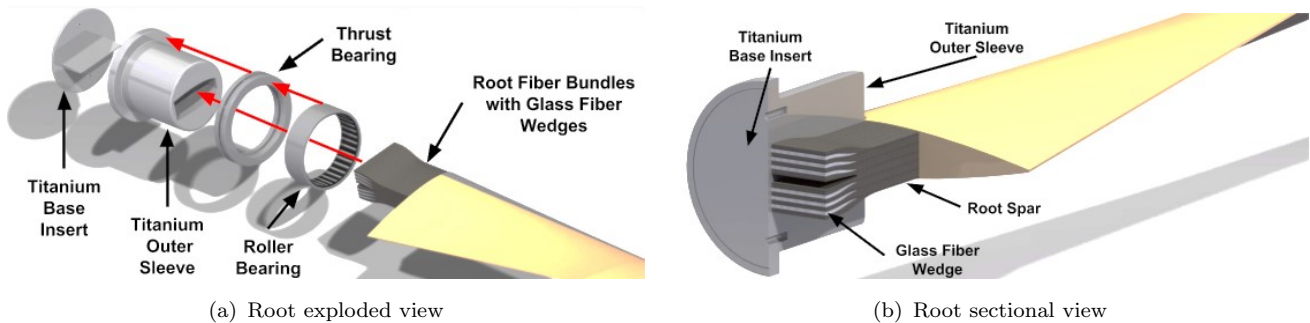


FIGURE 6.2: Anatomy of the blade root

6.0.2 Blade Internal Structure

Figure 6.3 shows the cross section of the blade. The D-spar is the major structural member transferring centrifugal force to the hub through the blade root. The flared fiber bundles of the root are converged into one bundle for the blade spar, which runs from 10% to 100% of the radius. A solid D-spar is designed such that the blade has high stiffness for a relatively small chord varying from 11.1 cm at the root to 5.56 cm at the tip. The spar is located from 2% to 35% of the chord and is composed of a bundle of unidirectional $[0^\circ]$ plies of T300 graphite-epoxy prepreg. The center of gravity is set at 0.2% ahead of the quarter-chord by distributed Internet IT170 tungsten alloy leading edge masses. This gives some margin to blade stability in case of moisture in foam core material. For the aft core material of the blade, Kevlar honeycomb and Rohacell 75 foam were studied and compared. Even though Kevlar honeycomb has a lower density (33.6 kg/m^3) compared to Rohacell 75 foam (74.97 kg/m^3), machining honeycomb to fit inside a small space like the core of the blade is less practical. Also, we want a higher density because blades are too light and have low inertia. Therefore, Rohacell 75 foam was chosen to be the core material to preserve the airfoil shape of the blade cross section. The trailing edge block is also made from a bundle of unidirectional fibers of T300 graphite-epoxy prepreg to reinforce the trailing edge of the blade. The blade skin is composed of two bidirectional $[\pm 45^\circ]$ plies of T300 graphite/epoxy. The skin provides the majority of torsional stiffness and chordwise stiffness.



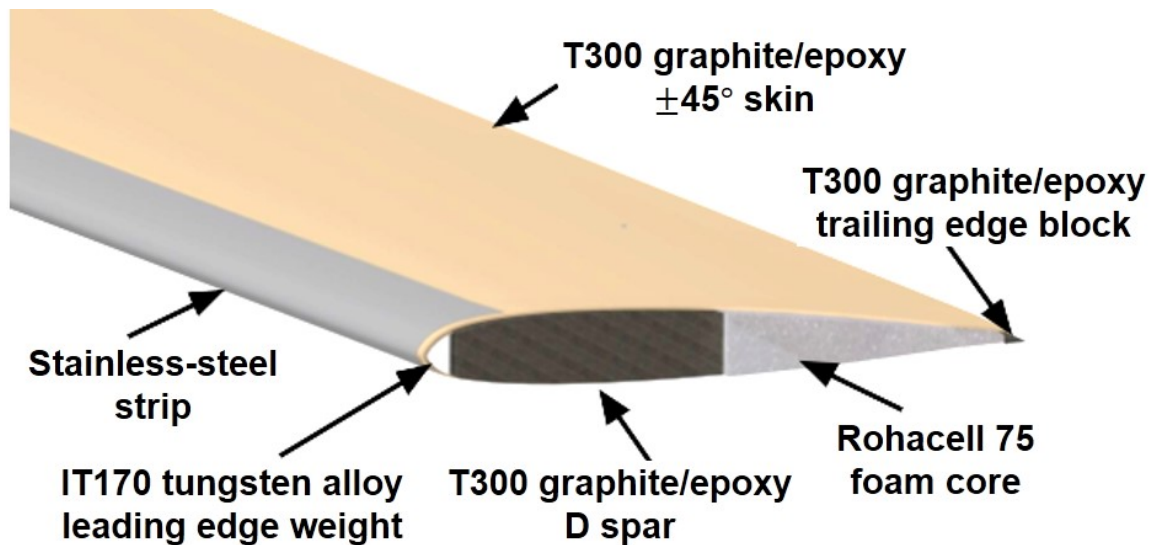


FIGURE 6.3: Inner blade structure and materials

Outside of the carbon fiber plies, the blade is coated all over with polyurethane elastomer to prevent wear and erosion, then wrapped with a copper mesh to protect the blade from static buildup and lightning. Finally, the blade has a stainless-steel strip on its leading edge to protect it from abrasions.

6.0.3 Blade Manufacturing

The blade spar, root section with wedge structure, and the titanium sleeves are fabricated as one part. Layers of the root section fibers run through the opening of the outer sleeve before they are inserted with glass fiber wedges to produce the flaring bundles. The inner sleeve is then inserted and bolted to the outer sleeve. Then the root assembly and blade spar are placed in a vacuum mold and cured in an autoclave.

While the spar is curing, the leading-edge weights and trailing-edge foam can be machined. Once those components are complete, the leading-edge weight, spar, foam and trailing-edge block are glued one after the other. The assembly is wrapped with two plies of bidirectional [45] graphite-epoxy prepreg. A mold with a shallow indent on the leading edge for the placement of stainless steel strip is needed for final curing in an autoclave. Ultrasonics is employed to do a final check for any major type of defects in the blade.

6.0.4 Rotor Blade Sectional Properties

Figure 6.4 shows the non-dimensional mass, flap stiffness, lag stiffness and torsional stiffness distribution along the elastic axis of the blade. The clamped cantilever condition is applied at the blade grip at 10% radius. The section per unit length mass and stiffness distribution decrease as the section moves outboard. This behavior is caused by the variation in chord and airfoils. The inboard NACA2420 airfoil section spans from 10% to 28.5% radius and the outboard SC1095 airfoil section spans from 32.5% to 100% radius. The transition between inboard and outboard airfoil takes place from 28.5% to 32.5% radius. Based on the cross-sectional analysis, the total weight of an individual blade is $1.057kg$.

Tuning the blade structural frequencies to desired values in both hover and forward flight



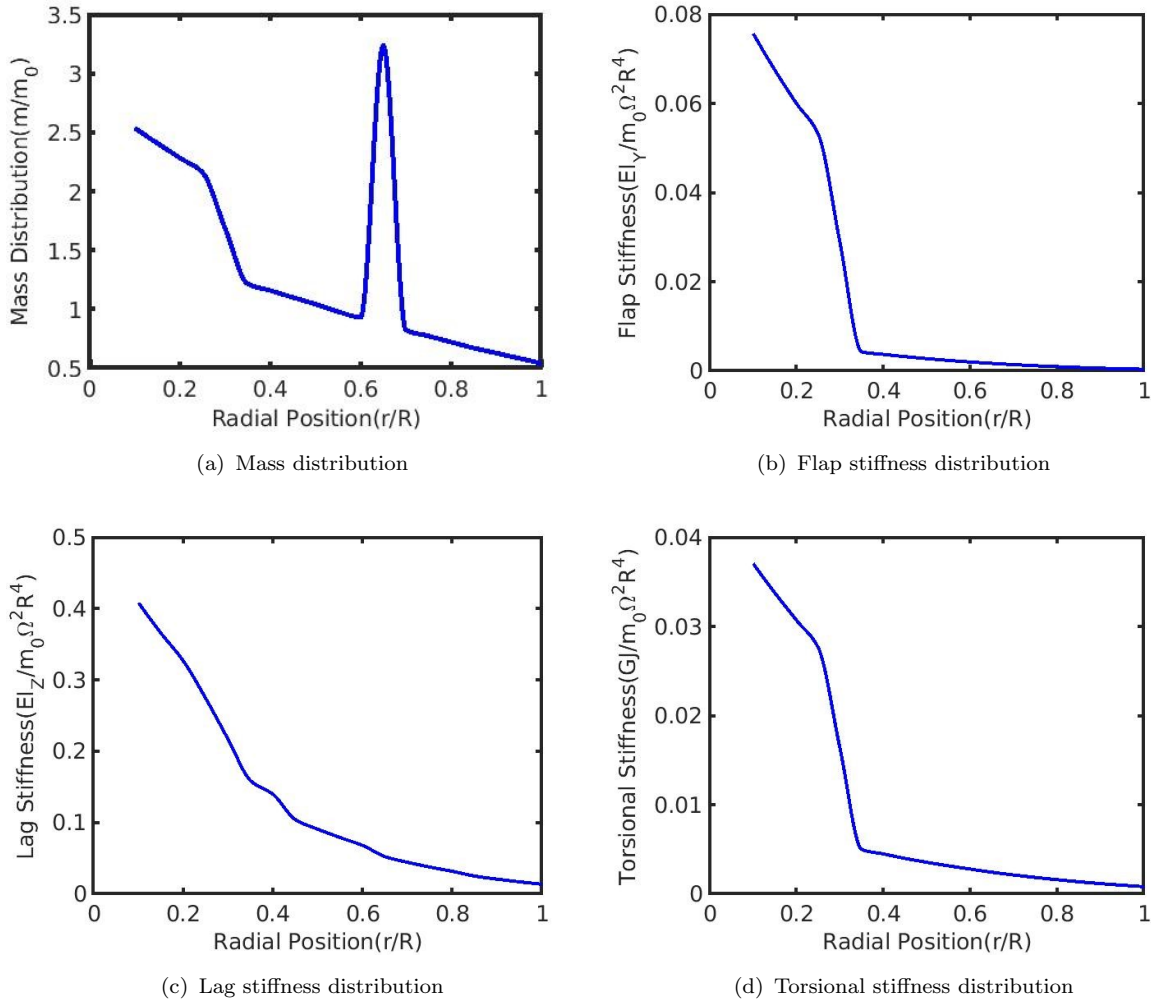


FIGURE 6.4: Sectional properties along the blade

operational RPMs is especially important for a proprotor. Variables such as spar type, chordwise position of spar, thickness of spar and skin, size of trailing-edge block and leading-edge masses were studied. An antinode mass is added to 62.5%-67.5% radius to tune down the third flap frequency. Fan plots of rotor blade in the vehicles operational rotor speed range at hover and cruise are shown in Figures 6.5(a) and 6.5(b). The fan plot shows that the first four frequencies of flap/lag modes will not excite any 1-8/rev harmonics at any of the operating RPMs of the rotor. Due to the highly coupled behavior of the flap and lag modes, the frequencies are labeled with the dominant mode first, displayed in Tables 6.1 and 6.2. Based on the first flap frequency in hover, a control phase angle of 64.4° is desired to decouple the longitudinal and latitudinal cyclic controls. This, together with space limitations guided the design of the pitch horn lengths. By tuning the pitch link stiffness, a $7.34/rev$ first torsion frequency was obtained for both the upper and lower rotor blades.

6.0.5 Aeroelastic Analysis

Metaltail has highly twisted rotor blades. Therefore, it is vital to ensure flap-lag coupling does not cause any instabilities in the operational envelope of the rotor. The root loci produced by an eigen-analysis of flap-lag instability for the proprotor operating in hover mode and cruise



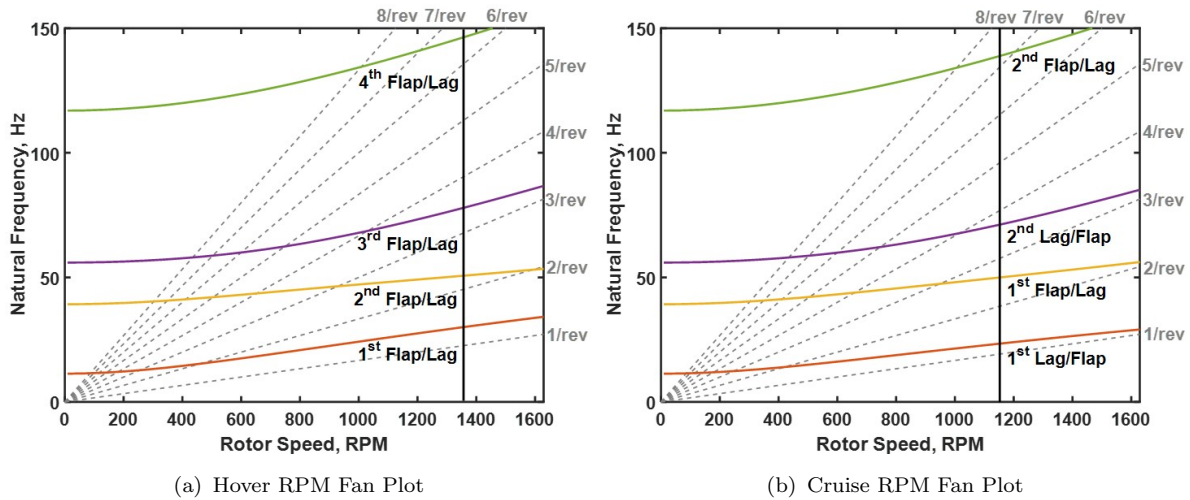


FIGURE 6.5: Fan plots displaying frequencies at hover and cruise RPM

TABLE 6.1: First five rotor frequencies at hover RPM

Frequency (/rev)	Hover 1369 RPM
1 st Flap/Lag	1.33
2 nd Flap/Lag	2.24
3 rd Flap/Lag	3.45
1 st Torsion	7.34
1 st Lag/Flap	9.37

TABLE 6.2: First five rotor frequencies at cruise RPM

Frequency (/rev)	Cruise 1163 RPM
1 st Lag/Flap	1.22
1 st Flap/Lag	2.60
2 nd Lag/Flap	3.70
2 nd Flap/Lag	7.22
1 st Torsion	8.54

mode are shown in Figure 6.6(a). The result indicates that the proprotor is stable throughout its operating envelope. The analysis was conducted without considering the blade structural damping, which provides a conservative estimate. Including any structural damping in the analysis will result in a larger stability margin. Pitch-flap flutter and pitch divergence instabilities were considered as well. Pitch-flap coupling occurs when the center of gravity (c.g.), center of pressure, the elastic axis of the blade cross section are not coincident. Hence, instability of such kinds can be mitigated by adjusting the c.g. position carefully. Figure 6.6(b) shows that *Metaltail's* operating envelope avoids the unstable boundaries of pitch-flap flutter and pitch divergence by having a torsional frequency of 7.34/rev at hover and 8.54/rev at cruise and a c.g. at 24.8% of the chord.

6.0.6 Ground and Air Resonance

Metaltail's proprotors are stiff-in-plane with rotating lag frequencies greater than 1.0 in all operating conditions. Therefore, instabilities such as air resonance, which involves coupling of rotor modes and aircraft body modes, and ground resonance, caused by the coupling of blade lag modes and landing gear modes, are not a concern in *Metaltail's* design.

6.0.7 Tip Clearance

With coaxial rotors, the risk of blades striking must be considered. *Metaltail* rotors are placed 0.15 m or 10% of the radius apart on the hub. Figure 6.7 tracks an upper rotor blade and a lower



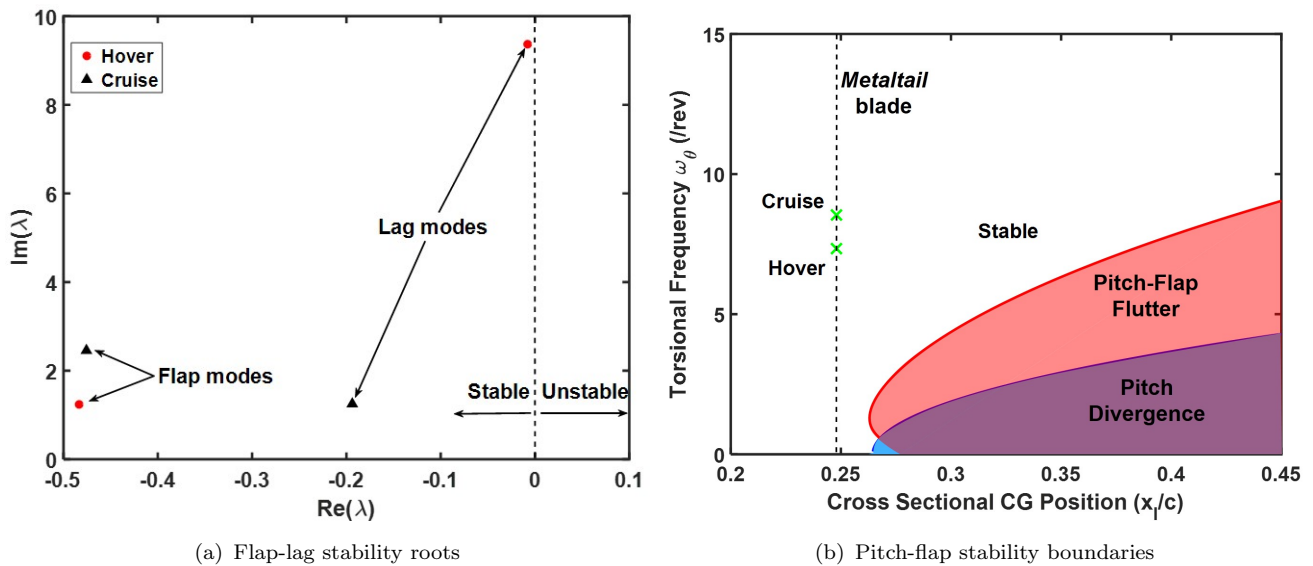


FIGURE 6.6: Aeroelastic Stability Boundaries

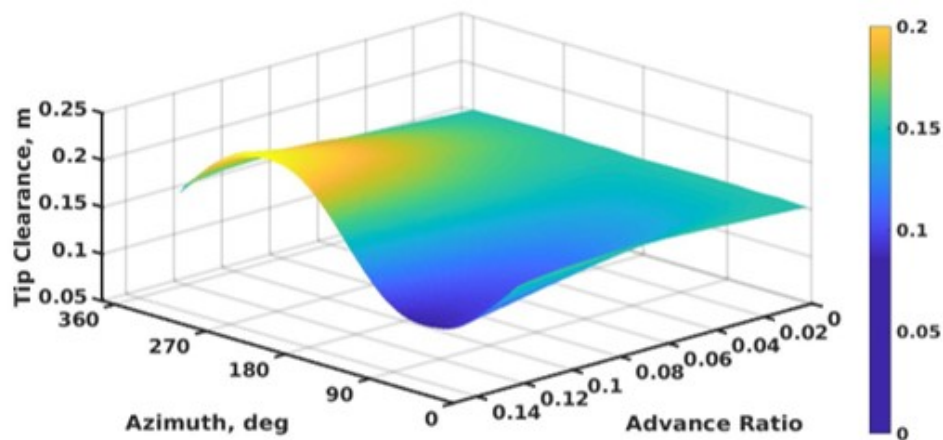


FIGURE 6.7: Tip clearance between upper and lower rotor blades

rotor blade as it travels around the azimuth for edgewise transition flight, as this scenario provides asymmetric lift distribution. Based on the transition trim result discussed in Section 14.2, the maximum advance ratio in edgewise transition is 0.124. The tip clearance is calculated using the University of Maryland Advanced Rotorcraft Code (UMARC). The minimum blade tip clearance of 8.4 cm occurs at 95° azimuth and advance ratio of 0.122. This tip clearance provides an adequate margin for maneuvers or gusts.

6.0.8 CSD/CFD Analysis

Using X3D, a rotor structural dynamics solver with integrated 3D computational fluid dynamics, the rotor blade root and blade were analyzed to determine their axial structural loads and safety factors based on Tsai-Wu failure criteria. Figures 6.10 and 6.9 show these results. Stresses are shown in units of pascals; blade root experiences up to 90 MPa of stress and the blade experiences up to 30 MPa. Figure 6.10(b) shows a minimum fatigue safety factor of 2.23 in the blade root, and Figure 6.9(b) shows a minimum failure safety factor of 2.08 in the blade.



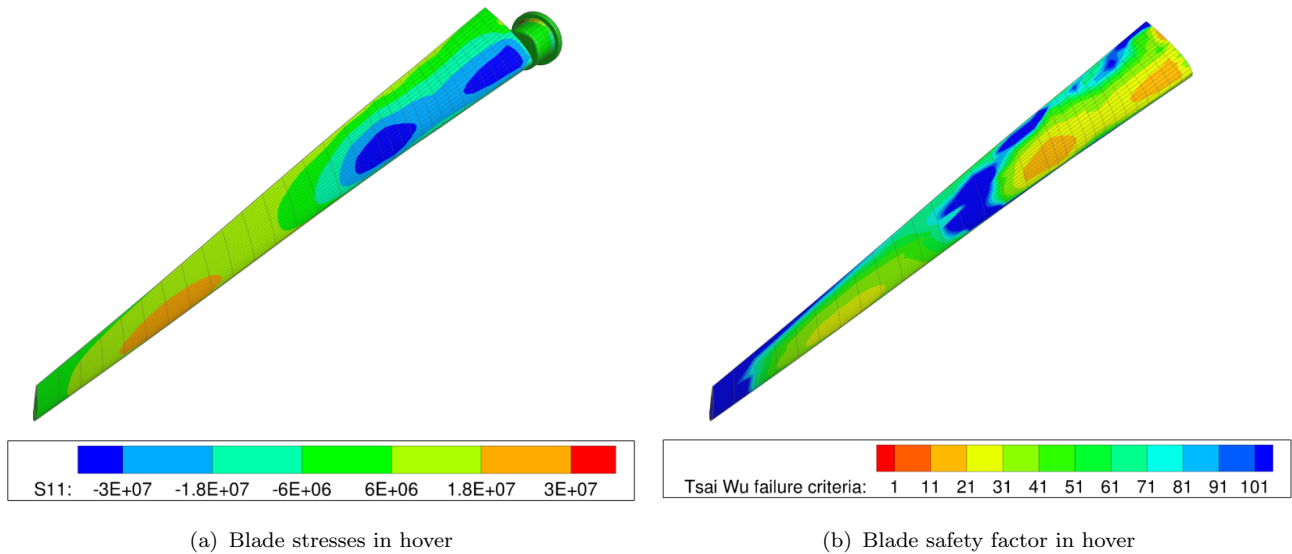


FIGURE 6.8: X3D analysis of rotor blade in hover

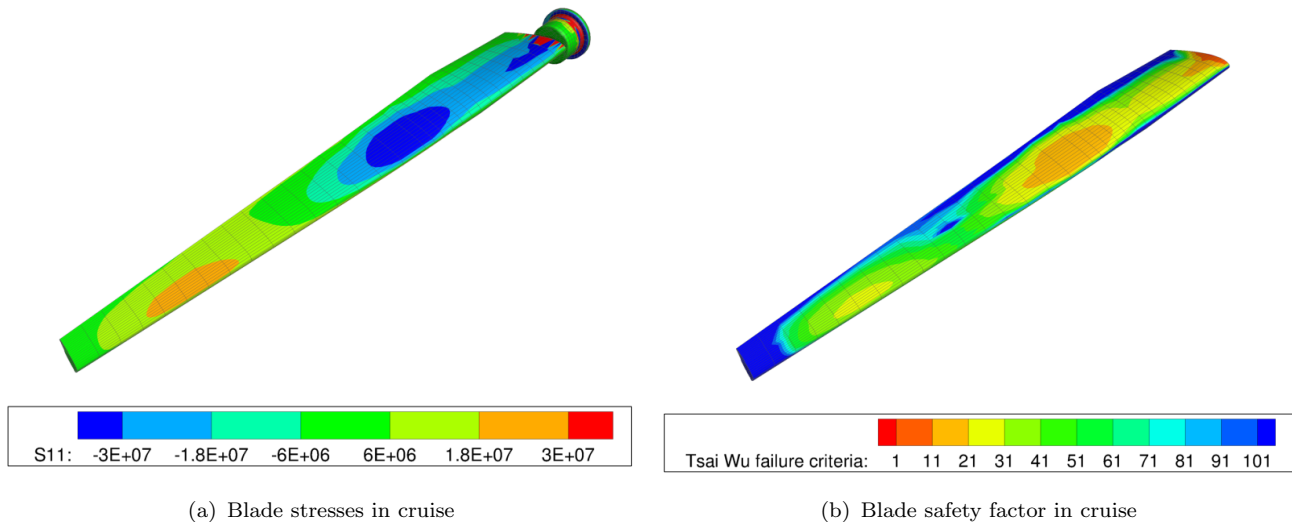


FIGURE 6.9: X3D analysis of rotor blade in cruise

The minimum safety factors confirm that the rotor blade roots and blades are not susceptible to composite ply failure or root sleeve fatigue failure.

7 Hub Design

7.1 Hub Selection

A hingeless hub was selected for *Metaltail*. There are four major criteria that *Metaltail's* hub needed to satisfy. First, as a tailsitter vehicle, *Metaltail's* transition between helicopter mode and fixed wing mode is a key feature. In order to start transition from hover, an initial pitching moment must be produced at the hub. For the vehicle to stay controllable and stable during transition, a hub pitching moment is required to counteract the moment produced by lifting surfaces to obtain moment equilibrium. That means the hub system needs to have enough



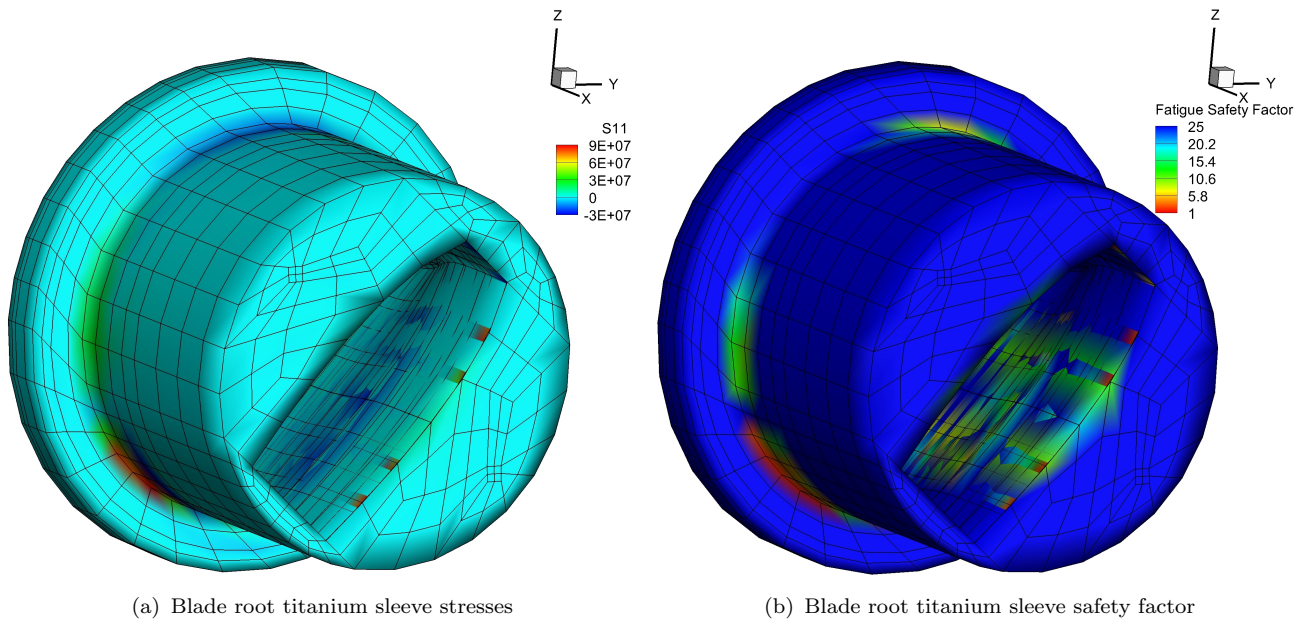


FIGURE 6.10: X3D analysis of rotor blade root

authority to generate and transfer hub moments to the body of the aircraft. Second, tip clearance is an essential consideration in the design of a coaxial rotor system that experiences edgewise flight. The rotor should provide adequate stiffness to prevent potential blade strike in the entire operating envelope. Third, *Metaltail's* rotor is designed to operate in both edgewise flow and high-speed axial flow, which requires a larger collective pitch range that allows the vehicle to efficiently hover at a Figure of Merit of 0.776 and efficiently cruise at a propulsive efficiency of 0.827. Lastly, compactness of the hub is considered in order to decrease drag area and achieve a high forward flight speed. Gimbaled, articulated, semi-articulated, and bearingless hubs all are unable to satisfy the requirements as shown in Table 7.1

TABLE 7.1: Hub Selection

Type of hub	Hub Moment	Tip Clearance	Collective Pitch Range	Compactness	Score
Gimbaled	-	-	+	-	+1
Articulated	-	-	+	-	+1
Semi-Articulated	-	-	+	-	+1
Bearingless	+	+	-	+	+3
Hingeless	+	+	+	+	+4

7.2 Hub Assembly

Figure 7.1 shows the assembly of the proprotor hub and blades. The proprotor is a coaxial system composed of a lower rotor assembly driven by a lower rotor shaft, and an upper rotor assembly driven by an upper rotor shaft. The lower rotor shaft is hollow and allows for the upper



rotor shaft to extend through the interior of the lower rotor shaft. The upper rotor assembly includes four upper rotor blades connected to the upper rotor hub.

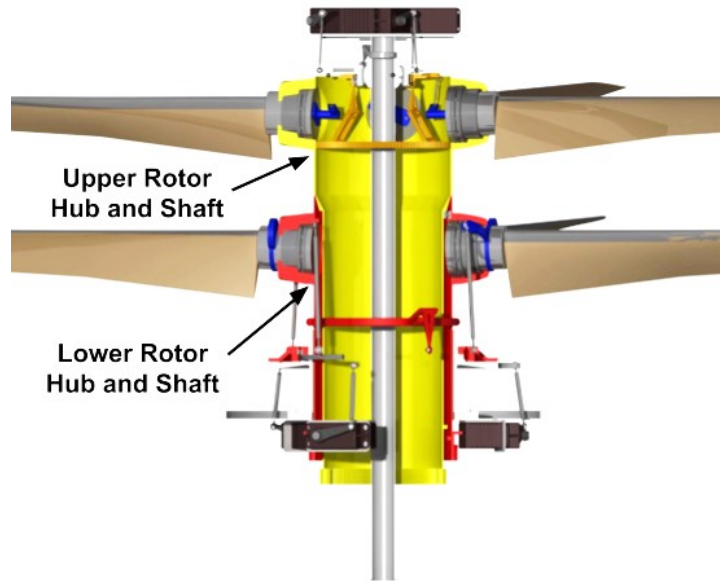


FIGURE 7.1: Rotor hub assembly

As shown in Figure 7.2(a), each upper rotor blade is placed in a bearing house on the hub with a thrust bearing and a roller bearing, which bears centrifugal force and bending moment, respectively. The roller bearing also allows the blade to rotate about its pitch axis. The blade root is sandwiched by the bearing housing, shown in Figure 7.3, which is fastened together with bolts. A pitch horn is assembled at the root of each inner sleeve located inside the upper rotor shaft and connected to the upper swashplate with a pitch link. The lower rotor assembly is similar to the upper rotor, except the pitch horn of the lower rotor is located outside the shaft. Moments acting on the two rotors are shared by two roller bearings in the gap between the inner and outer shafts.

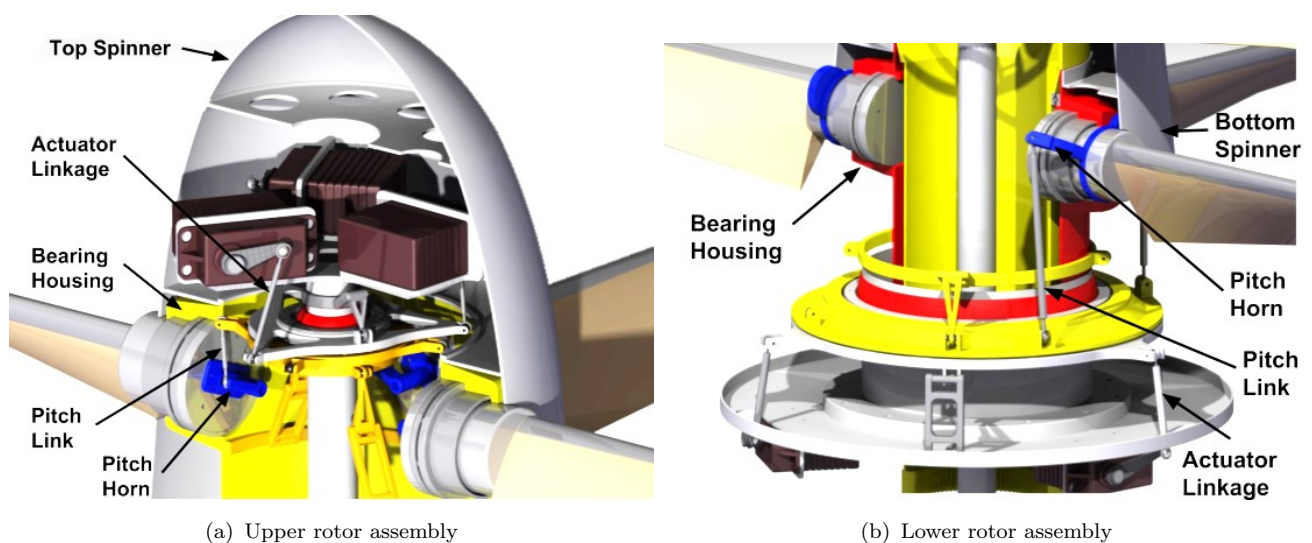


FIGURE 7.2: Pitch horn and pitch link assemblies of each rotor

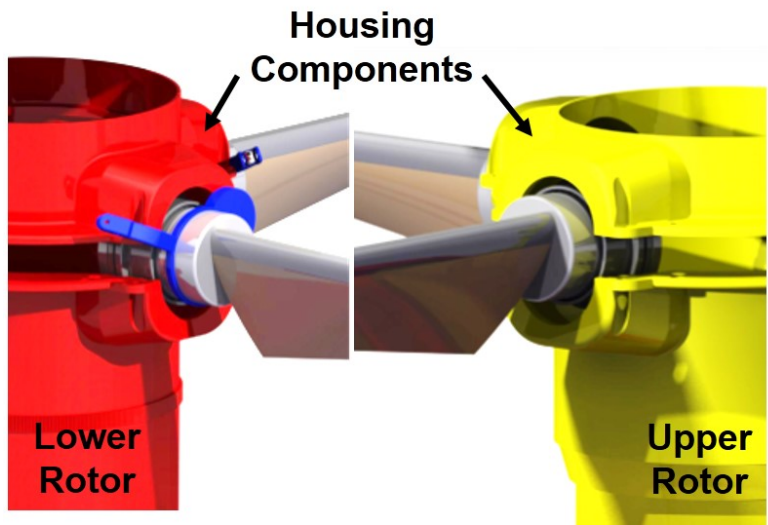


FIGURE 7.3: Bearing housing components clamp rotor blades to hub

Forces from the rotors are transmitted to the fuselage through a thrust bearing and a roller bearing between the gear housing and bevel gears located below the first bulkhead shown in Figure 7.4.

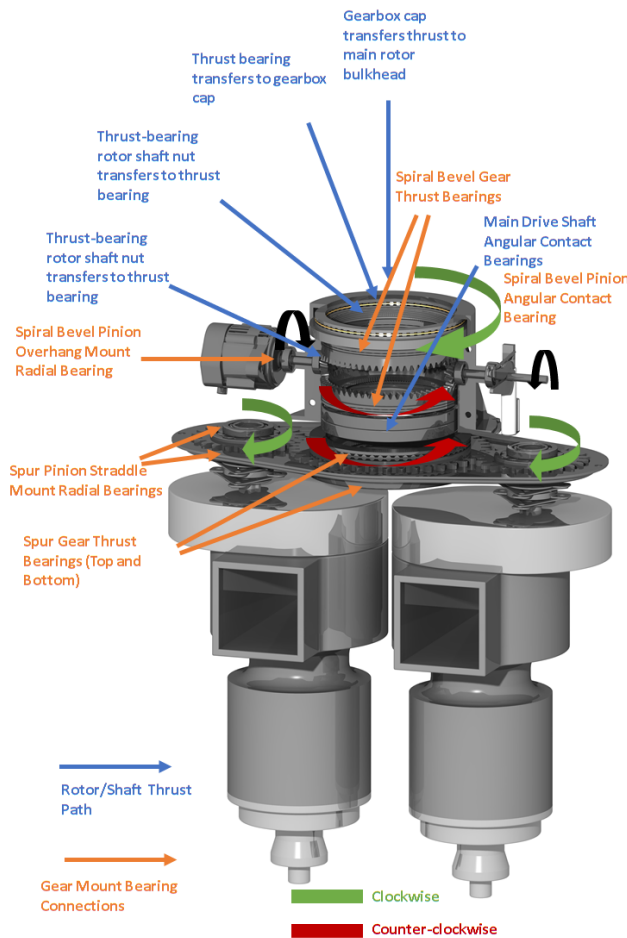


FIGURE 7.4: Rotor load path through transmission gear housing



7.3 Swashplate Design

Two swashplates, installed separately, one inside the top end of the upper rotor shaft, and one outside the lower rotor shaft were chosen because of their simplicity and reliability. Various collective and cyclic control systems were considered for the coaxial proprotor. *Metaltail* is designed to operate in a megacity environment, which demands exceptional control authority to maneuver in city streets and tolerate gusts. A coaxial rotor by nature is more mechanically complex than a single rotor; therefore, reliable, safe, and simple designs for the control system were preferred. Assessments of different control systems are shown in Table 7.2.

TABLE 7.2: Swashplate Selection

Control system	TRL	Simplicity	Compactness	Low Weight	Cyclic Pitch Range	Score
Traditional Coax Swashplate	+	-	-	-	+	+2
Sikorsky Aircraft Corp Patent US7585153B1	+	-	+	+	-	+3
Sikorsky Aircraft Corp Patent US8979495B2	+	-	+	-	+	+2
Individual Blade Control	-	+	+	-	+	+3
<i>Metaltail</i> Design	+	+	+	+	+	+5

The traditional coaxial control system can be found on a Kamov Ka-31 or Ka-52. It has been adopted since the 1980s and has a high technology readiness level. However, the exposed linkage and mechanical complexity are major barrier for *Metaltail*. Those features not only cause a large hub drag but also makes the system less reliable by having many small parts that may potentially fail. The second and third swashplate designs are Sikorsky patents. Both have a conventional swashplate for the lower rotor, but the difference is in the control of the upper rotor. The former patent employs a control rod placed inside the upper rotor shaft to elevate (collective pitch) and tilt (cyclic pitch) a pitch beam. The control rod is actuated by a servo located at the bottom of the rotor shaft and a X-Y positioner located inside the rotor shaft. Its primary disadvantage is that the size of linear actuator in the X-Y positioner is limited by the inner diameter of upper rotor shaft, which limits the control force an actuator can provide. The latter patent uses long actuator links passing through from one end of the shaft to the other to control the spider system located at the top of the rotor shaft. Long actuator links are traditionally designed with larger diameters to prevent buckling, which increases the weight of the system. Moreover, both of these patents have all actuators located below the rotor shaft. This is acceptable for a conventional helicopter, where the gearbox output shaft is normally connected to the rotor shaft from the side via a bevel gear, which provides space right below the shaft for actuators because *Metaltail's* rotor shaft is aligned with the gearbox output shaft, placing every actuator below the shaft will require a longer shaft resulting in a lengthened body. As for individual blade control (IBC), hydraulic actuators are needed to replace pitch links and swashplate. These actuators are required to have a high actuation rate (one cyclic per revolution) and to provide adequate torque to counter the pitching moment generated by each blade. All these requirements lead to relatively large and heavy actuators with a hydraulic support system.



From the resulting assessment, *Metaltail* keeps a conventional swashplate for the lower rotor shown in Figure 7.5(a). Another swashplate is modified to fit inside the upper rotor shaft, and rotated upside-down to allow control inputs from actuators placed above the rotor shown in Figure 7.5(b). A stationary stand is designed to support all non-rotating parts of the upper swashplate, including the non-rotating swashplate, non-rotating scissor link and servo motors. The stand travels all the way through the drivetrain and shares the same bulkhead with the reduction gearbox.

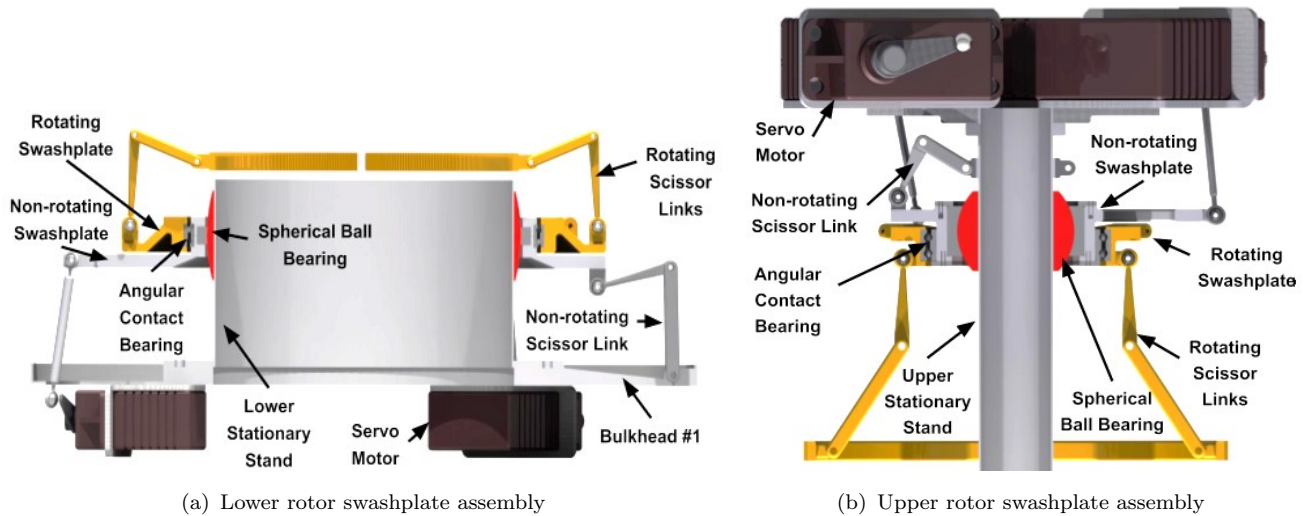


FIGURE 7.5: Swashplate assemblies

The non-rotating swashplate clamps onto the outer ring of the spherical ball bearing which is concentric with the upper swashplate stand. The spherical ball bearing allows the swashplate to slide along the shaft and enables cyclic tilting motions. A single scissor linkage connects the swashplate and non-rotating stand to prevent rotational motion of the non-rotating swashplate. It clamps onto the stand through a splined collar that meshes with matching splines on the stand. There are two angular contact bearings placed between the non-rotating and rotating swashplates to transfer control loads. A pair of scissor links clamp onto the rotor shaft from the rotating swashplate using the same method as the non-rotating scissor link, providing a path to transfer torque from the rotor shaft to the swashplate. The whole assembly allows the swashplates to spin freely with respect to each other with independent inputs from the control system.

8 Propulsion System

To fulfill mission requirements, meet aircraft performance goals and provide sufficient power for all desired maneuvers, the *Metaltail* propulsion system was designed to power coaxial rotors capable of hover, transition and forward flight at altitudes up to 3000 m and speeds of at least 371 km/h with full payload and fuel with as much range and endurance as possible. This chapter details the the selection and design of the power plant and transmission along with descriptions of their components and accessories.

8.1 Power Plant Design

Metaltail's mission and design requirements are oriented toward increasing speed and efficiency in a small vehicle. The power plant design was primarily driven by the need for a combination of high specific power and specific energy in a limited fuselage volume to achieve hover with a limited diameter (3 m) rotor and improve dash speed and range.

8.1.1 Configuration Study

The power plant configurations below were evaluated on approximate overall weight of the engine/motor and fuel/batteries, with additional consideration for power density and its effect on transmission and fuselage geometry. The Stuttgart Engineering STV130 turboshaft engine can be seen in Figure 8.1 to have lower combined weight than leading examples of other configuration types over all *Metaltail's* intended mission ranges.

- **Gasoline Spark-Ignition Engines** typically have better specific fuel consumption than turboshaft engines (0.25-0.35 kg/kWh) at the installed power required for the *Metaltail*, but suffer from lower specific power values (about 1.0-1.5 kW/kg). The [insert final max required power here] maximum power requirement for *Metaltail* ruled out the use of gasoline engines, with installed weights over 25% of MTOW.
- **Diesel Cycle Engines** typically have the lowest specific fuel consumption and lowest specific power of all fossil fuel engines at the Group 3 scale. Similar to the spark-ignition, Diesel cycle engines were eliminated from consideration due to their low specific power (about 0.8-1.25 kW/kg).
- **Battery-Electric** drive trains utilize electric motors with high specific power (the Siemens-Airbus eFusion demonstrator engine reached 5.2 kW/kg) compared to microturbine, reciprocating or rotary engines. However, modern high-power lithium-ion batteries are limited to pack densities of approximately 0.180 kWh/kg, and thus battery weight increases overall weight beyond that of combustion engine systems.

High energy-density Aluminum-air batteries improve endurance with specific energy values up to 1.8 kW-hr/kg, but were also ruled out as the 200 W/kg specific power cannot support vertical flight on the *Metaltail's* 3 m rotors. Hybrid combinations of the two battery types also produced either insufficient power or higher weight than turboshaft options.

- **Series Hybrid-Electric** drive power plants can eliminate the need for a mechanical transmission, saving complexity and weight. However, a coaxial, counter-rotating rotor increases the complexity of an electric motor-driven design and the weight of an electric motor for the *Metaltail's* configuration exceeds that of the mechanical transmission.
- **Parallel Hybrid-Electric** drive trains utilizing turboshaft engines in parallel with a limited-duty electric motor and low-endurance battery pack enables the use of a single recuperated microturbine (rather than two) and enables vertical to forward flight transition through the use of an electric motor temporarily boosting power to the rotors. It also improves autorotation performance in case of engine loss. However, the motor and battery pack increase weight over that of a second turbine at this scale while reducing the available time at maximum power.



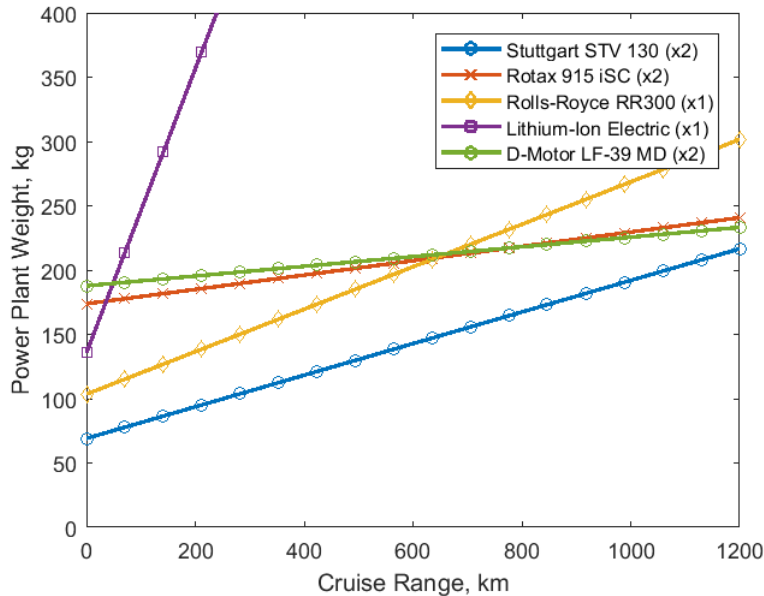


FIGURE 8.1: Approximate fuel + engine weight vs. cruise range (10 minutes total hover time)

TABLE 8.1: Comparison of turboshaft engine options for the *Metaltail*

	Stuttgart STV 130	PBS TS 100	Rolls-Royce RR300
Take-off Power, kW (HP)	96.94 (130)	180 (241)	224 (300)
Max Continuous Power, kW (HP)	77.55 (104)	160 (214)	179 (240)
SFC, $\frac{kg}{kWh}$ ($\frac{lb}{HP \cdot hr}$)	0.33 (0.54)	0.516 (0.847)	0.41 (0.67)
Dimensions, mm	555(L) x 280(D)	820(L) x 330(W) x 398(H)	828(L) x 546(D)
Weight, kg (lb)	30 (66)	61.3 (135)	91.2 (201)
Specific Power, kW/kg (HP/lb)	3.23 (1.97)	2.94 (1.79)	2.46 (1.49)
Output RPM	2500	2158	6016

- **Heavy-Fuel Turboshaft Engines** benefit from high generator specific power and fuel specific energy. At low installed power ratings, turboshaft engines suffer from low maximum pressure ratios due to minimum tolerance limits. At the microturbine scale (25-500 kW), exhaust energy recuperation systems can increase fuel efficiency by as much as 40% [8]. Research into applications of this technology previously suspended due to low fuel prices in the 1980s has restarted to improve Group 3 and 4 UAS performance, where there is a growing demand for microturbine engines.

8.1.2 Turboshaft Engine Selection

Multiple turbine engines in the 50-250 kW range were compared based on specific power, efficiency and size to determine the best available option. A subset of the analyzed engines representative of the range of sizes, efficiencies and power ratings are displayed in Table 8.1.

The STV 130 has the lowest specific fuel consumption (SFC) at predicted cruise and hover power settings. It also has the shortest length - aiding in aircraft longitudinal CG placement - and the



highest specific power. The *Metaltail* uses two engines to provide sufficient required power for hover and transition. A two-engine design also provides redundancy for flight over populated areas, allowing a safe landing in the event of an engine failure in hover and the ability to maintain altitude in forward flight on one engine.

8.1.3 Stuttgart Engineering STV 130 Turboshaft

The Stuttgart Engineering STV 130 (Figure 8.2) is a free-turbine, recuperated turboshaft engine with a single-stage compressor and single-stage power turbine. A recuperation system lowers specific fuel consumption by about 40% versus an unmodified Brayton cycle turbine such as the TS100 by increasing combustor inlet temperature. Similar recuperated engines are now in development with equal or better efficiency, including a 149 kW (200 HP) TRL 6 demonstrator from UAV Turbines, funded by the US Army Reliable Advanced Small Power Systems (RASPS) program, which has already demonstrated a 0.304 kg/kWh (0.5 lb/HP·hr) turbine at the 37 kW (50 HP) scale. These engines may further improve performance if retrofitted to the *Metaltail* airframe.

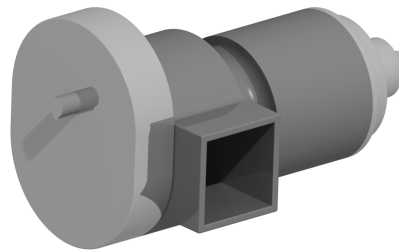


FIGURE 8.2: STV 130 Turboshaft Engine

The STV 130 uses diesel fuel, allowing refueling at any location that stores it including hospitals and other public buildings with diesel generators. The free turbine-powered drive shaft allows the rotor to be stopped with the engines at idle for safe ground operations while the avionics operate on battery power. An automated, engine startup, controller starts the engine completes in 20 seconds from battery power, using an integrated starter motor, reducing emergency response time. With a reported critical altitude of 9,100 m (30,000 ft), the STV 130 allows full power generation above the required performance altitude of 3000m. The time between overhaul (TBO) of 2000 hrs is the same as or higher than certified piston aircraft engines of similar size.

The STV 130 engine was originally designed for general aviation fixed-wing aircraft, and thus requires a modified lubrication system to allow for extended operation at vertical orientations. Additional oil sump scavenge lines are added to the engine at local low points in a vertical orientation to prevent pooling of engine oil. These lines feed back to the engine's standard scavenge pump.

The exhaust ports are connected to a combined exhaust pipe exiting the side of the aircraft, angled away from the aircraft for ground operations safety and to prevent overheating of the wing leading edge. The exhaust outlets maintain the cross section of the engine exhaust ports to prevent increased backpressure in the turbine. Due to the limited frontal area of the exhaust ports and a thrust contribution from the turbine exhaust, exhaust drag does not contribute significantly to the overall fuselage drag area.



Engine cooling oil flows through a radiator mounted inside the bottom of the *Metaltail*'s engine cowling. Air flowing through the radiator feeds the engine intakes, which is supplemented by a 200 W (0.27 HP) fan at engine idle when the rotor is locked for ground operations.

8.2 Transmission Design

In order to combine engine outputs and match RPM between both rotors, a geared transmission with a dual-input, spur gear reduction module and a split bevel coaxial drive module was selected to transmit power to the *Metaltail*'s coaxial rotor shafts.

8.2.1 Configuration Study

Alternate power transmission configurations examined include the following:

- **Pericyclic Variable Transmissions (PVTs)** have up to 50% lower weight and comparable efficiency when compared to epicyclic transmissions [9]. However, the fuel weight saved from the propulsive efficiency gain of variable transmission RPM is outweighed by the requirement for a motor-generator pair or traction-type CVT to backdrive the PVT to enable speed variation. This requirement for a second transmission eliminates specific power and efficiency benefits in Group 3 UAVs. A fixed-ratio implementation of the PVT on a coaxial configuration requires a separate power-splitting module, eliminating the potential weight savings of the PVT's high specific power.
- **Traction-Type Continuously Variable Transmissions (CVTs)** allow for selection of ideal rotor speeds through varying reduction ratios with transmission efficiency up to 97%. CVTs are poorly suited to high torque applications and have lower specific power than fixed-ratio transmissions. Future improvements in materials may enable this type of transmission to operate at the torque required for *Metaltail*, allowing for increased rotor efficiency and reduced fuel burn with a transmission retrofit, but CVTs are not currently a viable option.
- **Planetary Transmissions** provide large speed reduction with potentially higher specific power, efficiency and power density than a standard spur or helical gear reduction gearbox. However, the required speed reduction ratio for the *Metaltail* is lower than the minimum practical speed reduction ratio of 1:2.5 for a planetary drive. Additionally, the combination of two engine outputs necessitates having at least one combining stage prior to the input of the planetary reducing gearbox.
- **Electric Motor-Generator Drives** currently produce up to 5.2 kW/kg (3 HP/lb) and about 93% efficiency per stage [10]. Combining a motor and generator in series reduces this overall specific power by 50% to 2.6kW/kg with an overall efficiency of about 86% before taking into account added weight and losses from the power wiring and cooling. A motor-generator system has relatively low specific power (2.5kW/kg) compared to a fixed-ratio geared transmission (about 8-15 kW/kg) and lower efficiency (about 90% vs. approximately 98-99%). With these limitations in mind, electric transmissions are unsuitable for coaxial configurations at the Group 3 scale.

In view of these considerations, a fixed-ratio combining gearbox was chosen with dual-input reduction module and split bevel coaxial drive module. This configuration has high efficiency



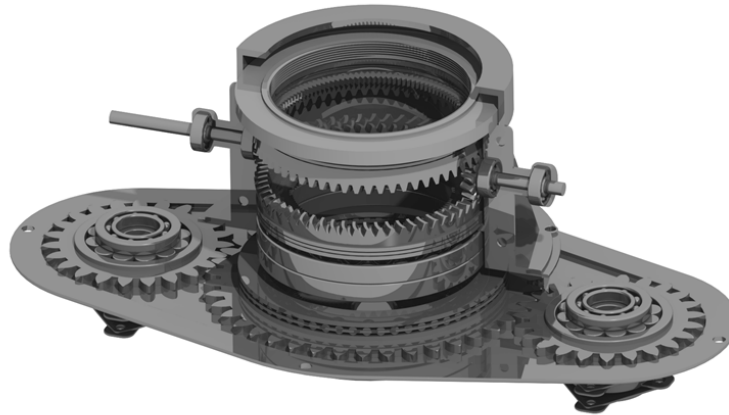


FIGURE 8.3: Gearbox section view

(99%) and high specific power (13 kW/kg) while combining two engine inputs. This configuration is able to power counter-rotating, coaxial output shafts and fit inside the boundaries of the *Metaltail's* streamlined fuselage with its axially-aligned input and output shafts.

8.2.2 Combining Coaxial Transmission

The transmission gearbox (Figure 8.3) includes two stages: dual-input speed reduction stage using involute spur gears and a power splitting stage made up of spiral bevel gears. Each input shaft from the turbine engines has a flexible coupling before entering the gearbox to accommodate axial and angular misalignments. An overrunning sprag clutch is integrated into each spur input pinion inside the gearbox to allow one engine to continue powering the rotor system without backdriving the second engine in the case of a One Engine Inoperative event to prevent parasitic losses and damage to the inoperable engine. Sprag clutches also allow for rotor autorotation.

The input spur pinions are secured on a keyed shaft for torque transmission with retaining rings to restrict axial movement and straddle-mounted radial ball bearings to carry side loads from tooth meshing. The reduction module spur gear is splined to the main drive shaft and supported axially in both directions by roller thrust bearings. The main drive shaft, carrying 100% of the total power, is supported axially by a pair of angular contact bearings to restrict axial movement on the main drive shaft of the split bevel coax drive module.

The main drive shaft is internally splined to transmit power to the upper rotor drive shaft and splined externally to transmit power through the split bevel gears. The lower spiral bevel gear, supported axially by a roller thrust bearing, drives two spiral bevel idler pinions. The idler pinions are mounted in an overhung configuration with an angular contact bearing to carry the side forces and axial separation forces from the spiral gear mesh and a radial ball bearing to carry side forces on the pinion shaft. One pinion idler shaft extends through the gearbox case housing to provide power to the gearbox oil pumps and a contact point for the rotor brake. The second pinion idler shaft extends from the case to provide power to the alternator. Both idlers transmit power to the upper spiral bevel gear, which is supported by a roller thrust bearing and is splined to transmit power to the lower rotor shaft.

This power splitting configuration ensures that the rotors will operate at the same RPM while leaving yaw authority (or roll control in forward flight) available to the rotor controls via



differential collective settings. The upper rotor hub loads are transferred to the lower (outer) rotor shaft via angular contact bearings. The lower rotor shaft transfers the combined thrust through the gearbox to the main engine compartment structure by a load-bearing nut on the shaft that supports a roller thrust bearing interfacing with the top of the gearbox case.

8.2.3 Gear Design and Analysis

All transmission gears were designed to operate with a lifetime of 2000 hrs at maximum RPM and power settings with a reliability of 0.997 (3σ). Each gear is made from AMS 6308 (Pyrowear 53) steel, AGMA 6002 Grade 2, which has a higher tempering temperature than traditional AISI 9310 steel. The gears are carburized to HRC 60 (HV 700) then ground, honed, and superfinished using chemically accelerated vibratory finishing to improve durability and achieve lubrication regimen III ($\Lambda > 1.0$) with the MIL-23699 lubricant through reduced surface roughness. In the event of a loss of lubrication (LOL), the gear superfinish, high material tempering temperature, and large flash temperature margin serve to forestall gearbox failure with the goal of exceeding the FAA, EASA, and CTSB requirements of 30 minutes safe flight time after LOL. The spur gears also have a thin face width that improves convective heat rejection, and a thinned tooth profile with increased dedendum depth provides clearance in case of thermal expansion. These two factors further improve LOL performance for the reduction module. The gearbox is investment cast in four pieces using selectively laser sintered mold patterns and Elektron 21 magnesium alloy for weight reduction (compared to aluminum alloys) and corrosion resistance (compared to magnesium-aluminum alloys).

Reduction Spur Gear Design

The reduction module uses spur gears to reduce axial loading on the gear body. Double helical gears were also considered because of their low axial thrust, but ultimately rejected because of the difficulty of manufacturing a double helix on a small face.

The design and analysis of the reduction module spur gears is based on the ANSI/AGMA 2001-D04 and AGMA 908-B89 standards [11, 12]. Tables 8.3 and 8.4 show the stress analysis results of the engine output spur pinions and main drive shaft spur gear. The large 0.4717 m (18.57 in.) offset between the engine shafts guided the selection of large diameter spur gears.

TABLE 8.2: Reduction Spur Gear Geometry

	Engine Output Pinion	Drive Shaft Gear
Number of Teeth	23	42
Pitch Diameter, in. (mm)	6.571 (166.91)	12.00 (304.8)
Diametral Pitch, teeth/in.	3.500	
Module, mm	7.257	
Pressure Angle, degrees	25.00	
Addendum, in. (mm)	0.286 (7.26)	0.286 (7.26)
Dedendum, in. (mm)	0.386 (9.80)	0.386 (9.80)
Clearance, in. (mm)	0.100 (2.54)	0.100 (2.54)
Face Width, in. (mm)	0.360 (9.14)	0.360 (9.14)
Tooth Thinning, nd	0.024	0.024
Gear Ratio	1.826	



To reduce overall gear weight while meeting these geometric requirements, the gears utilize thick teeth with a thin face width to reduce overall weight by balancing contact stress margins and bending stress margins. The gear ratio of 1.826:1 outputs the desired RPM for rotor performance, while the number of teeth selected for each gear provides a hunting tooth gear set (in which each tooth in the pinion will contact every tooth in the gear before contacting any gear tooth a second time to evenly distribute surface contact wear and reduce surface pitting [13]).

Bending Stress Analysis

Equation 8.1 describes the calculation of the bending stress number and margin for each gear [?] with values enumerated in Table 8.3.

$$s_t = U_l K_t K_d = \frac{\dot{W} P_d K_a K_s K_m}{J K_v} \quad (8.1)$$

Equation 8.2 describes the relation between bending stress number and allowable bending stress number [12].

$$s_t = \frac{s_{at} Y_N}{S_F K_T K_R} \quad (8.2)$$

TABLE 8.3: Bending Stress Analysis Factors and Margins

Attributes	Input Pinion	Drive Shaft Gear
Mesh Power, \dot{W} , HP (kW)	130 (97)	
Diametral Pitch, P_d , teeth/in.	3.500	
Module, mm	7.257	
Face Width, F , in. (mm)	0.330 (8.382)	
RPM, $\omega * \frac{60}{\pi}$	2500	1369
Pitch Diameter, in. (mm)	6.571 (166.91)	12.000 (304.80)
Bending Geometry Factor, J	0.4155	0.4666
Unit Load Factor, U_l , psi (N/mm^2)	9697 (66.86)	
Application Factor, K_a	1.250	
Bending Size Factor, K_s	1.100	
Load Distribution Factor, K_m	1.092	
Dynamic Load Factor, K_v	0.850	
Total Bending Derating Factor, K_d	1.799	
Allowable Stress, s_{at} , psi (N/mm^2)	65,000 (448.2)	
Temperature Factor, K_T	1.00	
Reliability Factor, K_R	1.145	
Bending Stress Cycle Factor, Y_N	0.9579	0.9563
Derated Allowable Stress, psi (N/mm^2)	54,391 (375.02)	54,303 (374.41)
Bending Stress Number, s_t , psi (N/mm^2)	45,812 (315.87)	40,795 (281.27)
Bending Stress Margin	1.1873	1.3333



Contact Stress Analysis

Equation 8.3 describes the calculation of the bending stress number and margin for each gear with values enumerated in Table 8.4 [13].

$$s_c = C_K \sqrt{K C_d} = C_p \sqrt{\frac{1}{I} \frac{m_G}{m_G + 1}} \sqrt{\frac{\dot{W}}{d^2 F \omega} \frac{C_a C_s C_m}{C_v}} \quad (8.3)$$

Equation 8.4 describes the relation between bending stress number and allowable bending stress number [12].

$$s_c = \frac{s_{ac} Z_N}{\sqrt{K_R}} \quad (8.4)$$

TABLE 8.4: Contact Stress Analysis Factors and Margins

Attributes	Input Pinion	Drive Shaft Gear
Mesh Power, \dot{W} , HP (kW)	130 (97)	
Diametral Pitch, P_d , teeth/in.	3.5	
Module, mm	7.257	
Face Width, F , in. (mm)	0.330 (8.382)	
Gear Ratio, m_G	1.826	
RPM, $\omega * \frac{60}{\pi}$	2500	1369
Pitch Diameter, d , in. (mm)	6.571 (166.91)	12.000 (304.80)
Pitting Index, K , psi (N/mm^2)	711.8 (4.908)	
Geometric Pitting Factor, I	0.111	
Material Constant, C_P	2800	
Contact Geometry Factor, C_K	5543	
Application Factor, C_a	1.250	
Contact Size Factor, C_s	1.000	
Load Distribution Factor, C_m	1.092	
Dynamic Load Factor, C_v	0.850	
Total Contact Derating Factor, C_d	1.607	
Allowable Stress, s_{ac} , psi (N/mm^2)	225,000 (1551)	
Reliability Factor, K_R	1.145	
Contact Stress Cycle Factor, Y_N	0.9248	0.9228
Derated Allowable Stress, psi (N/mm^2)	194,480 (1340.9)	194,073 (1338.1)
Contact Stress Number, s_c , psi (N/mm^2)	187,466 (1292.5)	187,465 (1292.5)
Contact Stress Margin	1.0374	1.0352

Split Power Bevel Gear Design

The power split module (Figure 8.4) transmits power from the main rotor drive shaft to the lower rotor while the main drive shaft transfers power directly to the upper rotor drive shaft via internal splines. The matched bevel gears fix both rotors to the same RPM while allowing



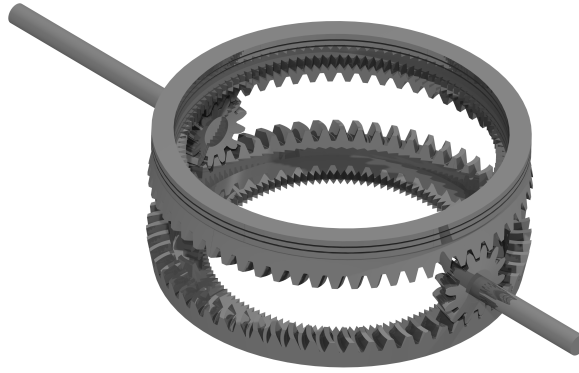


FIGURE 8.4: Power Splitting Spiral Bevel Gear Mesh

varying torque for directional (vertical flight) or roll (forward flight) control. Table 8.5 shows the geometry of the spiral bevel power splitting gears and pinions.

The bevel gear design uses ANSI/AGMA 2005-D03 and ANSI/AGMA 2003-C10 standards (AGMA standards are based upon English unit system and English gear design notation; SI values provided where available). The spiral bevel gear design is primarily geometrically limited, due to the diameter of the rotor drive shafts. An exaggerated base diameter led to small face widths and high stress margins. A 35° spiral angle ensures a higher contact ratio than straight tooth gears despite limited face width. Spiral teeth allow operation at pitch velocities above the 1000 ft/min (5.08 m/s) recommended limit of straight tooth bevel gears while increasing efficiency and reducing noise output. The number of teeth selected for each spiral bevel gear provides hunting ratios to all meshes to evenly distribute surface contact wear [14].

TABLE 8.5: Spiral Bevel Gear Geometry

	Shaft Bevel Gears	Bevel Pinions
Number of Teeth	61	12
Pitch Diameter, in. (mm)	8.652 (219.76)	1.702 (43.23)
Pitch Angle, degrees	78.87	11.13
Face Width, in. (mm)	0.500 (12.7)	
Diametral Pitch, teeth/in.	7.050	
Module, mm	3.603	
Spiral Angle, degrees	35.00	
Pressure Angle, degrees	20.00	
Addendum, in. (mm)	0.142 (3.603)	0.142 (3.603)
Dedendum, in. (mm)	0.177 (4.50)	0.177 (4.50)
Clearance, in. (mm)	0.036 (0.90)	0.036 (0.90)
Tooth Thickness, in. (mm)	0.223 (5.66)	0.223 (5.66)
RPM	1369	6959
Pitch Velocity, ft/min (m/s)	3101	
Gear Ratio	5.083	



8.2.4 Gearbox Cooling and Accessories

Gearbox Cooling

Spur and Spiral Bevel gears typically have mesh efficiencies of about 0.995, resulting in a total gearbox efficiency of 99% and a 1.55 kW (5290 BTU/hr) maximum continuous thermal load on the oil cooler [15]. To cool the gearbox and maintain an maximum oil temperature of 25°C (45°F) above gear body temperature, a dry sump system with an 820 kPa (120 psi) oil injection gear pump draws from a reservoir to spray into the gearbox through injection ports pointed at each gear mesh point. The gearbox collects oil at sumps located at low points for both vertical flight and forward flight orientations. This scavenged oil is filtered and passed by a magnetic chip detector and through a 410 kPa (60 psi) scavenge pump to the dual loop engine and gearbox oil cooling radiator before being returned to the gearbox oil reservoir. Cooling inlet flow is assisted by a radiator-mounted fan in vertical flight.

Gearbox-powered Accessories

Both oil gear pumps are powered from the fore (vertical flight)/lower (forward flight) spiral bevel pinion shaft extended through the gearbox case. The rotor brake grips the aft/upper pinion shaft to reduce potential failures from the failure of a rotor brake attached to the main drive shaft. A 14V, 60A alternator charging the Lithium-ion battery is powered by connection to the end of the same aft/upper pinion shaft.

9 Wing Design

The *Metaltail's* mission profile and performance requirements demand a highly efficient, lightweight vehicle cruising at speeds higher than the maximum speed of most similarly sized general aviation aircraft. The wing design was driven primarily by the high speed cruise requirement and the geometric requirement of a 3m maximum vehicle span in vertical flight. The resulting design uses a highly-loaded, high-aspect ratio sweeping wing to achieve a best-range cruise speed of 311 km/h (167 kts) and a minimum swept span of under 3m. The swept wing also increases pitching moment for transition via aft movement of the wing center of pressure, decreasing transition time and increasing the margin of trimmable center of gravity movement. This chapter details the aerodynamic and structural design of the *Metaltail* wing and the mechanical design of its lightweight sweeping mechanism.

9.1 Wing aerodynamic Design

The *Metaltail* wing aerodynamic design focused on efficient cruise, light weight and low drag. A aspect ratio of 12, high wing loading of 293 kg/m² (60 lb/ft²) and a 17% thick, low-drag subsonic airfoil were combined to reduce both parasitic and induced drag and achieve cruise and maximum speeds above those of most twin-engine general aviation (GA) aircraft. Crucially missing from aircraft requirements is the FAR Part 23.49 requirement for a 113 kph (61 kts) stall speed for safe landings. As a reconfigurable VTOL aircraft, the *Metaltail* takes advantage of a stall limitation defined by vertical-to-forward flight transition rather than wheeled landing to increase the cruise lift coefficient. High wing loading increases stall speed to about 180 km/h (97 kts) and cruise speed to over 310 km/h (167 kts) at 3000 m (9800 ft) altitude.



9.1.1 Planform Design

To reduce aircraft drag and weight, the wing planform, shown in Figure 9.1 was chosen to balance manufacturing complexity and planform efficiency. An aspect ratio of 12 and linear taper ratio of 0.5 over a 4.75 m (15.6 ft) span provide a Prandtl planform efficiency factor of 0.95, closely approximating the load of an elliptical planform without the complexity of fabrication. The slender wingtips also reduce overall span in vertical flight configuration, increasing the ratio of unswept span to swept span to maximize available wing span.

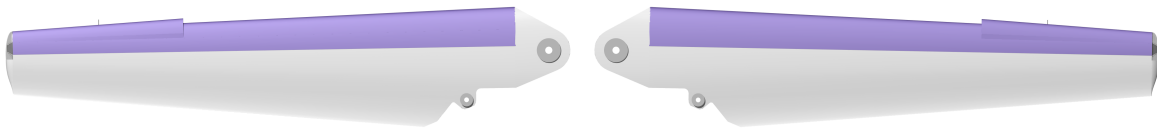


FIGURE 9.1: *Metaltail* wing planform (top view)

A taper ratio of 0.5 also moves the mean aerodynamic chord inboard compared to a square wing, reducing overall bending moment on the root and lowering structural weight.

9.1.2 Airfoil Selection

The *Metaltail* wing uses a NASA/Langley/Whitcomb GA(W)-1 airfoil. This 17% thick airfoil provides more than twice the bending stiffness of typical 12% thickness airfoils used on many GA aircraft like the NACA 2412 and 4412, reducing overall structural weight. Developed for use at Re values on the order of 10^6 and Mach values of approximately 0.3 (the *Metaltail's* cruise flow conditions), the GA(W)-1 provided the best available combination of spar stiffness, low drag ($C_{d_{min}} \approx 0.006$) and maximum lift ($C_{l_{max}} \approx 1.8$) of all airfoils considered. The high $C_{l_{max}}$ allowed for a wing design avoiding the drag and weight penalty of lift augmentation devices like flaps or slats, and the high structural stiffness allowed for the high wing loading crucial to increasing cruise speeds.

Among the airfoils considered for the main wing were:

- the **Wortmann FX 63-137**, a high lift airfoil, suitable for very high cruise C_l values. This airfoil provides high lift to drag (L/D) ratios at ideal conditions, but relatively poor structural stiffness compared to the GA(W)-1. Additionally, cruise C_l values near peak airfoil L/D would require a wing loading too high for the wing structure to bear at the desired cruise speed.
- The **NACA 2412** airfoil, used on most Cessna single-engine GA aircraft. This was ruled out with a lower cruise L/D ratio, higher minimum drag and lower $C_{l_{max}}$ than the Wortmann airfoil.
- the **Clark Y** airfoil, another high lift airfoil, has a wide range of sectional L/D ratios over 100. Ultimately, the Clark Y was also ruled out for a too-high cruise C_l , low structural stiffness, and a low $C_{l_{max}}$ value of about 1.5.



9.2 Wing Structural Design

The structural design of the *Metaltail* wing focused primarily on weight reduction for increased range and payload and increasing structural stiffness to avoid aeroelastic divergence and flutter at high forward speeds. Finite element analyses were performed on the wing spar and wing box to validate load-carrying capacity at load factors of +3.8g/-1.9g suggested by FAR part 23 for aircraft under 2,722 kg (6,000 lbs).

9.2.1 Internal Structure

The wing is built around a box beam spar. The spar is the main structural member of the wing, carrying most of the aerodynamic and inertial forces and moments. This is made with a lay-up of [0/90/0/0/90/0]s T300 graphite/epoxy fiber at the root section and gradually reduced to a lay-up of [0/90/0]s plies at the tip section. The cross section location of the spar reaches from 20% to 60% of the chord. Seven ribs located from 11.7% to 100% of semi-span are mounted to the fore and aft of the spar to prevent wing skin buckling. The fourth and fifth ribs also support the aileron actuation mechanisms. The skin is composed of a lay-up of two [45] carbon fiber plies to provide an airfoil profile surface and additional torsional stiffness. A stainless steel abrasion strip is bonded to the leading edge of the wing to prevent foreign object debris from damaging the composite skin.

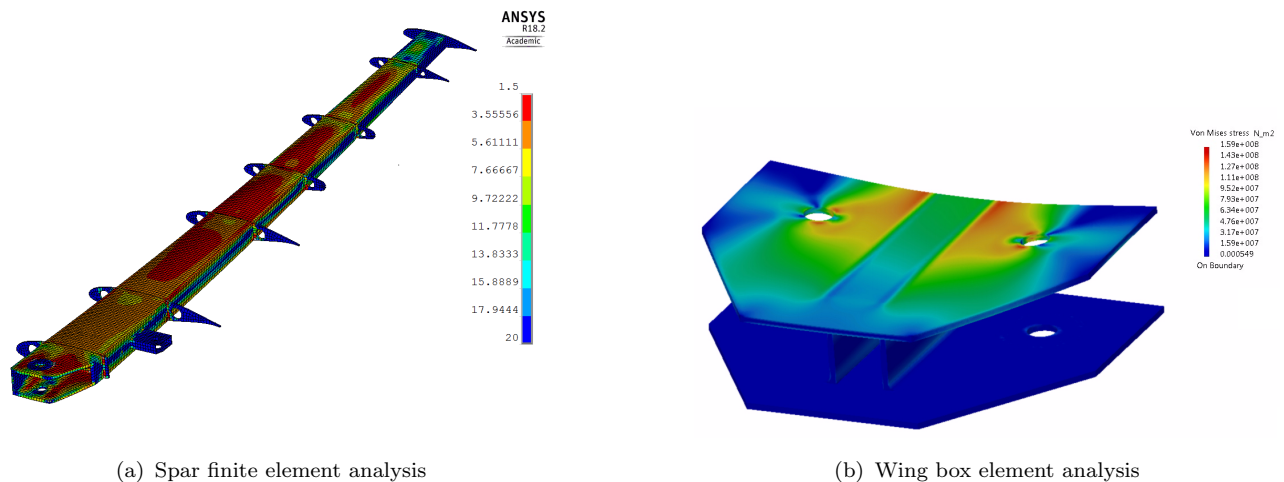


FIGURE 9.2: Finite element analysis of wing structure for *Metaltail*.

The wing root carries lifting loads while allowing it to swing with the motion of the wing sweep actuator. The wing is connected to the wing box via a titanium pin. Together with a pair of bushings on the top and bottom of the root, this mechanism creates a cantilevered boundary condition in bending and torsion. A linkage support beam located at 20% of the semi-span serves as a load path for the swing wing control mechanism. A second pin at the end of the linkage support beam provides rotational freedom for the linkage. The actuation arm of the swing mechanism is connect to the wing through this pin. Between the first and second rib, Rohacell 75 foam reinforces the skin around the linkage support beam where the skin experiences a portion of the actuation load.

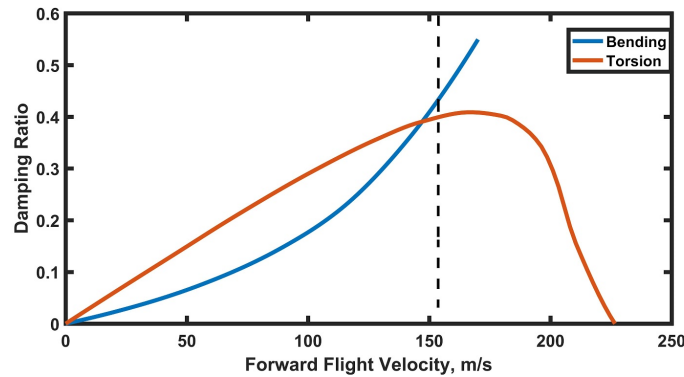


FIGURE 9.3: Wing aerodynamic damping vs. forward flight velocity

9.2.2 Finite Element Analysis

A finite element analysis was conducted on critical structural composite wing components to supplement analytical calculations for the wing lift-carrying structure and the wingbox that transfers load to the fuselage bulkheads, as shown in Figures 9.2. The spar and wing box have a factor of safety of at least 2.25 at all points under the maximum +3.8g loading condition according to the Tsai-Wu failure criteria.

9.2.3 Aeroelastic Analysis

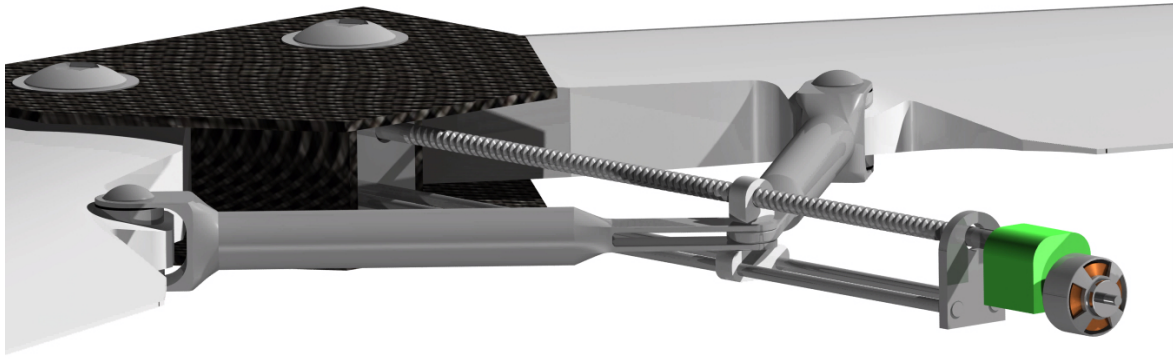
In forward flight, *Metaltail* operates as a fixed wing aircraft propelled by the coaxial prorotor. To safely operate at high speed, it is important to design the wing of *Metaltail* so that flutter is not a problem in high speed before other speed constraints such as maximum power or compression effects on the rotor. An in-house-developed code was used to analyze a cantilever beam model under unsteady aerodynamic loads, and a flap-torsion coupling model was employed to calculate the damping ratio with respect to forward flight velocity. The damping ratios can be seen in Figure 9.3.

9.3 Wing Sweep Mechanism Design

A swing wing is a novel and essential concept of *Metaltail*. Figure 9.4 shows the wing when it is fully extended and fully swept (maximum 65°). The tip distance changes from 4.75 m (15.6 ft) to 2.38 m (7.8 ft) according to the sweep angle; this allows *Metaltail* to have a wing with high aspect ratio while still fitting inside a 18 ft trailer.

A lead screw mechanism was chosen to actuate the swing wing for its simplicity, low actuation force, and high back drive force. Various actuation mechanism were considered, and ultimately a fuselage-mounted symmetrically-linked lead screw actuator was chosen to control sweep angle. The lead screw mechanism was designed to reduce overall weight, resulting in a screw with 600mm travel, weighing less than 1 kg, driven by a brushless DC motor. The electric drive motor is capable of fully sweeping or unsweeping the wing in 8.5 seconds. Redundant shaft encoders measure wing swing position. Contact switches on each end of the lead screw carriage guide rails serve as calibration stops and emergency kill switches for the drive motor.



FIGURE 9.4: *Metaltail* wing sweep mechanism actuator and linkages

The symmetrically mounted wing linkages enforce axial loading along the shaft, with a factor of safety of 5 against buckling. Guide rails on the carriage protect against any asymmetric loading that would bend the lead screw, and the lead screw thread is designed against back-driving. The lead screw is self-locking and no amount of force on the screw from the wing will move the carriage along the screw before the screw fails in buckling. Details of the swing wing actuation mechanism as shown in Figure 9.4.

10 Airframe Analysis and Design

10.1 Airframe Aerodynamics

The shape of the fuselage was designed to accommodate the necessary internal sub-systems and payload, while maintaining a streamlined profile to minimize parasitic drag in cruise and high-speed forward flight conditions.

The first approach was to estimate the parasite drag on the fuselage using equivalent flat plate area f , defined as the ratio of drag D to the dynamics pressure q . The second was performing computational fluid dynamics CFD of *Metaltail* isolated fuselage at max speed conditions. Note that while only a full-fledged CFD solution of the entire vehicle would provide the most accurate estimate of parasitic drag, CFD over the isolated fuselage at maximum speed conditions was performed to ensure flow does not separate and to ensure pressure recovery across the length of the fuselage based on the current design.

10.1.1 Fuselage Drag Area Estimation

For the estimation analysis, flat plate area was estimated by splitting the fuselage into cylindrical sections and summing the parasite drag of the individual sections. The flat plate area was calculated using Eq.10.1.

$$f = C_{Do}S_{ref} = \sum_1^N C_{fi}(FF_i)(IF_i)S_{wet,i} \quad (10.1)$$

Where the variables are defined as:

C_{Do} - zero-lift drag of the fuselage

S_{ref} - reference area, typically the main rotor disk



C_{fi} - skin friction coefficient of the i-th component

FF_i - form factor of the i-th component

IF_i - interference factor accounting for interference drag of the i-th component

$S_{wet,i}$ - wetted area of the i-th component

While C_{Do} and S_{ref} were known and IF_i and $S_{wet,i}$ were estimated, C_{fi} and FF_i had to be calculated. Equation 10.2 was used to calculate the skin friction coefficient, C_{fi} . The form factor, FF_i , was calculated based on Hoerner [ref] using Eq.10.3.

$$C_{fi} = \frac{1.328(1-p)}{\sqrt{Re}} + \frac{0.455p}{\log_{10}(Re)^{2.58}(1+0.144M^2)^{0.65}} \quad (10.2)$$

$$FF_i = 1 + 1.5(d/l)^{1.5} + 7(d/l)^3 \quad (10.3)$$

Where l/d is the fineness ratio of the component body length to the maximum diameter of the component body.

From this approach, the estimated fuselage flat plate area is 0.1013 square meters.

10.1.2 CFD Analysis

An in-house computational fluid dynamics (CFD) code was used to analyze the flow characteristics around the fuselage. The CFD code used was a three-dimensional Reynolds-Averaged Navier-Stokes solver that can operate on both structured and unstructured meshes. The grid around the fuselage was created to ensure that the boundary layer properties were accurately captured along with any separation characteristics. The flow condition was 180 knots (Mach number of 0.29) at 0 degree body angle of attack. As the Reynolds number based on the fuselage length was 23 million, a fully turbulent flow was deemed sufficient. Figure 10.1(a) shows the Mach colored streamlines around Metaltails fuselage, and it was observed that the streamlines adhere to the fuselage surface, indicating attached flow. An earlier iteration of the fuselage design near the prop-spinner featured a rapid increase in cross-sectional area to accommodate the radiator and fuel tanks. However, the position of these internal components were reorganized to prevent flow separation and to minimize the flat-plate area. Figure 10.1(b) shows the pressure distribution along the longitudinal centerline of the fuselage for the upper and lower surface. The key takeaway is the absence of flow separation and the pressure at the tail recovering to near free-stream conditions.



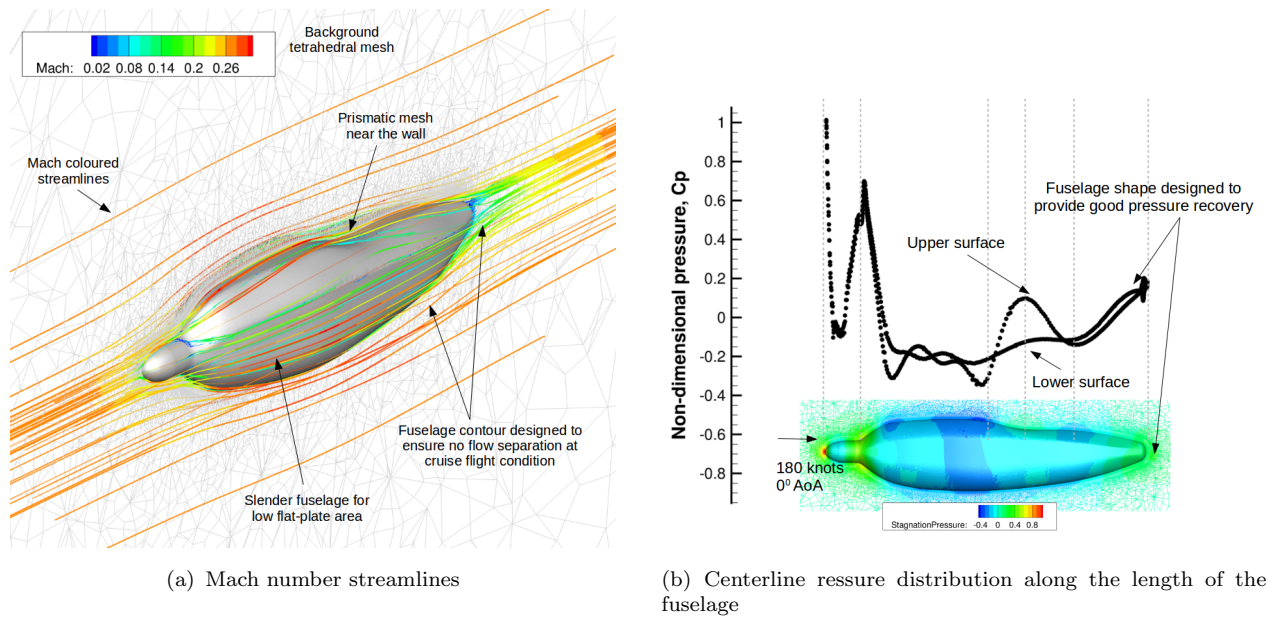


FIGURE 10.1: Results from CFD analysis of isolated fuselage.

10.2 Landing Gear

To handle the loads experienced during landing, the *Metaltail* has four oleo-pneumatic shock absorbers integrated into its structure. Each fin of the X-tail contains a truss structure comprised of three elements, the first being a ring bulkhead to which a hollow leading edge spar is connected. Below is another ring with a horizontal member for supporting a ruddervator, and the truss is closed by an angled tensile member connecting the two rings. This truss structure has been sized to support the vehicles weight on the ground and to support the oleo struts. Telescoping fairings have been placed overtop the oleo-pneumatic struts to minimize the drag they produce, and rounded feet at the end of each strut distributes the landing loads across a larger ground area.

For ground stability, the *Metaltail* landing gear configuration accounts for the center of gravity travel experienced when the vehicle delivers its payload. Each oleo strut is located 1.11 m from the vehicle centerline, rotated 45 degrees around the vehicles longitudinal axis to maximize the tail area. A minimum rollover angle of 30 degrees is satisfied with this setup for C.G. locations up to 2.598 m from the ground. For additional stability, telescoping supports housed within the leading edge of the tail can be used to increase the rollover angle. These telescoping supports can also be used in addition to hard points on the fuselage to lash the *Metaltail* down and counter any high wind conditions that could create undesirable side forces.

10.2.1 Oleo-Pneumatic Strut Sizing

In compliance with Part 27.725 of the FAR, each landing gear oleo-pneumatic strut on *Metaltail* has been sized for a drop velocity of 3.05 m/s and a drop height of 0.33 m . Assuming a gear efficiency of 75% and a gear load factor of 3.5, the total stroke of the strut was found to be 0.181 m [Raymer]. The total length of the strut was thus set at 0.451 m , with an outer diameter of 0.032 m and an inner diameter of 0.024 m . For ease of maintenance, the internal pressure of the oleo-pneumatic strut was chosen to be 12.41 mPa ($1,800\text{ psi}$).



11 Weight Analysis

TABLE 11.1: *Metaltail* Weight Estimates

	Component Description	Weight			x_{cg}		z_{cg}	
		(kg)	(lbs)	(% _{empty})	(m)	(ft)	(m)	(ft)
1	Rotor Group	42.9	94.5	12.3 %	0.00	0.00	3.72	12.20
	Blades	15.4	33.9	4.4 %	0.00	0.00	3.82	12.53
	Hub and Shaft	25.9	57.1	7.4 %	0.00	0.00	3.65	11.97
	Spinner	1.6	3.5	0.5 %	0.00	0.00	3.89	12.76
2	Airframe Group	129.8	286.2	35.6 %	0.00	0.00	2.06	6.75
	Fuselage Structure	94.9	209.3	27.2 %	-0.05	-0.17	2.05	6.73
	Skin	14.8	32.6	4.2 %	0.01	0.03	1.99	6.53
	Paint	5.0	11.0	1.4 %	0.01	0.03	1.99	6.53
	Swing Mechanism	6.4	14.1	1.8 %	0.35	2.04	1.15	6.69
	Wing Box	8.7	19.2	2.5 %	0.32	1.05	2.30	7.55
3	Landing Gear Group	11.4	25.1	3.3 %	0.00	0.00	0.53	1.74
4	Propulsion Group	108.9	240.1	31.2 %	0.00	0.01	2.93	9.61
	Engine	60.0	132.3	17.2 %	0.00	0.00	2.89	9.47
	Battery	1.8	4.0	0.5 %	0.16	0.52	2.55	8.37
	Accessories	47.1	103.8	13.5 %	0.00	0.00	3.00	9.84
5	Fuel System Group	4.0	8.82	1.1 %	-0.10	-0.33	2.28	7.48
6	Wing Group (Hover)	16.7	36.7	4.8 %	0.34	1.12	1.45	4.75
	Wing Group (Forward Flight)	16.7	36.7	4.8 %	0.34	1.12	2.30	7.54
7	Flight Controls Group	14.0	30.8	4.0 %	0.02	0.07	3.55	11.64
	Swashplate	6.9	15.1	2.0 %	0.00	0.00	3.61	11.84
	Actuators	7.1	15.7	2.0 %	0.04	0.13	3.49	11.45
8	Gear Box Group	20.3	44.8	5.8 %	0.00	0.00	3.29	10.79
9	Avionics Group	1.7	3.7	0.5 %	-0.02	-0.07	0.73	2.40
	Empty Weight (Hover)	345.6	761.8	100.0 %	0.02	0.06	2.58	8.47
	Empty Weight (Forward Flight)	345.6	761.8	100.0 %	0.02	0.06	2.62	8.60
	Payload	110.0	242.5		-0.06	-0.20	1.49	4.89
	Fuel	100.0	226.3		-0.10	-0.33	2.28	7.48
	Gross Weight (Hover)	555.6	1224.9	100.0 %	-0.02	-0.06	2.31	7.58
	Gross Weight (Forward Flight)	555.6	1224.9	100.0 %	-0.02	-0.06	2.34	7.66

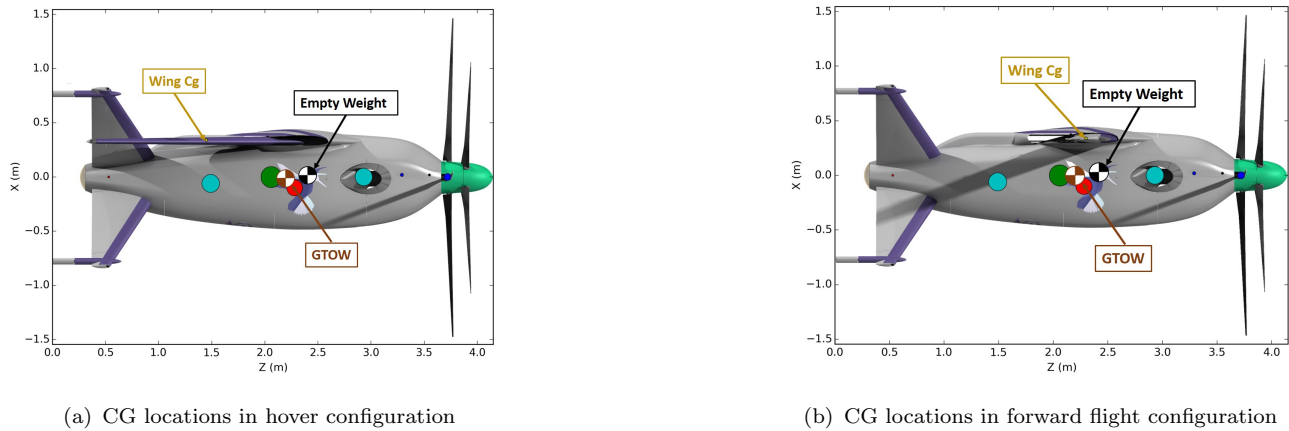
12 Avionics System

12.1 Mission Requirements

The sensor suite and avionics on *Metaltail* is chosen to perform the mission with full autonomy. Fully autonomous flight is defined as flight without a human-in-the-loop. Thus, the selection of avionics components is derived from permutations of the following design spaces.

- **FAA-Necessary Components:** For general aviation aircraft operating within class B airspace (around major airports) and over 10,000ft, a VHF frequency transponder is



FIGURE 11.1: Center of gravity locations for *Metaltail*.

required. The transponder must be Mode C: equipped with altitude encoder and altimeter. Altitude encoding thus necessitates a means of measuring altitude.

An Emergency Locator Transmitter (ELT) is also required by law for all general aviation aircraft since 1977, except for in special cases. Unmanned versions of this vehicle are considered special cases, as the ELT law is useful to allow crashed pilots a method of emergency communication. In the event of a crash while the vehicle is operating autonomously, a similar low-power transmitter is independently powered to provide vehicle location information.

- **Expected Environment Conditions:** The *Metaltail* must be able to navigate quickly and precisely in a number of different environments. These environments are ‘clear day’, ‘nighttime’, ‘occluded by particulates’, and ‘constrained flight path.’ Each situation presents unique challenges. In all cases, the vehicle is susceptible to gust disturbances.

Clear day is the baseline flight condition. This definition is equivalent with daytime VFR. Visibility, cloud ceiling, and cloud clearance minimums are set and vary by location. For navigation in these conditions, gyroscope, accelerometer, pressure/temperature, and satellite navigations sensors are required.

Nighttime is defined by low ambient light. Limitations are thus placed on sensors that rely on ambient lighting, such as optical cameras.

Occlusion presents issues with light-based sensors. In the case of a light-emitting sensor, there may be an interaction (scattering or reflection) between the emitted light and the occluding particulate. In the case of a light-receiving sensor, the occluding particulate may cause the amount of salient information gathered to drop below a minimum amount required for accurate mapping. An example of this with the optical camera is in edge detection, which is useful for optic flow and object detection.

Constrained flight refers to flight in a city or in crowded airspace. A real-time map is necessary in these cases. In a city, *Metaltail* must be able to avoid buildings, people, and other obstacles. In crowded airspace, *Metaltail* must be able to avoid air traffic. In both cases, it is extremely useful for *Metaltail* to accurately project its flight path to any moving people or vehicles in the vicinity.



- **Controllability:** Autonomous controllability and robust disturbance rejection are necessary for all flight modes. While in an urban environment, *Metaltail* will be in hover mode, and must maintain adequate clearance from obstacles, which requires a real-time, 360 degree map of the surroundings. Once it is clear of the city, *Metaltail* transitions to forward flight mode. The transition from hover to forward flight takes place forward or in reverse over a period of 90 seconds, and *Metaltail* maintains controllability throughout the process.

12.1.1 Vehicle Design Budgets

The final vehicle weight, power, volume, and cost budget for all avionics subsystems are shown in Table 12.1.

TABLE 12.1: Avionics Design Specifications

Subsystem	Weight [kg]	Power [W]	Cost [\$]
Sensors	1.26	3.42	139,100
External Communications	1.26	45.2	12,679
Networking	1.8	48.1	900
Processors	0.15	65	15,030
Total estimated	4.82	161.72	167,709

12.2 Sensors

Sensors are categorized by use case. Given the above expected environment and controllability constraints, the minimum amount of sensors are chosen to fulfill these constraints.

- **LIDAR:** Two LIDAR systems are used on *Metaltail*. One LIDAR performs scan in a cylinder along the horizontal plane for precision environment mapping and localization. The second faces downward and is useful for precision landing procedures. The **Velocyne Puck LITE** is a scanning LIDAR with ± 15 degree vertical scanning field-of-view, and 100 m scanning range. The **LeddarTech Vu8** faces downward. It has 100 degree by 3 degree field-of-view and has up to 215 m scanning range. Dust-penetrating (DUSPEN) LIDAR filtering techniques are utilized so that LIDAR can perform mapping in occluded conditions.
- **Optical Camera:** Optical monochrome camera uses an innovative transistor circuit useful for high velocity and low-light flight conditions. Six **Inivation mini-eDVS** event-based cameras are used to generate a robust visible-light view around *Metaltail* with minimal blind spots. Event-based camera updates individual pixels at a time. Update condition is triggered whenever light intensity gradient causes the pixel phototransistor to generate voltage exceeding a threshold. **Inivation mini-eDVS** camera at 128x128 pixel resolution can support up to 50 million pixel updates per-second, compared to 3 million pixel updates per second for a conventional monochrome camera at the same pixel resolution and 200 frames per second. A conventional monochrome camera can typically achieve subpixel resolution up to 1/10 pixel size with appropriate filtering techniques. It is asserted that **Inivation mini-eDVS** can achieve even more accurate subpixel resolution due to pixelwise updating scheme and superior update rate.





FIGURE 12.1: Potential sensor choices categorized by usage

- **RADAR: ImSAR NanoSAR** is a synthetic-aperture radar shrunk down to the size of a shoebox. This RADAR is used on *Metaltail* for altimetry and collision-and-avoidance of both ground and other vehicle traffic (GCAS/TCAS).
- **Satellite and Inertial: SBG Systems Ellipse2-N** satellite and inertial navigation systems are used for high accuracy 6 degree-of-freedom position and orientation estimation. The sensor array has 0.1 degree roll and pitch accuracy and 0.5 degree heading accuracy over full 360 degree angle horizon. The sensor array has 5 cm real-time heave estimation accuracy and 2 m global position accuracy. Global position accuracy is aided with real-time-kinetic (RTK) and wide-area-augmentation-system enhancements to GNSS navigation.
- **Temperature and Pressure: United Sensor Corp. Pitot Static Temperature Probe** is used to determine free flow around *Metaltail*. One sensor is placed at each wing-tip to minimize interference effects from rotor wake.



TABLE 12.2: Sensors Design Specifications

Component	Weight [kg]	Power [W]	Cost [\$]
Velodyne Puck Lite	0.6	0.01	8,000
Leddartech Vu8	0.2	2	1,000
Inivation mini-eDVS camera	0.3	0.9	25,000
ImSAR NanoSAR	0.9	15	100,000
SBG Systems Ellipse2-N	0.5	7	5,000
United Sensor Corp. Pitot Static Temperature Probe	0.01	0.65	100
Total estimated	2.51	18.42	139,100

12.3 External Communications

Four communication regimes are used on *Metaltail*. **NovAtel GPS-701-GGL** integrates with GPS/IMU sensor array to communicate via GPS. **Sagetech MXS** transponder is used to communicate with air-traffic-control and as distance-measuring-equipment for additional vehicle position tracking with nearby air-traffic-control towers. **TP-Link 2.4GHz antenna** is used for WiFi communication when available. WiFi provides a high data-rate for communication, to send and receive a rich data-set in near real-time. **Globalstar Sat-Fi2** satellite network access transceiver is used for reduced-dataset communication with ground stations.

TABLE 12.3: External Communications Design Specifications

Component	Weight [kg]	Power [W]	Cost [USD]
Globalstar Sat-Fi2	0.36	10	10,000 [per year]
TP-Link 2.4GHz antenna	0.1	20	15
NovAtel GPS-701-GGL	0.5	0.2	1,464
Sagetech MXS	0.3	15	1,200
Total estimated	1.26	45.2	12,679

12.4 Networking

Two popular networking architectures are considered for this vehicle: ARINC-664 and MIL-1773. MIL-1773 is an extremely reliable, low-complexity data bus standard that has been in use on small to mid-size aircraft for over 30 years. ARINC-664 is a modern point-to-point, full-duplex alternative that has the benefit of using many inexpensive, off-the-shelf components and can maintain constant data streams from high data-rate components such as optical cameras. ARINC664 is chosen for its proven reliability with high data-rate applications and flexible, full-duplex architecture. Component specifications and a complete graphic of networking with ARINC664 is shown in Table 12.4.



TABLE 12.4: Networking Design Specifications

Component	Weight [kg]	Power [W]	Cost [\$]
Ethernet switches	0.5	3	20
Network interface cards	0.8	45	15,000
Wiring	0.5	0.1	10
Total estimated	1.8	48.1	15,030

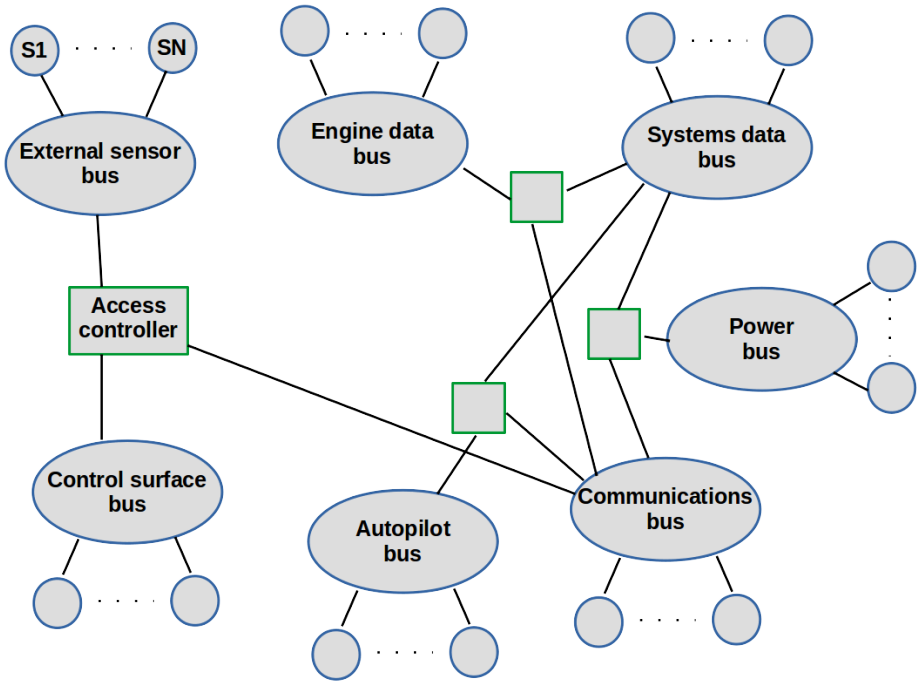


FIGURE 12.2: ARINC664 internal network design

12.5 Processors

Processor choice is derived from thru-put data budget, as well as proven examples of processing architecture for similar applications. A chart of chosen processor components is shown in Table 12.5.

TABLE 12.5: Estimated processor required instructions per second (IPS)

System	Instructions per second	Processor	Instructions per second
Communication	10 ⁶	Snapdragon Flight	10 ⁹
Mapping/Estimation	10 ¹²	NVIDIA Jetson TX2	10 ¹³
Health Monitoring	10 ³	ARM Cortex-M4	10 ⁶



TABLE 12.6: Processors Design Specifications

Component	Weight [kg]	Power [W]	Cost [\$]
NVIDIA Jetson TX2	0.09	20	400
Snapdragon Flight™	0.03	20	400
ARM Cortex-M4	0.025	25	100
Total estimated	0.15	65	900

12.6 Vehicle Systems Integration

This vehicle is constrained for space and must still maintain adequate margins for the following metrics:

- **Power Distribution:** The vehicle must supply appropriate power to all avionics subsystems as needed.
- **Electromagnetic Interference:** Placement of sensitive electromagnetic components is considered to ensure that phantom signals are not captured by sensors, actuators, processors, or communications devices.
- **Temperature control:** Avionics components must be kept within appropriate temperature conditions.

12.7 Assured Autonomy

The autonomy suite utilizes innovative techniques for navigation, state estimation, and object detection based-off reinforcement learning and deep learning. This is possible onboard a dynamic system in real-time due to recent developments in graphics processor minimization and artificial intelligence for embedded systems. Autonomy techniques for vehicle navigation integrate directly with Health and Usage Monitoring System (HUMS) and improves the functionality of both. Detailed below are the avionics requirements for autonomous controllability.

12.8 Controllability Requirements

In the megacity environment, due to the high density of people, buildings, and other fragile systems, is inherently unsafe. Outside of the city, a Class C unmanned vehicle flying in crowded airspace is also inherently unsafe. Thus, the vehicle must be able to reject disturbances robustly and quickly. The vehicle must also be able to avoid and safely interact with obstacles. With respect to avionics, this entails a robust autonomy suite and a low latency controller. Low latency is a design consideration for determining hardware architecture (e.g. networking/data bussing) and software architecture (e.g. algorithm and operating system choice). It is worthwhile to note that the choice of a real-time operating system is preferable for simple networking tasks such as data acquisition and transmission, while a best-effort (e.g. Linux) operating system is preferable for complex tasks such as image manipulation. This is because most robust and reliable modern scientific computing software is developed for best-effort operating systems (e.g., Python, Julia, OpenCV, OpenCL, etc.). The table below shows estimates for maximum allowable latency for different avionics subsystems. Latency is defined as the inverse of update rate.



TABLE 12.7: Maximum allowable latency of avionics subsystems

Subsystem	Max latency [ms]
Position estimation	33
Attitude estimation	4
Actuator response	4
Object detection	33
City path plan refactoring	250
Free-flight path plan refactoring	2000
Health monitoring	250—2000

TABLE 12.8: Maximum allowable latency of avionics subsystems. Inertial estimates based off of typical pose filter rates. Actuator response and object detection bottlenecked by pose estimation. Path refactoring based off of typical values for human response while piloting UAV. Health monitoring bottlenecked by plan refactoring.

TABLE 12.9: Data Rate Budget

Component	Max data rate [kbps]
Optical camera	50,000
LIDAR	35,200
Inertial	14.4
GPS/WAAS/RTK	3.84
Filter states	40.2
System health	64
Total allowed offboard	10,000
Total required	85,322

TABLE 12.10: Data Rate Budget. Estimates shown for 12 GNSS/IMU states, 20 filter states, 20 system health states. Allowed offboard stream rates reflect average upload rates for east coast US cities (2017, SpeedTest).

12.9 Remote Human Pilot

Remote human piloting is commonly determined to be plausible for a fixed-wing UAV in unconstrained forward flight with latency up to 2 seconds. The same is assumed for unconstrained hover flight. These requirements are fulfilled outside of the city environment.

Using WiFi connection in a metropolitan environment and reduced dataset rates for piloting of 5000/500 kilobits uplink/downlink, latency can be estimated at 0.5 seconds. This appears as a small enough time to account for megacity dynamics and human reaction time.

12.10 Object Detection

Object detection is based off of You-Only-Look-Once(YOLO), as shown in Figure 12.3 technique for multi-object, real-time object detection. YOLO makes a single pass through an image to perform object detection at over 45 frames per second (up to 155 fps with Fast YOLO) with a small chance of false prediction. This method is adapted appropriately for event-based cameras.



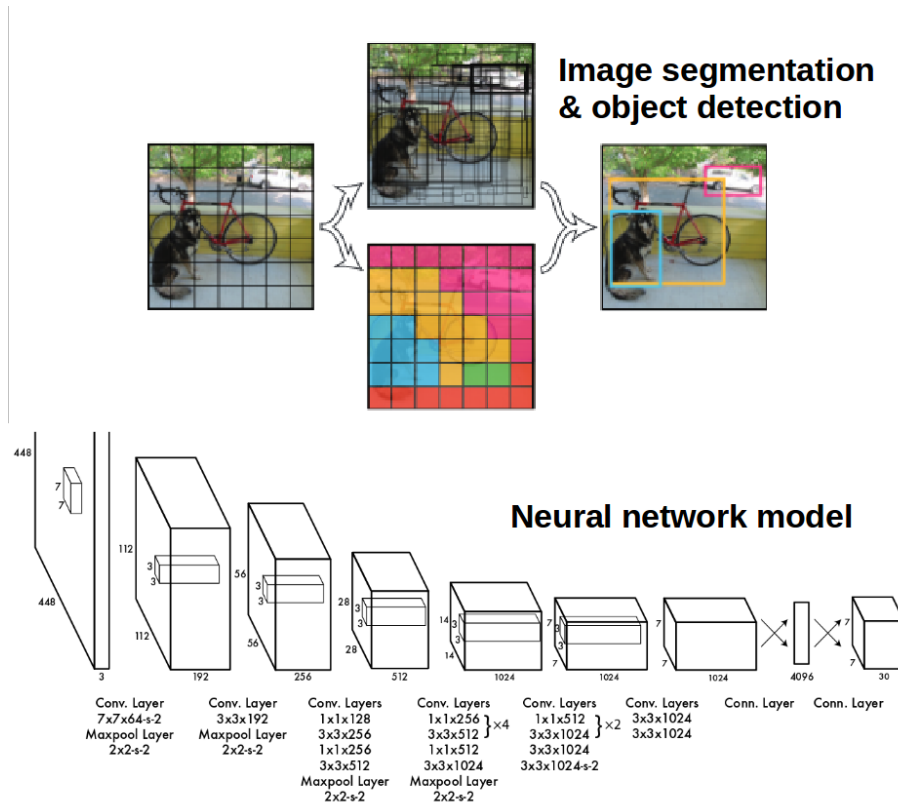


FIGURE 12.3: YOLO Object Detection and Tracking

12.10.1 Communication Modes

Ground-station communication switches between WiFi and satellite link depending upon whether the vehicle is inside or outside of a city. Usage of cell-phone towers is explored but is ultimately not feasible for a fast-moving vehicle flying at altitudes of 3000 meters. Cell towers range in antenna design and power output. It is typically quoted that vehicles moving faster than 120 mph will have problems with network switching and vehicles above 2500 feet will receive signals with high signal-to-noise ratio due to atmospheric effects and low-power antenna lobes.

13 Health and Usage Monitoring System (HUMS)

Health and Usage Monitoring Systems (HUMS) analyzes operation of various *Metaltail* subsystems. This information is vital to ensure that the correct information is present to allow the autonomous, unmanned aircraft to operate in the most fitting condition at all times. HUMS greatly increases vehicle adaptability and preservation in the event of a vehicle subsystem failure. The addition of HUMS is able to decouple failure modes of *Metaltail* to a high degree.

Metaltail HUMS is capable in most instances of performing monitoring, analysis, and system mode adaptation onboard. Hardware failures and in certain cases software failures must be maintained with the aid of external engineers. This is done through the state machine model with prescribed characteristic states and state determination based off of the belief Partially Observable Markov Decision Process (POMDP) model for stochastic systems. POMDP here



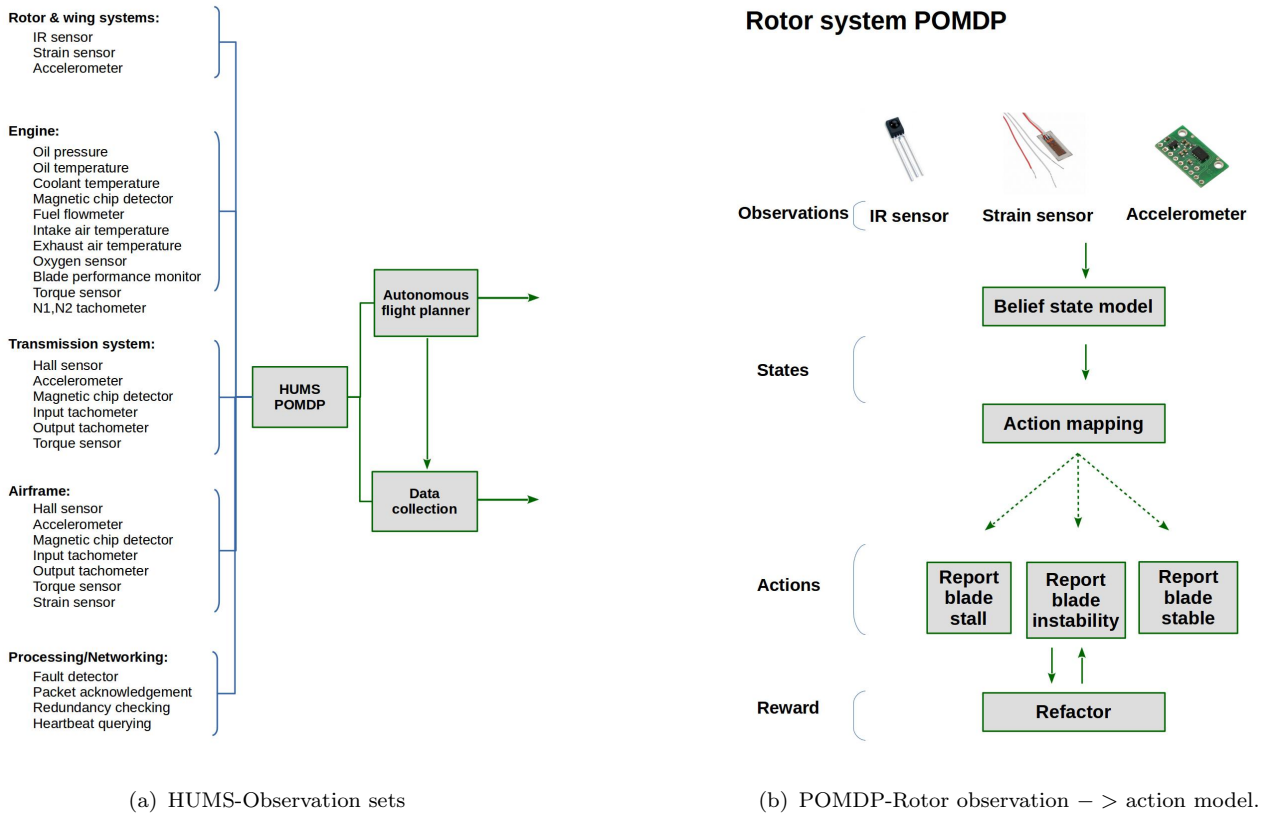


FIGURE 13.1: HUMS system architecture

is a 9-tuple deep reinforcement learning system $(S, O, B, A, T, \tau, r, \gamma, V)$ used to determine system action for a given belief state.

- **S** Set of all states.
- **O** Observations, i.e. sensor measurements.
- **B** Set of belief-based states. Derived from sensor measurements and probability model from observations, previous actions, and previous states.
- **A** Set of finite actions.
- **T** Set of conditional transition probabilities between states.
- τ Belief state transition function. Determines action from state.
- **r** Reward function on the belief states.
- γ Discount factor for future action projection.
- **V** Value of action in a given state transition function τ . Value updates through reinforcing good actions and punishing bad actions. Value is shown to eventually converge to Bellman optimality equation.



Deep Q-Learning is a version of POMDP reinforcement learning. Q-Learning adds in the quality update as a way to rank potential actions in the POMDP set. Deep learning here is a global classification system for creating an empirically-based nonlinear mapping from state input to action quality. Deep Q-Learning has been shown to produce superior results when compared to other empirical POMDP methods and even some human systems.

As an example, a diagram of the POMDP for the rotor subsystem is shown[?]. Not shown are the POMDP for engine, transmission, airframe, processing/networking, and overall system management. The Belief POMDP reinforcement learning algorithm handles in-flight vehicle maintenance in a context-sensitive way. For a pre-defined system priority function, the Belief POMDP algorithm will converge to the optimal mapping between observation and action to fulfil that function. For example the rotor subsystem may prioritize rotor stability by rewarding mappings that result in fast, tightly bound rotor convergence to prescribed control angle for a given control angle input.

Deep Q-Learning here is aided by ‘Rainbow’ techniques[?] in order to significantly speed up convergence to optimal decision. For example, uncommon scenarios such as failure modes are captured by the Belief POMDP by the ‘experience replay’ technique: continually train the Deep Q-Learning network on a small subset of example scenarios. This reduces gradient variance, which is extremely important for practical usage of a stochastic gradient descent algorithm that relies on samples with small gradient. The extensible structure of Deep Q-Learning allows HUMS to be directly integrated with (read: coupled with) all vehicle subsystems so that a more globally optimal vehicle decision is reached with respect to a given reward metric. At any given time, a Belief POMDP may be compared to a different chosen method for in-flight vehicle operation by running a Monte-Carlo simulation and comparing the action taken for a given observation. If necessary, the system may then be retrained or reverted in order to attain a particular shape for the mapping function.

14 Flight Dynamics and Controls

In addition to the normal controllability metrics of stabilization and maneuverability, *Metaltail* fulfils the requirements of transition between hover and forward flight in a tumble free and fully assured autonomous mode. A tumble-free maneuver is defined as a maneuver that is able to reach a trim condition at any arbitrary point along the path between two trim conditions. Full autonomy means that *Metaltail* is robust to large disturbances, and unexpected vehicle configuration changes. This has inspired a novel control scheme that is a combination of typical gain-scheduling methods and deep reinforcement learning. The fusion of these two methods provides the dependability of a linear system controller with the adaptability of a real-time learning system.

14.1 Flight Dynamics Model

A nonlinear model of *Metaltail’s* dynamics was developed, for use in control, stability, and performance analysis. The model takes into account all forces and controls acting on the vehicle, which are shown in Figure 14.1. The model also includes inertial forces, for use in trim calculations where a path with nonzero acceleration is specified.

Metaltail has several methods of control, all of which are included in the dynamics model. Both rotors have full cyclic and collective inputs. The vehicle also has ailerons, and control surfaces on



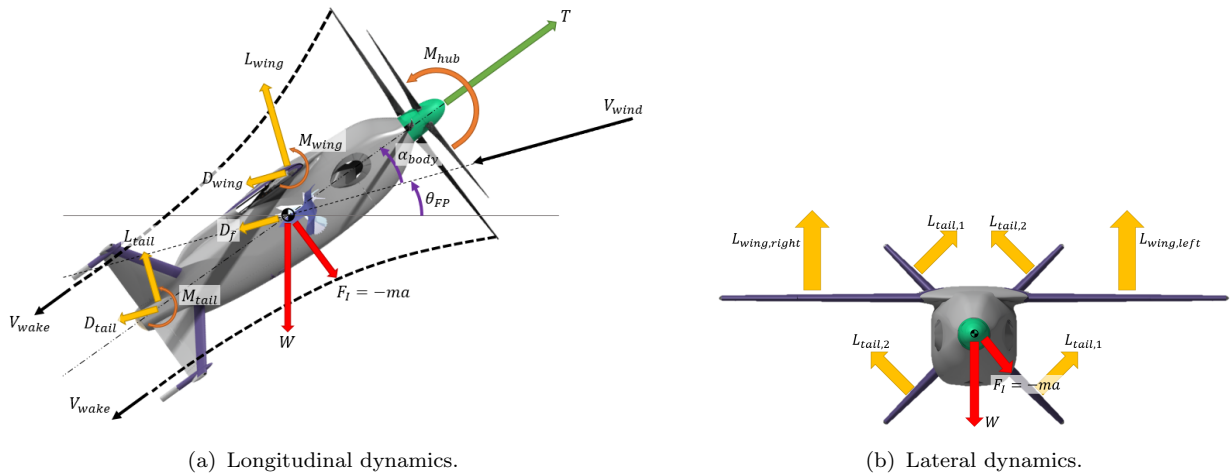


FIGURE 14.1: *Metaltail* dynamics model.

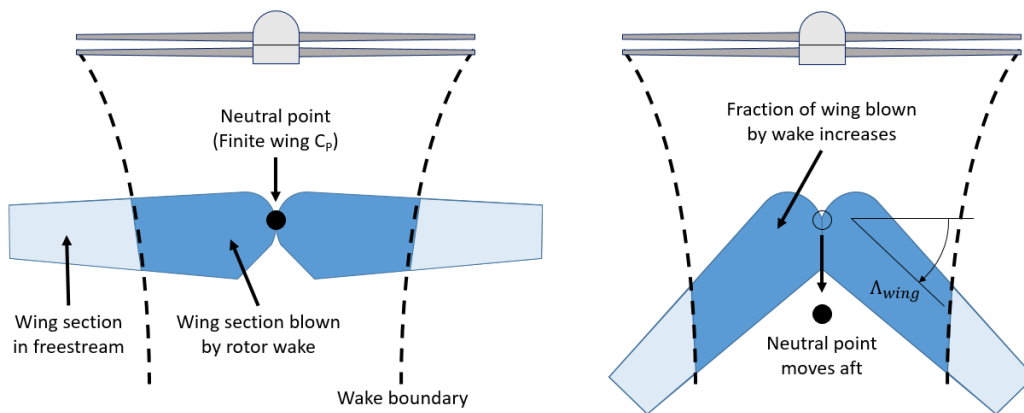


FIGURE 14.2: Aerodynamic effects of sweeping the wing.

each empennage fin. The control surfaces of the fins on opposite sides of the fuselage are linked, but by combining their deflections, conventional yaw and pitch commands can be executed. Because the empennage largely exists within the wake of the rotor (Fig. 14.1(a)), these controls retain authority even in hover.

14.1.1 Effect of Wing Sweep

A key feature of *Metaltail* is its ability to sweep (swing) its wing back during hover, and extend it during cruise. This allows *Metaltail* to be designed with an efficient wing planform, while fitting within the required dimensions in hover. Similarly to the empennage, part of the wing is always in the downwash of the rotor (Fig. 14.2), so the wing will generate some aerodynamic forces even in hover. However, because the ailerons are mounted at the tips of the wings, these may have reduced or have no authority in some phases of flight. Thus, roll control at and near hover must be provided by differential torque of the coaxial rotors.

The ability to swing the wing presents more options for control of the vehicle. The largest effect to the dynamics of the vehicle is the aft movement of the neutral point of the wing when the wing is swept back. With the wing fully extended ($\Delta_{wing} = 0$), the neutral point is ahead of *Metaltail's* center of gravity, so the lift on the wing will exert a nose-up moment on the vehicle.



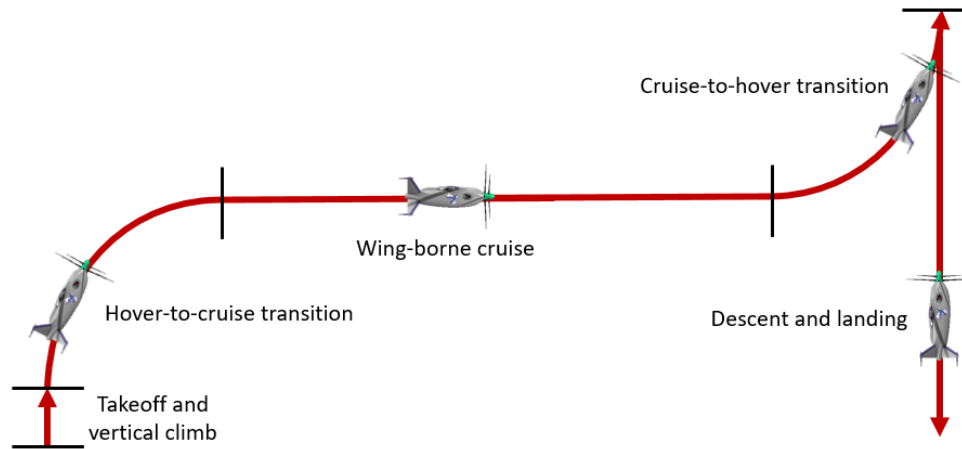


FIGURE 14.3: Phases of flight during one flight cycle.

However, as the wing is swept back, the neutral point translates aft and can move behind the CG for sufficiently large sweep angles, causing the pitching moment due to lift to be nose-down. This variation of the moment due to lift can be used to trim the vehicle over a wide range of CG location and acceleration states, reducing the control inputs necessary to maintain level flight.

Although the movement of the neutral point is the primary effect of sweeping the wing on the stability of the vehicle, there are two other lower order but significant effects. First, as the wing swings back, the vehicle CG also translates aft. This CG translation is small compared to the movement of the neutral point. Second, sweeping the wing back increases the area of the wing which is affected by the rotor wake. However, the effective lift curve slope of the wing decreases slightly due to the wing sweep. The net effect on the lift depends on the specific operating conditions. The effect of the CG translation and the aerodynamic effects of the wing sweep are both included in the dynamics model.

14.2 Transitional Maneuvers

During each flight cycle, *Metaltail* begins by taking off vertically, supported by its rotor, transitions to horizontal wing-borne flight for cruise, then transitions back to rotor-borne flight for descent and landing. These transition maneuvers are all performed under fully trimable conditions (i.e. without tumbling). Several different maneuvers are possible, depending on mission requirements, as shown in Sections 14.2.4 and 14.2.5.

14.2.1 Transition Control Formulation

A simplified model using only *Metaltail's* longitudinal dynamics was used to study the transition between horizontal and vertical flight. The pitch angle of the vehicle, which changes between a vertical and horizontal orientation is an index of the state of transition. In this formulation, it is assumed that the control system is able to counteract any disturbances, including in the lateral direction, and is able to compensate for sideslip. Although decoupling the longitudinal dynamics is not in general a robust model for a helicopter, it is acceptable for a fixed-wing vehicle. It will be shown that *Metaltail* spends relatively less time during transition operating as a pure helicopter; thus, decoupling the longitudinal dynamics is sensible to calculate the approximate control inputs during transition.



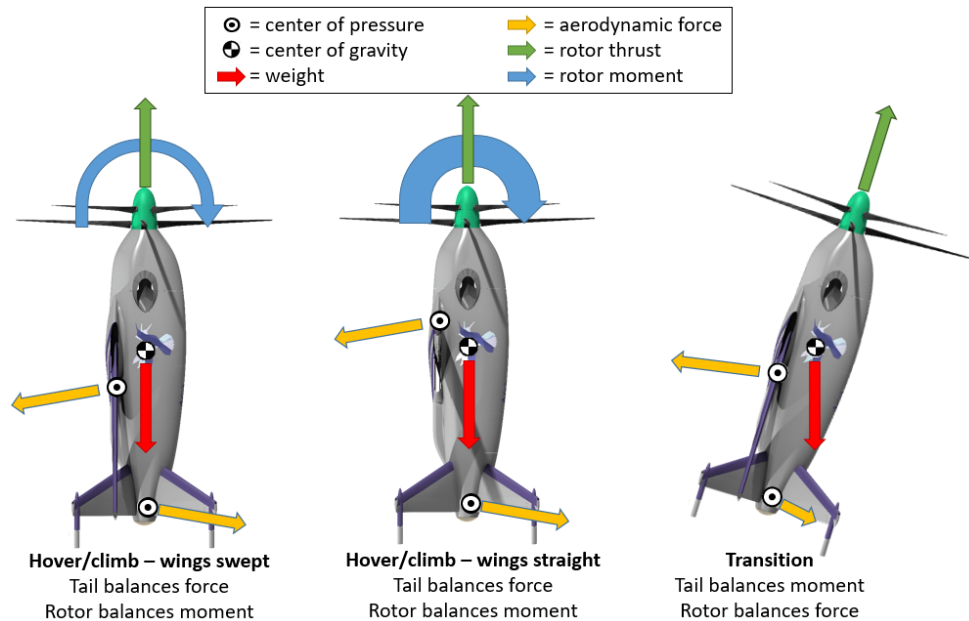


FIGURE 14.4: Control of the vehicle in hover, climb, and transition.

To calculate the required control inputs and behavior of *Metaltail* during the maneuver, a flight path must be specified, which must include the linear accelerations of the vehicle and the wing sweep schedule. Then at each state of the flight path, three equations are solved iteratively: the two force equations about the ground (inertial) X and Z axes, and the moment equation about the body center of mass. The problem is solved at a given time T without requiring a time-marching solution by the inclusion of an inertial force $F_I = -ma$ acting upon the vehicle. This formulation assumes that the blade and aerodynamic control surface responses are instantaneous. It will be shown that the required control inputs are “slow,” so this assumption is reasonable. The angle of attack and control inputs are adjusted until the vehicle is balanced, forming an accelerated-trim condition at each step.

14.2.2 Takeoff and Hover Control

When the *Metaltail* takes off and lands, it must be vertical (perpendicular to the ground) to prevent tipping, or causing excessive stress on its landing gear. It is also desirable to remain vertical during climb, for proper sensor orientation and to keep a small operational footprint around tall buildings, in urban congestion.

In a vertical orientation, in hover or climb, the vehicle weight, rotor thrust, and drag (due to downwash) all act along its longitudinal axis. Since the direction of the thrust and weight cannot be significantly adjusted without tilting the vehicle, the aerodynamic side-forces, i.e., the lift on the wing and the tail (again due to downwash), which act along the vehicle’s vertical axis, must be equal and opposite. *Metaltail* has sufficient elevator authority to be able to cancel the wing lift using the lift generated by its tail. However, because the tail has a longer moment arm from the CG than the wing, there will be a net nose-up moment created by the aerodynamic forces, which must be reacted by the rotor (Fig. 14.4, left and center). As stated above, sweeping the wing back creates a nose-down moment, which reduces the moment which the rotor is required to support. Thus it is beneficial to keep the wing swept aft.

Requiring that the rotor provide a net moment implies that the force on the blades of the rotor



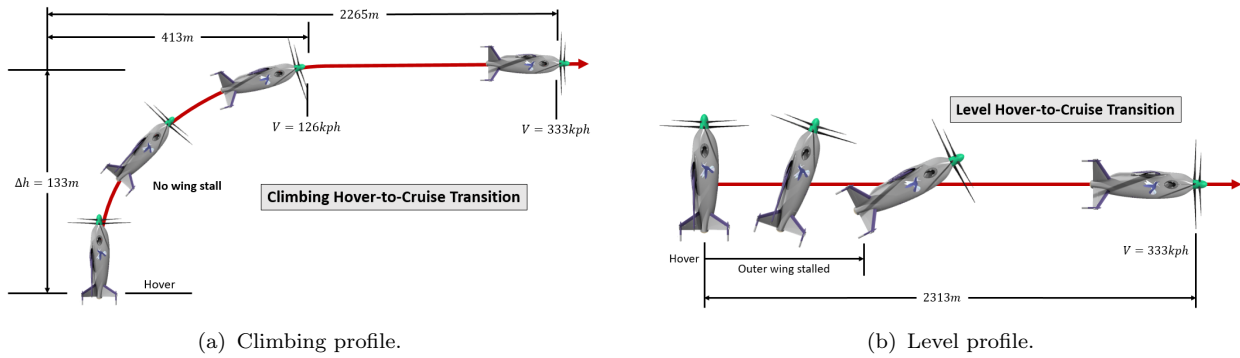


FIGURE 14.5: Hover-to-cruise transition profiles.

will not be equal at all points on the disk. This unequal loading is not desirable when the vehicle is maneuvering, as the most heavily loaded blades will stall at a lower total thrust. The wing lift (which is dominated by the effect of the rotor downwash in hover) cannot be changed significantly. However, by tilting the vehicle, the lift begins to oppose the weight, while a component of the rotor thrust acts opposite the side-force created by the wing. Since a component of the thrust balances part of the side-force from the wing, the lift on the tail may be reduced, thus reducing the moment, which must be reacted by the rotor. By selecting the proper elevator deflection, the vehicle assumes an orientation with zero net moment, without the need for the rotor to provide a reaction moment.

Thus, there are two control modes of particular interest: one in which the body angle is vertical, and another in which the rotor provides zero moment. The former strategy is useful for climbing and hovering near the ground. The latter strategy, also useful for hover, but in particular useful to achieve at the initiation of any maneuver.

14.2.3 Transition Control Strategy

Metaltail's transition maneuvers are designed to be executed as quickly as possible, without hitting the vehicle's stall and structural limits. Because *Metaltail* has multiple control methods, it is necessary to decide which metrics will be most important, and adopt the control strategy accordingly.

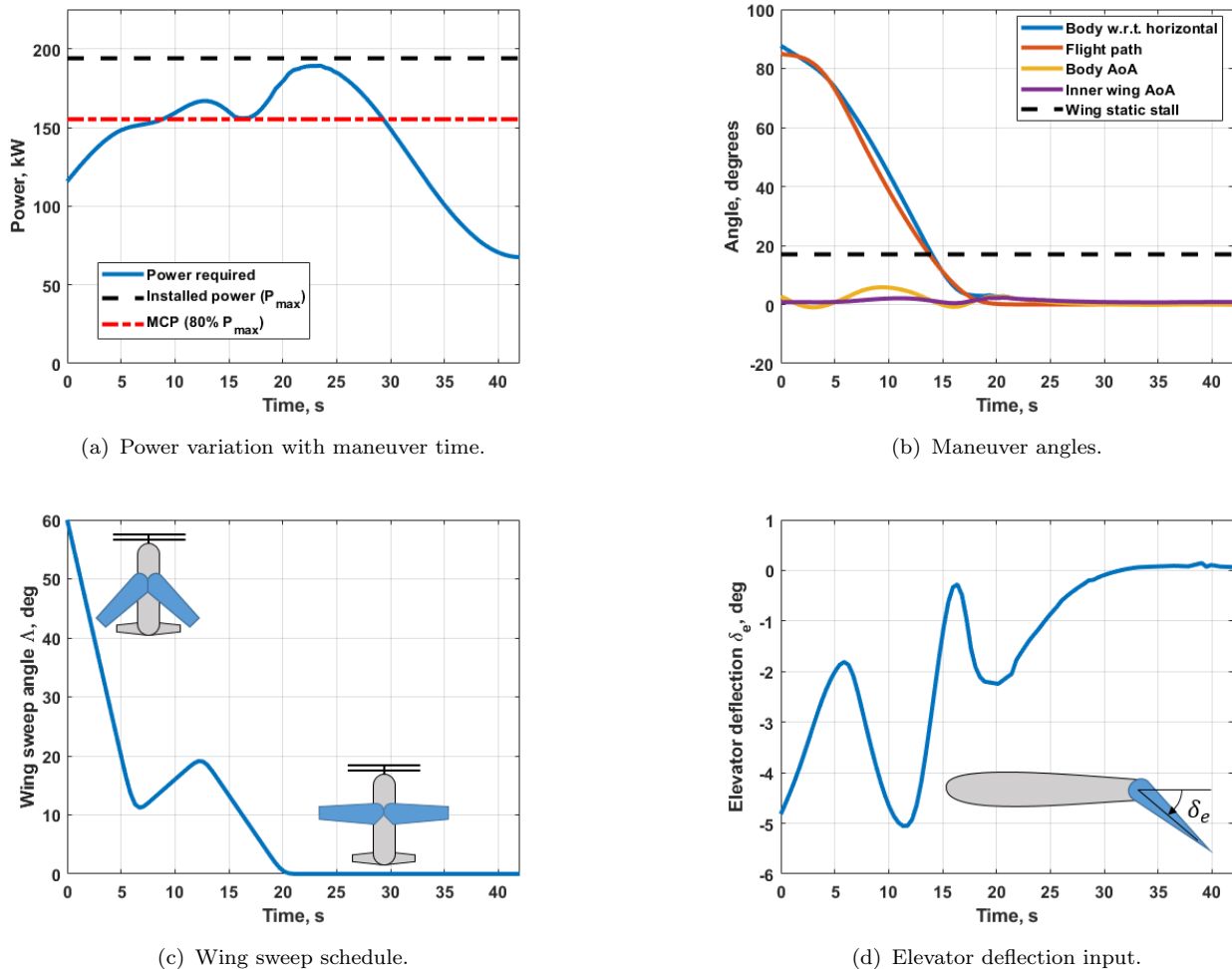
The primary goal which was chosen is to perform the transition with the minimum required control input, which gives the greatest margin for disturbance rejection. In particular, the rotor cyclics are not used unless the elevator reaches its travel limit (5 to -30 deg). By examining the elevator deflection over the time of the maneuver, it was possible to determine whether the elevator was exerting a nose-down (positive δ_e) or nose-up (positive δ_e) moment on the vehicle.

In all maneuvers, the wing must be fully swept back in hover, and fully extended in cruise. The elevator control deflection was used as an index of the net moment being exerted on the vehicle and the wing sweep schedule was designed to minimize this moment (and thus the elevator deflection) to the extent possible.

14.2.4 Hover-to-Cruise Transition

The outbound transition covers the acceleration from hover to cruise speed. Many profiles are possible, but a profile with an initial climb segment (Fig. 14.5(a)) and a profile which remains entirely level (Fig. 14.5(b)) are of particular interest. The goal of the climbing profile is to keep



FIGURE 14.6: Description of the climbing hover-to-cruise transition maneuver for $T = 42s$.

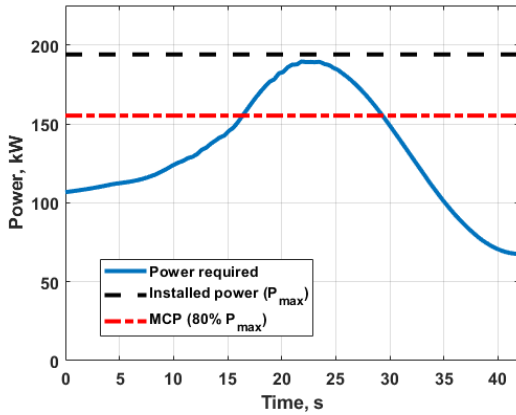
the angle of attack of the vehicle low, maximizing the aerodynamic efficiency of the vehicle. In addition, the curvature of the profile means that the wing and rotor are more lightly loaded during part of the initial acceleration, reducing the power required. However, a level profile may be preferred if the vehicle is operating in a constrained airspace environment. When operating in cities, it is necessary to make an initial climb above the height of the surrounding buildings, but it may also be desired to stay beneath controlled airspace near that city's airport, unhindered by the high volumes of commercial airlines.

14.2.4.1 Climbing Hover-to-Cruise Transition

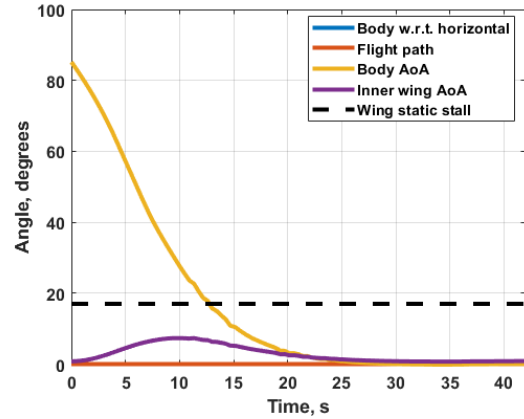
The elevator control deflection, angles of the body and the flight path, and power required for the climbing maneuver are shown in Figure 14.6. A maneuver taking 42 seconds from hover to cruise was chosen as the power approaches, but does not exceed the maximum installed power (Fig. 14.6(a)). Notice that there is a reduction in power at around 50 m/s, due to the curvature of the flight path (Fig. 14.5(a)).

At the start of the maneuver, the vehicle has a slightly off-vertical orientation (because of wing lift from prop wash), so the initial direction of the flight path was chosen to be close to the body angle. This allows the vehicle to operate in a low angle of attack regime throughout the

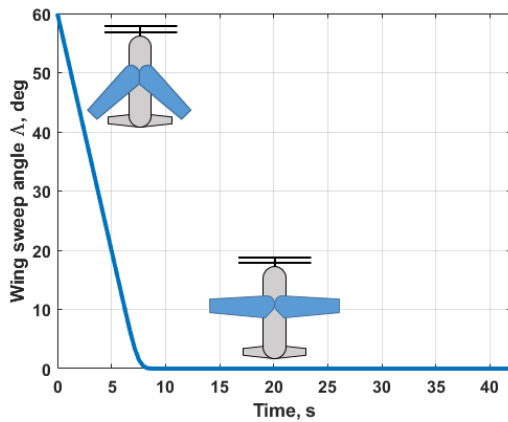




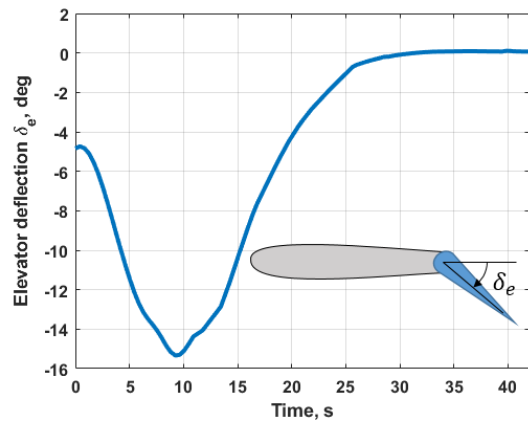
(a) Power variation with maneuver time.



(b) Maneuver angles.



(c) Wing sweep schedule.



(d) Elevator deflection input.

FIGURE 14.7: Description of the level hover-to-cruise transition maneuver for $T = 42s$.

transition (Fig. 14.6(b)). Because the inboard sections of the wing are blown by the rotor, they see a lower angle of attack than the vehicle with respect to the freestream. Although it takes 40 seconds for the vehicle to transition from hover to cruise, the vehicle flight path is horizontal in less than 20 seconds. Thereafter, the vehicle accelerates in wing-borne flight.

The wing sweep schedule for the climbing maneuver is shown in Figure 14.6(c), and the elevator control deflection is shown in Figure 14.6(d). As discussed above, the wing sweep schedule was chosen to minimize the required elevator control input. Throughout most of the maneuver the elevator is required to provide a nose-up moment, but as the curvature of the flight path changes, the elevator would be required to apply a nose-down control. To counteract this, the wing is swept slightly aft, before returning to the cruise position. The rotor cyclic control is essentially zero during the maneuver; only collective is varied to control thrust. The total elevator deflection does not exceed -5 degrees, so there is considerable control margin available for disturbance rejection. Observe also that in cruise, the tail is sized so that there is no required elevator deflection.



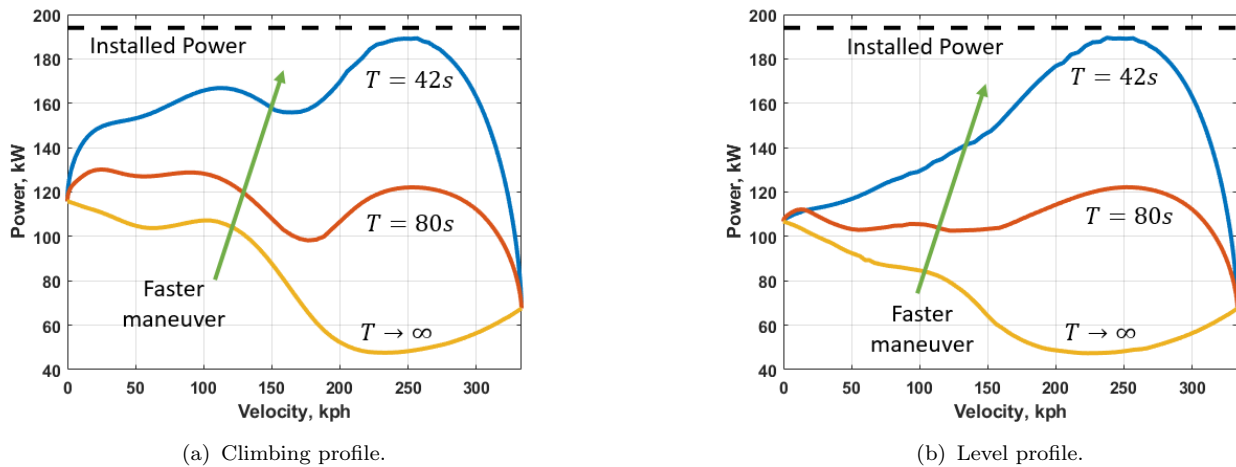


FIGURE 14.8: Power variation with total maneuver time for different hover-to-cruise transition profiles.

14.2.4.2 Level Hover-to-Cruise Transition

Similar plots are shown in Figure 14.7 for the horizontal maneuver. Since there is no curvature to the path, the wing and the rotor must carry the full weight of the vehicle throughout the maneuver, so there is no decrease in the power with increasing speed. However, a 40 second maneuver from hover to cruise remains achievable (Fig. 14.7(a)).

In the horizontal maneuver, the body angle with respect to the freestream is much greater than that in the climbing maneuver. However, because the wing is blown by the rotor, its local angle of attack remains low enough to avoid stall on the inboard sections (Fig. 14.7(b)). Again, it takes less than 20 seconds for the wing to support the bulk of the vehicle’s weight, and the remaining time is spent accelerating to cruise velocity.

Unlike in the climbing case, a significant nose-up control moment is required to keep the vehicle in the proper orientation for the horizontal maneuver (Fig. 14.7(d)). Since sweeping the wing back decreases the nose-up moment in the vehicle, the wing is simply moved from its swept back position in hover to the fully forward position, and kept locked throughout the maneuver (Fig. 14.7(c)).

14.2.4.3 Effect of Hover-to-Cruise Transition Time

When accelerating from hover to cruise in a finite time, a greater power is required than the power required to trim at a constant velocity. The maximum rate of acceleration is thus set by the installed power of the vehicle. Note that because the maneuver takes place in a sufficiently short time, it is the maximum power and not maximum continuous power which is the limit of concern.

The variation of power with maneuver speed is shown in Figure 14.8(a) for the climbing maneuver and Figure 14.8(b) for the level maneuver. In each figure, the power is also shown for a “slow” maneuver ($T \rightarrow \infty$). In the climbing maneuver, the power is higher at low speeds than for the level maneuver, due to the power required to climb. However, this power decreases between 150 and 200 kph, as the curvature changes. Above 200 kph, where both flight paths are level, the power is similar.



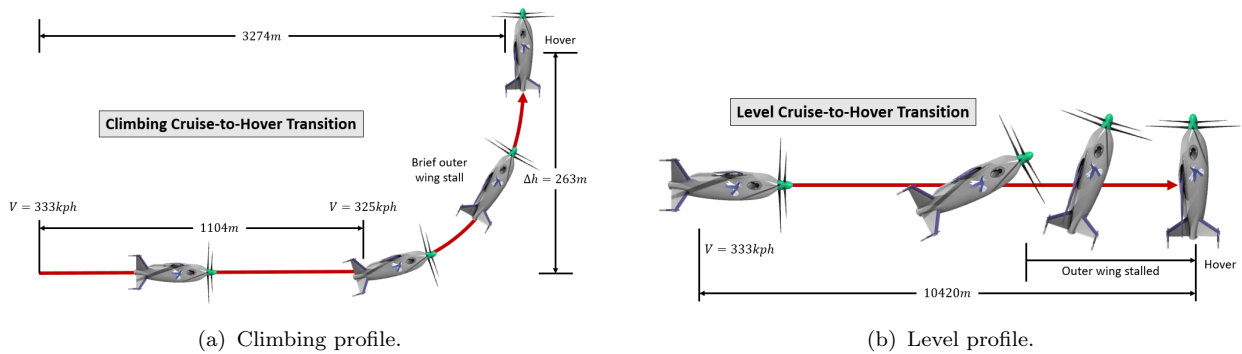


FIGURE 14.9: Inbound transition profiles.

14.2.5 Cruise-to-Hover Transition

The inbound transition covers the deceleration from cruise speed down to hovering flight. After the inbound transition, the vehicle descends and lands vertically. Again, a climbing profile and a profile with a level flight path are considered. In both cases, the limiting factor for the maneuver time was ensuring that the rotor thrust remained positive at all points.

14.2.5.1 Climbing Cruise-to-Hover Transition

The properties of the inbound climbing transition maneuver are shown in Figure 14.10. Climbing allows the use of the vehicle's own weight to slow it down, so the maneuver may be completed in 50 seconds, while avoiding reverse rotor inflow (Fig. 14.10(a)). As the vehicle enters the climb, its body angle of attack initially must increase, increasing its lift, then decreases as the vehicle slows to the end of the maneuver. Again, the wing angle of attack remains low on the inboard section due to propwash (Fig. 14.6(b)).

Because the maneuver requires a net nose-up moment on the vehicle (negative elevator), there is no advantage to sweeping the wing back. The wing is swept only at the end of the maneuver, so that the vehicle assumes its hover configuration (Fig. 14.10(c)). The elevator deflections required are large, so any disturbance rejection that might be needed during the maneuver must be performed using the rotor cyclic control (Fig. 14.10(d)).

14.2.5.2 Level Cruise-to-Hover Transition

The properties of the inbound level flight transition maneuver are shown in Figure 14.11. Unlike in the climbing case, the deceleration in level flight is strictly due to the drag acting on the vehicle, so the maneuver takes 150 seconds to perform, if the rotor inflow must remain positive (Fig. 14.11(a)). Again, the angle of attack increases as the vehicle decelerates, so that the wing produces sufficient lift to balance its weight. The wing inboard angle of attack initially increases as the vehicle pitches, then decreases as the vehicle slows, meaning that the angle of attack is most strongly influenced by the downwash (Fig. 14.11(b)).

Like the climbing inbound transition, a significant nose-up moment is required, so the wing is left in the unswept (forwards) position until the end of the maneuver (Fig. 14.11(c)). The elevator provides additional nose-up moment, but the control saturates for some time during the maneuver (Fig. 14.11(d)). When the elevator control is saturated, additional pitch moment is provided by using a small amount of rotor cyclic control.



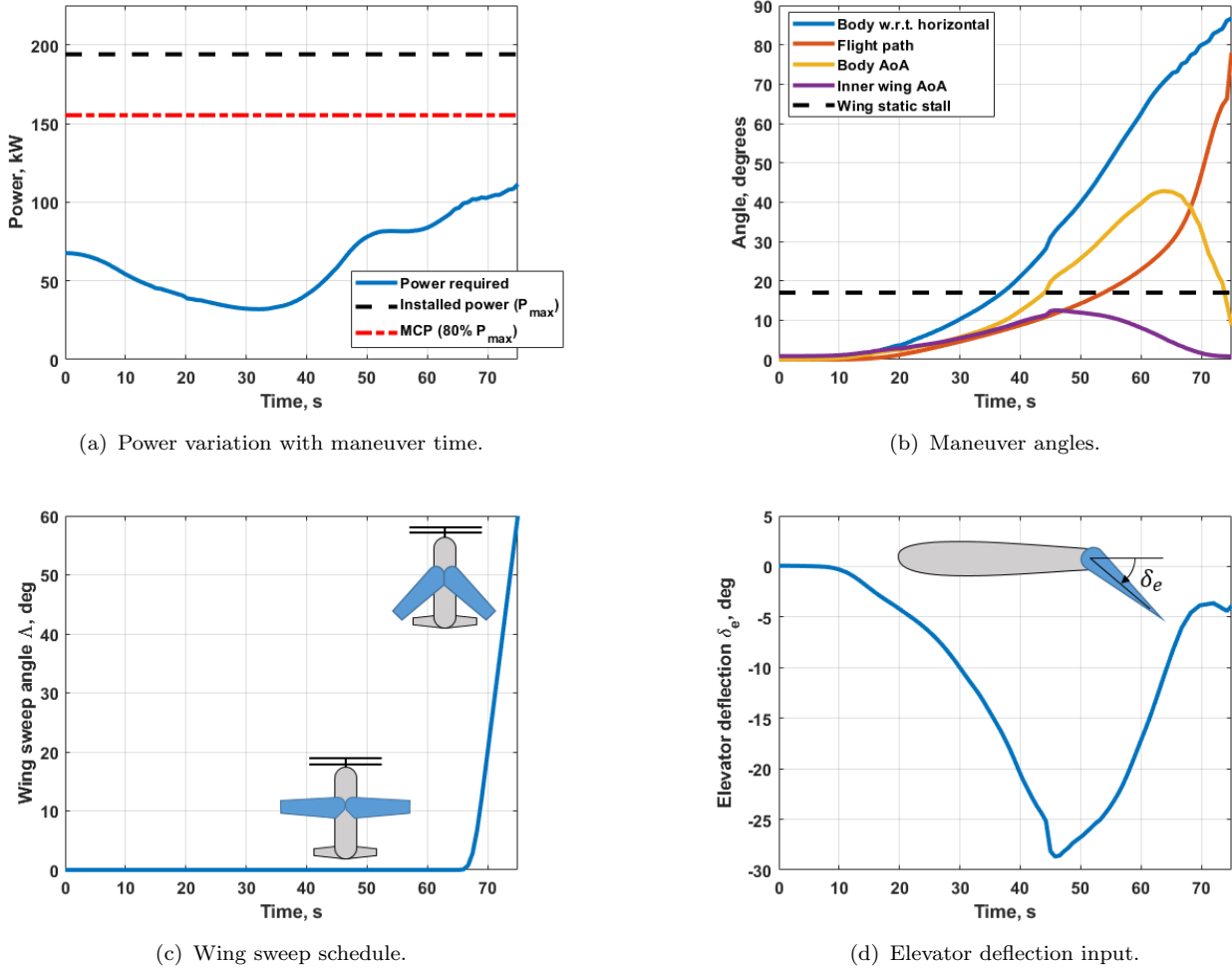


FIGURE 14.10: Description of the inbound climbing transition maneuver for $T = 75s$.

14.2.5.3 Effect of Cruise-to-Hover Transition Time

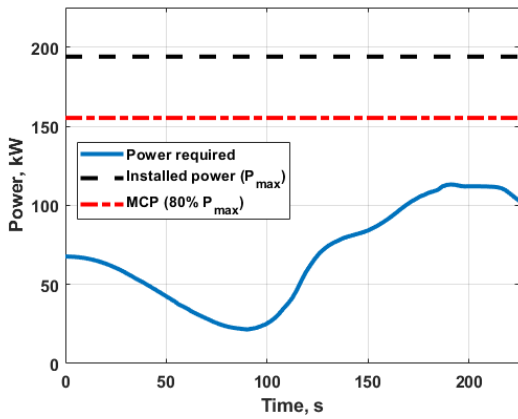
The effect of total maneuver time for the cruise-to-hover transition is shown in Figure 14.12(a) for the climbing profile and Figure 14.12(b) for the level profile. Unlike in the hover-to-cruise transition, a shorter cruise-to-hover maneuver requires less power. The shortest possible time is dictated by the need to avoid absorbing power into the rotor.

The slow climbing profile requires a greater power than the slow level flight profile, due to the power absorbed by gaining altitude. As such, the climbing profile has a larger margin by which the power can be decreased before reaching zero, allowing for a shorter maneuver time than the level profile.

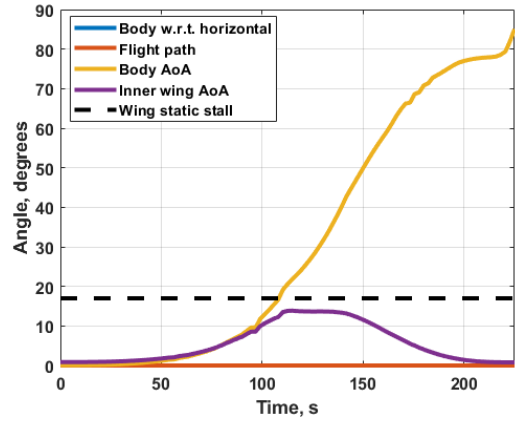
14.3 Control System

The *Metaltail* control system operates in three main modes: (1) hover, (2) transition, and (3) cruise. Each mode utilizes the typical 12-state representation of flight dynamics for a full-sized aerial vehicle with position tracking: $[x, y, z, u, v, w, \phi, \theta, \psi, p, q, r]$, where $x, y,$ and z are translational displacements, $u, v,$ and w are translational velocities, $\phi, \theta,$ and ψ are rotational angles, and $p, q,$ and r are rotational rates. At various flight stages, *Metaltail* is linearized to

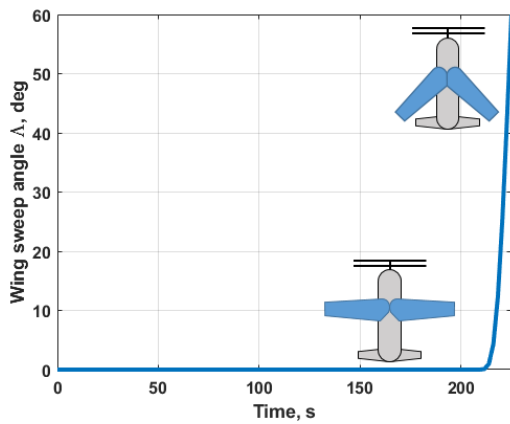




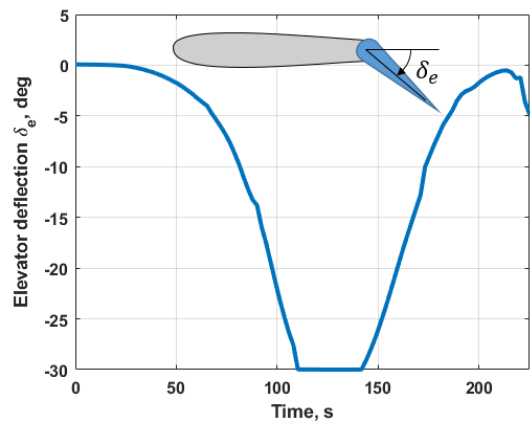
(a) Power variation with maneuver time.



(b) Maneuver angles.

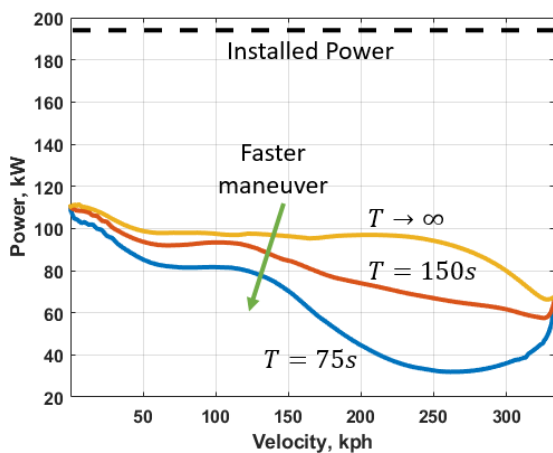


(c) Wing sweep schedule.

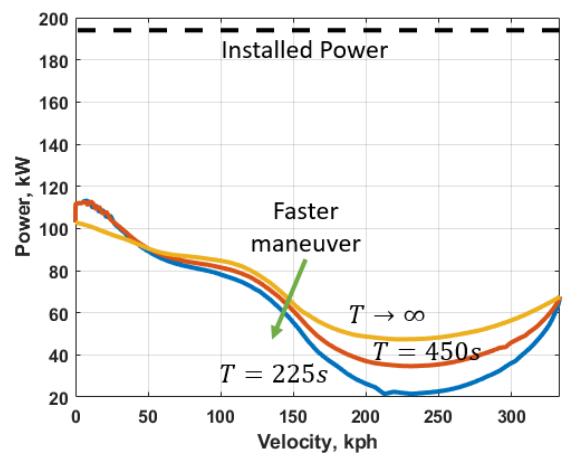


(d) Elevator deflection input.

FIGURE 14.11: Description of the inbound level transition maneuver for $T = 225s$.



(a) Climbing profile.



(b) Level profile.

FIGURE 14.12: Power variation with total maneuver time for different cruise-to-hover transition profiles.



determine Linear Quadratic Regulator (LQR) optimal infinite-horizon, continuous-time gains. LQR gains minimize the following cost function based off of preferential magnitudes for control input and vehicle state. This is useful for sensitive control systems to minimize control input and for non-robust vehicle dynamical systems to minimize vehicle state error.

$$J = \int_0^{\infty} (x^T Q x + u^T R u + 2x^T N u) dt$$

For normal operating conditions, *Metaltail* is an overactuated system. Control surfaces are defined by rotor cyclic, rotor collective, swept-wing ailerons, swept-wing sweep angle, and tail surface ailerons. In hover flight, *Metaltail* is controllable through synchronized rotor cyclic and independent rotor collective commands. Rotor cyclics provide lateral and longitudinal movement, and rotor collective controls vertical movement. In cruise flight, *Metaltail* is controllable through wing aileron deflections. Main wing ailerons control ϕ . Tail wing ailerons control θ, ψ . In forward transition, the main wing sweeps forward to increase span and provide greater authority. In reverse transition, the main wing sweeps back. The transition flight region provides appropriate control mixing, refined by control surface effectiveness at each condition. Initially, mixing is done mode-by-mode with modification of the LQR Q matrix.

14.3.1 Autonomous Control and Navigation

14.3.1.1 Control

The *Metaltail* autonomous controller begins as a deep reinforcement network (Deep Q-Learning) trained on minimizing error with a set of LQR gain controllers. Almost all autonomy is based simply on “discovery” driven by collection of facts from a myriad of sensors. *Metaltail* tries “cognition”, i.e. an attempt to understand context of disturbances and its environment (see Fig. 14.13). Deep Q-Learning is chosen because it is reliable and has been shown to converge to the optimal POMDP solution by the Bellman Optimality Equation for a given well-defined problem. This characteristic of Deep Q-Learning is known as artificial general intelligence. The neural network structure is analogous to the typical control structures for determining input or control law u , and plant G . Control law generator uses vehicle state, world model, and goal location to predict actuator output. Control law generator is updated to reward low-energy movements towards the next setpoint. Plant predictor takes in current state, world model, and current input to determine vehicle response. Plant predictor is trained to minimize error between predicted state and sensor-based determination of state at the next state estimation step.

14.3.1.2 Path-Planning

Metaltail movement planning integrates directly with Avionics and HUMS, thus creating adaptive and context-sensitive vehicle reactions. The movement planning model is an automated meta-planner for forward simulating flight and tuning parameters related to *Metaltail*'s control and navigation. Key problems associated with Deep Q-Learning are: 1. Training data has high variance, 2. Gradient descent on a deep neural network is extremely slow, and 3. Certain events usually occur infrequently making learning uncertain. The movement planning model uses techniques such as forward simulation, experience replay, and double-DQL training in order to continually achieve better performance even in contingency scenarios such as autorotation and power loss.



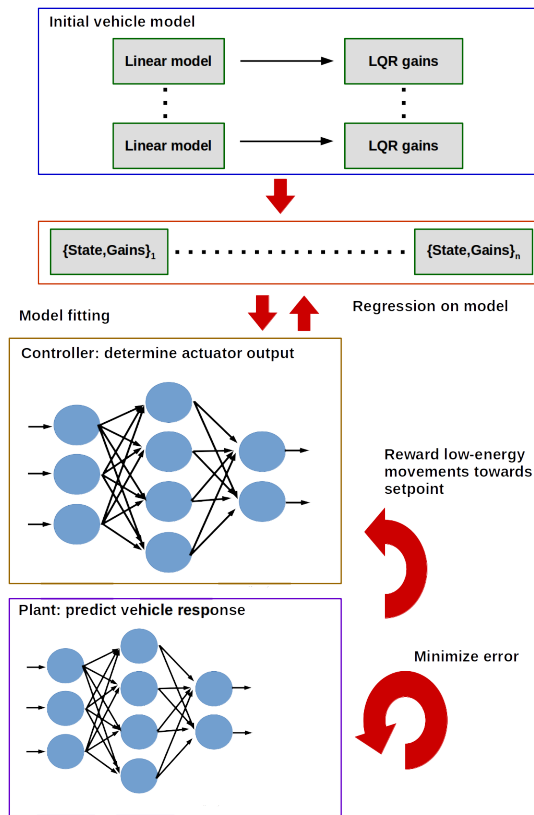


FIGURE 14.13: Deep Q-Learning control law generator and plant predictor.

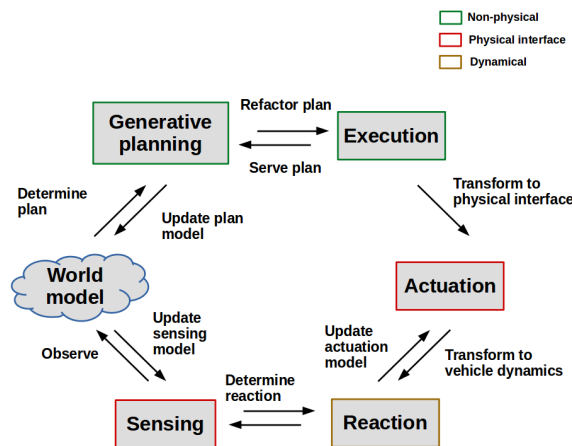


FIGURE 14.14: Cycle of autonomous planning showing six-system environment model. Non-physical systems (green) are entirely software. Physical interfaces (red) transform software-generated data into physical movement. Dynamical system (yellow) is true physical motion. World model is a mapping of salient environment states.



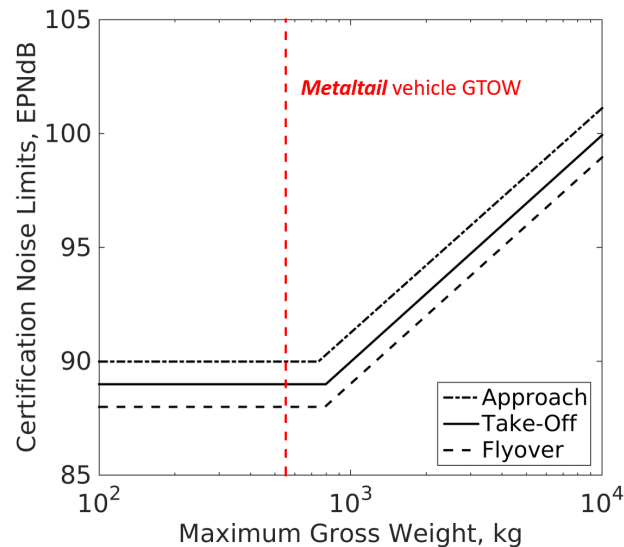


FIGURE 15.1: FAA tiltrotor noise limits (Extrapolated from FAR 36.1103).

15 Acoustics

Metaltail is designed for operation in a megacity-type environment, where noise restrictions may apply. Therefore it is important to consider the acoustic signature of *Metaltail* to ensure safe and comfortable environment for those that may come in contact with the aircraft. Noise produced by an aircraft is generated from various sources which include but are not limited to main rotor, transmission and engine.

15.1 FAA Noise Requirement

Currently there are no specific Federal Aviation Administration (FAA) noise regulations imposed on tail-sitters. However, because the operation of *Metaltail* rotors is similar to that of a tiltrotor, tiltrotor noise restrictions will be considered. The maximum noise limit for a tiltrotor as a function of the maximum gross weight is shown in Fig. 15.1. The limit for a 552 kg aircraft is a range between 88 and 90 EPNdB (Effective Perceived Noise Level in decibels), depending on the flight regime of the aircraft.

15.2 Noise Assessment

The noise levels of *Metaltail* main rotor were analyzed using an in-house acoustic analysis based on Ffowcs-Williams-Hawkins equations, using Farassat formulation 1A [16], [17]. The thickness and loading noises were calculated for each of the rotors. Thickness noise, which is a function of blade thickness and deflection, is a result of the displacement of air due to blade movement. Thickness noise propagates in the rotor plane. The loading noise is due to the aerodynamic loading, normal and chordwise forces, on the blade. The noise from each rotor was then superimposed to obtain the noise levels for the coaxial configuration.

In accordance with the FAA standards, the sound pressure levels (SPL) were calculated for hover and cruise conditions, 150 meters below the aircraft, in a circle with 150 meter radius. Table 15.1 summarizes the maximum noise levels on the circular plane of a 150 meter radius, 150 meters below the aircraft. Figure 15.2 shows the noise levels on a hemispherical surface with a radius of



150 meters and a plane located 150 meters below the aircraft. The thickness noise is maximum in rotor plane, for hover and cruise. Even though the blade loading is lower in cruise, the loading noise is higher due to the high chordwise loading in the cruise condition. Because the thickness noise is dependent on the deflection of the blade, as well as the airfoil thickness, the thickness noise in cruise is higher due to higher deflections. The low noise levels of *Metaltail* in both hover and cruise, are in accordance with the FAA standards and suitable for urban environment operations.

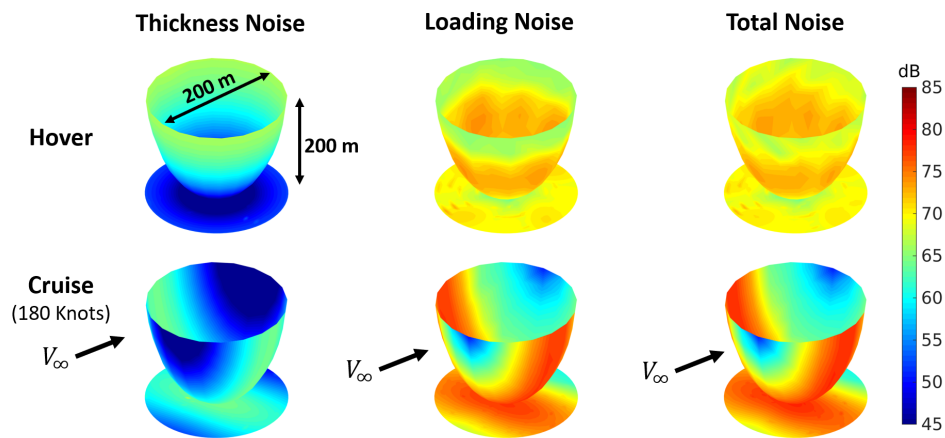


FIGURE 15.2: Noise levels for Metaltail in hover and cruise.

TABLE 15.1: Maximum noise level on the ground plane, 150 meters below the aircraft.

Noise, dB	Hover	Cruise
Thickness	48.59	58.24
Loading	71.74	72.26
Total	71.69	72.28

16 Vehicle Performance

Metaltail is designed to have a higher top speed than both helicopters and conventional fixed-wing aircraft in its weight class, while still being able to hover, take off, and land vertically as a helicopter. As a fixed-wing aircraft in cruise, *Metaltail* saves power and fuel by supporting its weight on an aerodynamically efficient wing. *Metaltail* is able to swing its wings backwards in helicopter mode, ensuring that it is able to operate as a helicopter in confined spaces. Reducing the span of the wing in hover allows the use of a more efficient wing than would be possible if the wing was fixed with a reduced span.

The performance of *Metaltail* is examined for several flight regimes. As will be shown, *Metaltail* succeeds in having high performance, particularly in cruise but also in hover, while meeting the stated weight and dimensional requirements.

16.1 Drag Estimation

For accurate calculation of *Metaltail's* forward flight performance, a reasonable estimation of the drag acting on the vehicle is required. To estimate the total vehicle drag, the drag of each component is calculated, then the total drag is calculated as the sum of that of the components.

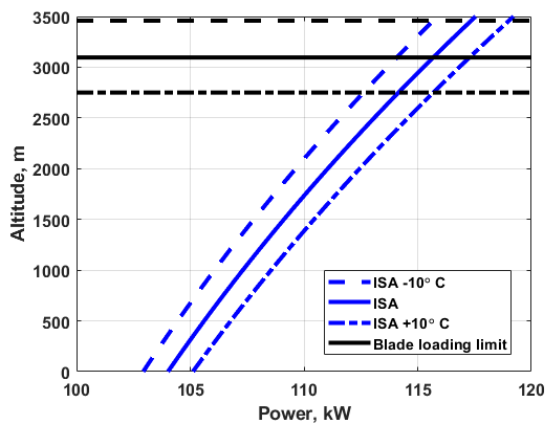
The drag of the wing is a simple calculation. Through the performance methodology, the angle of attack of the wing is known, as well as the lift being generated. The profile drag is calculated by performing a table lookup on airfoil data gathered through experimentation, and applying the sectional drag coefficient to the wing planform. The induced drag due to lift is also calculated, with an assumed Oswald efficiency of $e = 0.8$. The total drag of the wing is calculated as the sum of the profile and induced drag. The same calculation is also performed for the tail, using the appropriate airfoil tables.

The variation of the fuselage and rotor spinner drag with angle of attack is necessarily important to *Metaltail*, as it has a large angular range of motion. Moving horizontally in the vertical orientation, the fuselage is modeled as a cylinder with appropriate height and diameter, for which the equivalent drag area is known. For forward flight, where the vehicle is in a horizontal orientation, the drag is built up by discretizing the fuselage into segments, then calculating the drag for each segment. An additional form factor correction is applied, based on the shape of the fuselage. Finally, it is assumed that the boundary layer is fully turbulent. In between the vertical and horizontal orientations, the two values of drag area are blended to produce an estimation of the actual drag.

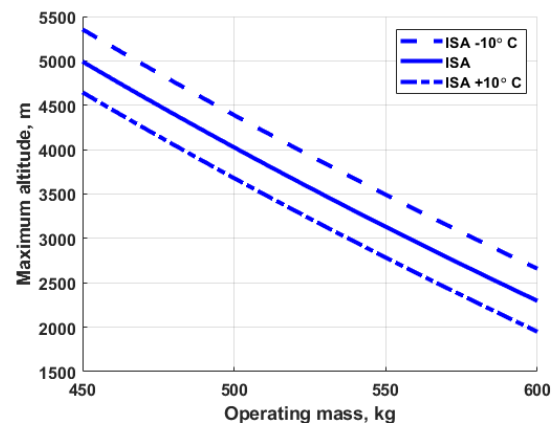
16.1.1 Download Penalty

In any helicopter, some thrust is lost due to the drag created by the rotor downwash interacting with the vehicle. Compared to a tiltrotor, *Metaltail's* tailsitter configuration offers a much lower penalty, because its wings remained aligned with the rotor wake flow in both hover and cruise. Additionally, the use of a monoplane wing eliminates the drag from structural supports typical of multiplane wings. The bulk of the download penalty thus comes from the fuselage drag.

16.2 Hover Performance



(a) Power required for hover at MTOW.



(b) Hover ceiling for different vehicle weights.

FIGURE 16.1: Effect of altitude and mass on hover performance.



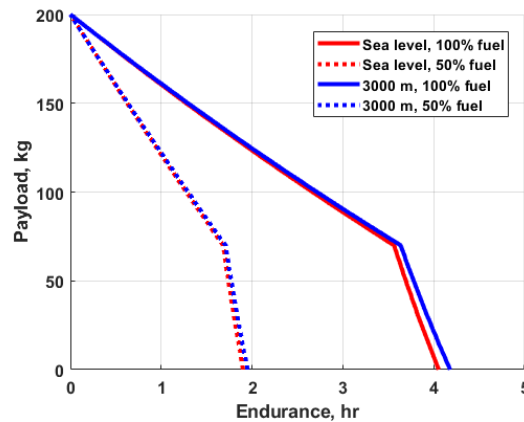


FIGURE 16.2: Hover endurance variation with payload and altitude

Metaltail is designed to be efficient in hover, despite the requirement that it fit within a 3 meter span, limiting the size of its rotor compared to other vehicles of a similar weight. With 194 kW installed power, *Metaltail* has a significant power margin in hover. However, the rotor's constrained area means that *Metaltail* experiences a high C_T in hover, and thus a higher than historically average blade loading. The requirement that $C_T/\sigma < 0.16$, rather than the installed power, limits the altitude at which *Metaltail* can hover (Fig. 16.1(a)). However, *Metaltail* is still able to achieve hover at MTOW at 3000 m altitude, with a ceiling of 3100 m under standard conditions.

If it is required that *Metaltail* hover at an altitude greater than 3000 m, the payload or fuel load may be reduced. The combined weight of full fuel and payload is approximately 200 kg (36% of the 552 kg MTOW), giving significant operational flexibility. Reducing the useful load to 100 kg (for a total mass of 452 kg) allows *Metaltail* to hover at up to 5000 m altitude (Fig. 16.1(b)).

The hover endurance of *Metaltail* in hover is shown at both sea level and 3000 m altitude in Figure 16.2. The basic mission for *Metaltail* assumes a 100 kg payload, and 100 kg of fuel, although the fuel tank is sized for a maximum capacity of 130 kg. Trading payload for fuel (or reducing total weight once the fuel tanks are full) allows a hover endurance of up to 4 hours, giving *Metaltail* the flexibility to carry out hover-dominated missions, in addition to its high-speed missions. All hover calculations were done out of ground effect.

16.3 Forward Flight Performance

A major advantage of *Metaltail* over conventional helicopters is its ability to transition to horizontal flight, and operate as an airplane for higher speeds and greater cruise efficiency. Doing so allows *Metaltail* to have a maximum flight speed of 454 kph at sea level or 511 kph at 3000 m altitude, well in excess of the required 333 kph. A summary of *Metaltail*'s optimum speeds are presented below in Table 16.1.

At low forward flight speed, *Metaltail* acts as a helicopter in edgewise flow. As the vehicle moves faster, it transitions to horizontal wing-borne) flight, completing its transition by the time it reaches 140 kph. The power plot shown in Figure 16.3(a) reflects *Metaltail* moving along a horizontal flight path, without accelerating. The vehicle is capable of trim in any intermediate state, and so the power curve is fully defined. The effect of different flight paths and accelerations on the transitional flight phase are examined in Chapter 14.



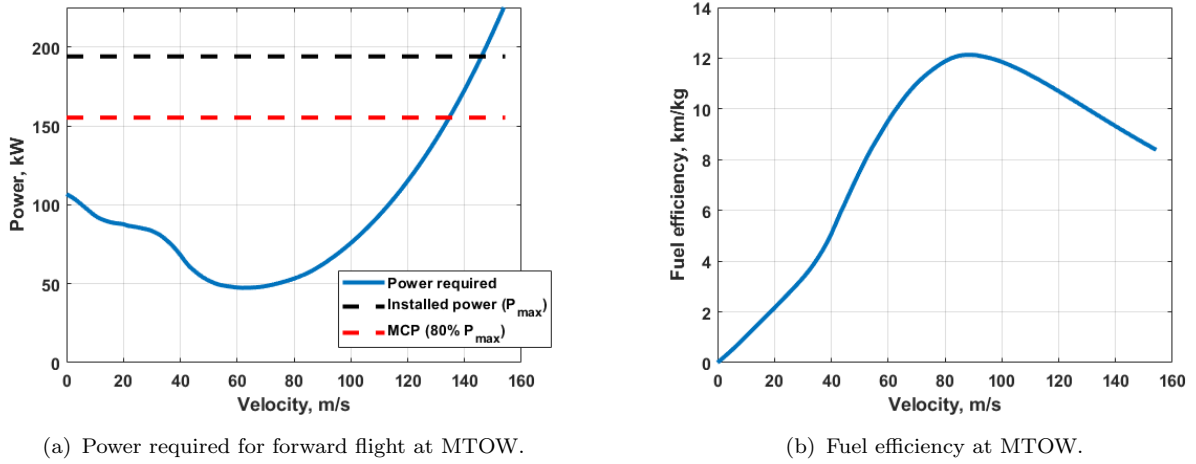


FIGURE 16.3: Effect of speed on forward flight performance at 3000 m altitude.

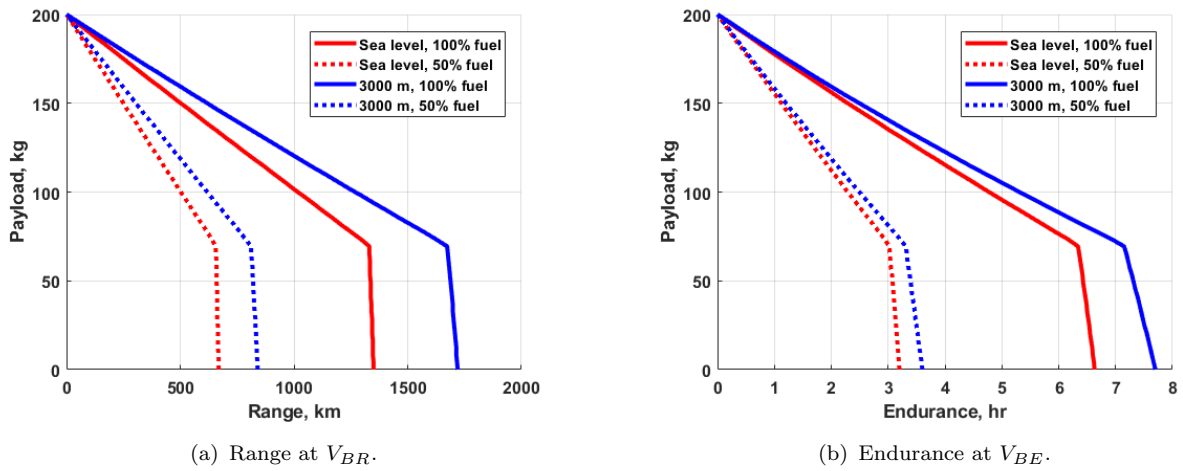


FIGURE 16.4: Range and endurance achievable by *Metaltail*.

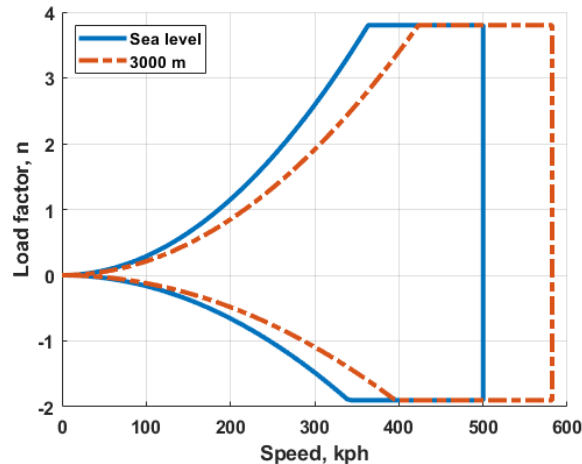
Compared to hover, the thrust required in forward flight is lower, so the limitation on forward speed is based on installed power rather than blade loading. *Metaltail's* two engines give the vehicle an installed power of 194 kW, of which 80% is taken as the maximum continuous power. The full power of the engines may be used for up to 5 minutes at a time, for takeoff and other intensive maneuvers. The Stuttgart STV 130 engine is flat-rated up to an altitude of 10,000 m (33,000 ft), so is effectively fixed for *Metaltail's* operating altitudes.

The velocity for best endurance is defined as the velocity for minimum power required, which for *Metaltail* occurs at 222 kph. Because the fuel consumption of the engines varies with altitude and power setting however, it is necessary to examine *Metaltail's* fuel economy to find its velocity for best range. Figure 16.3(b) shows the fuel economy in km/kg for the vehicle's operating speeds. The maximum value is approximately 12 km/kg, which occurs at a speed of 311 kph. Of note, at *Metaltail's* maximum speed, its fuel economy is still greater than 75% of its best fuel economy, meaning that operating at a faster speed is possible with only a modest loss in mission range.



TABLE 16.1: Summary of *Metaltail* airspeeds at 3000 m altitude.

Symbol	Description	Set By	Value (kph)
V_{BE}	Best endurance	Minimum power	222
V_{BR}	Best range	Best fuel efficiency	311
$V_{cr,max}$	Max sustained cruise speed	MCP	471
V_{max}	Maximum level flight speed	Installed power	511

FIGURE 16.5: *Metaltail* V-N diagram.

16.4 Load Factor

The operating envelope for *Metaltail* is shown in Figure 16.5. The vehicle is capable of +3.8 g and -1.9 g maneuvers, and the structure is designed to ensure that the vehicle may exceed V_{max} in a dive if necessary. At lower speeds, *Metaltail's* maneuvering envelope is limited by wing stall.

16.5 Performance Metrics

A summary of *Metaltail's* performance metrics is presented in Table 16.2. All metrics reflect an initial takeoff mass of 552 kg, including 100 kg of payload and 100 kg of fuel, for a typical mission. *Metaltail* achieves excellent speed and range compared to similarly-sized fixed and rotary wing vehicles, while still maintaining the ability to operate as a conventional helicopter, with reasonable hover endurance.

17 Life-Cycle Cost Analysis

Based on NDARC theory, the total cost of the *Metaltail* aircraft is broken down into two major categories: (i) the purchase price, and (ii) the direct operating cost (DOC)[3]. The total life cycle cost is the sum of each of these two elements. The aircraft purchase price covers airframe, mission equipment package (MEP), and flight control electronics (FCE) costs. The direct operating cost (DOC) is the sum of maintenance cost, fuel and oil cost, depreciation, insurance cost, and finance cost. Inflation factors were used to calculate the expected production costs of *Metaltail* in 2018 USD. As *Metaltail* is developed using proven technologies with TRL of 6 or higher, further developments are not required, and therefore the cost estimate is expected to be conservative.



TABLE 16.2: Summary of *Metaltail* performance metrics.

Metric	Conditions	<i>Metaltail</i> Value	Units
Hover time using 50% fuel	SLS	1.275	hours
	3000 m	1.295	
Cruise range at V_{BR} using 50% fuel	SLS	502	km
	3000 m	619	
Dash speed (V_{max})	SLS	454	kph
	3000 m	511	
Drag area at V_{max}	SLS	0.1303	m ²
	3000 m	0.1306	

17.1 Aircraft Purchase Price

Purchase price is based on Harris and Scully [3]. which uses a function of aircraft weight and power; has several complexity factors; a factor for rotorcraft or turboprop aircraft; and a country or industry factor (specifically U.S. military). The model includes separate calculations of a composite construction increment, mission equipment package cost, and flight control electronics cost. The model accounts for inflation and includes an overall technology factor. With these equations, the purchase price is predicted within 20% for 96% of 128 rotorcraft, a standard deviation of 10%.

The equation for aircraft purchase price is:

$$C_{AC} = \chi_{AF}(F_i c_{AF}) + C_{MEP} + C_{FCE} \quad (17.1)$$

Where χ_{AF} is the calibration and industry factor; $\chi_{AF} = 0.87$ for U.S. Military. F_i is the inflation factor; based on 1994 dollars, $F_i = 1.6839$ for 2018. C_{MEP} and C_{FCE} are cost of mission equipment packages and cost of flight control electronics, respectively, displayed in Table 17.1. c_{AF} is the airframe purchase price:

$$c_{AF} = 739.91 K_{ET} K_{EN} K_{LG} K_R W_{AF}^{1.0619} (P/W_{AF})^{0.5887} N_b^{0.1465} \quad (17.2)$$

Where $K_{ET} K_{EN} K_{LG} K_R$ is the configuration factor, W_{AF} is the airframe weight, P is the rated takeoff power for all engines, and N_b is the number of blades per rotor. All values are compiled in Table 17.1.

The total aircraft purchase price is **869,281.62 USD**.

17.2 Direct Operating Cost

The direct operating cost includes maintenance, fuel, depreciation, insurance, and finance costs. The equation for estimating this quantity is:

$$C_{OP} = T_F C_{maint} + C_{fuel} + C_{dep} + C_{ins} + C_{fin} \quad (17.3)$$

Where T_F is the estimated flight hours per year, C_{maint} is the estimated maintenance cost per flight hour, C_{fuel} is the cost of fuel, C_{dep} is the depreciation cost, C_{ins} is the insurance cost, and C_{fin} is the finance cost.



TABLE 17.1: Parameters used to calculate aircraft purchase price.

Parameter	Unit	Value
K_{ET}	1 for turbine 0.557 for piston	1
K_{EN}	1 for multi-engine 0.736 for single-engine	1
K_{LG}	1 for retractable landing gear 0.884 for fixed landing gear	0.884
K_R	1 for single main rotor 1.057 for twin rotor 1.117 for quad rotor	1.057
W_{AF}	Airframe weight (kg)	196
P	Max takeoff power (kW) (all engines)	194
N_b	Number of blades	4
χ_{AF}	Industry factor	1
F_i	Inflation Ratio based on 1994	1.6839
C_{MEP}	Mission equipment package cost (USD in thousands)	37.4
C_{FCE}	Flight control equipment cost (USD in thousands)	167
C_{AC}	Total aircraft purchase cost (USD in thousands)	869.28

TABLE 17.2: Parameters used to calculate direct operating costs per year.

Parameter	Unit	Value
T_F	Flight hours per year	450
C_{maint}	Maintenance cost per flight hour (USD)	119.69
C_{fuel}	Average cost of fuel per year (USD in thousands)	31.2
C_{dep}	Depreciation per year (USD in thousands)	58.7
C_{ins}	0.56% of C_{AC} per year (USD in thousands)	4.9
C_{fin}	Finance cost per year (USD)	400.96
C_{OP}	Total operating cost per year (USD in thousands)	149.02

Based on the upper range of EMS helicopter usage, $T_F = 450$ flight hours per year, as shown in Table 17.2. All other costs are shown as per year operating cost.

The total cost of *Metaltail* for the first year is the sum of aircraft's purchase price and its operating cost, resulting in **1,018,300.59 USD**. For an estimated twenty years of service, the total cost will amount to **3,849,661.02 USD**, averaging **192,483.05 USD** a year. These calculations were purposefully made to be conservative with no change in industry factor from 1994, high depreciation per year for twenty years, and a high number of flight hours per year resulting in high maintenance costs. Another factor contributing to this low price is the absence of a pilot and any crew.



18 Summary

The University of Maryland Graduate Team has designed *Metaltail*, a novel approach on the implementation of swing wing technology, to meet all of the vehicle and operational requirements specified in the Request for Proposal for a Reconfigurable VTOL Aircraft for the 2018 AHS International Student Design Competition. *Metaltail* is designed to exploit its reconfigurable system to convert to a high aspect ratio high wing in high speed forward flight.

- Novel swing wing design reverses conventional practice and leverages the compactness in hover, control authority in transition, and high lift in forward flight that a sweeping wing provides.
- Advanced blade aerodynamics allow for multipurpose rotor, boasting high efficiency in hover with FM of 0.77 and high propeller efficiency of 0.83.
- Unique hingeless rotor hub places the upper swashplate within the rotor shaft, resulting in an uncharacteristically compact coaxial rotor.
- Dual turboshaft engines provides system redundancy, low specific fuel consumption, and exceptional power for Group 3 class aircraft.
- Cutting edge avionics supply *Metaltail* with 360° awareness and enhanced operability in degraded conditions.



Bibliography

- [1] Donate Life, “Donate Life America Statistics,” 2018, <https://www.donatelife.net/statistics/>.
- [2] Tischenko, M. N., Nagaraj, V., and Chopra, I., “Preliminary Design of Transport Helicopters,” *Journal of AHS*, Vol. 48, No. 2, Apr. 2003, pp. 71–s79.
- [3] Johnson, W., “NDARC NASA Design and Analysis of Rotorcraft,” Tech. Rep. 2015-218751, NASA, Oct. 2016.
- [4] Chappell, D. and Peyrau, R., “Methodology for Estimating Wing Weights for Conceptual Tilt-Rotor and Tilt-Wing Aircraft,” *Society of Allied Weight Engineers 51st Annual Conference*, 1992.
- [5] Dadone, L., Liu, J., Wilkerson, J., and Acree, C., “Proprotor Design Issues for High Speed Tiltrotors,” *American Helicopter Society 50th Annual Forum, Washington, DC*, 1994.
- [6] Johnson, W., Lau, B. H., and Bowles, J. V., “Calculated performance, stability and maneuverability of high-speed tilting-prop-rotor aircraft,” 1986.
- [7] Paisley, D. J., “Rotor aerodynamic optimization for high speed tiltrotors,” *AHS, Annual Forum, 43 rd, Saint Louis, MO, Proceedings.*, Vol. 1, 1987, pp. 301–310.
- [8] Bamsey, I., “Small but Perfectly Formed,” *Unmanned Systems Technology*, Vol. 11, Dec. 2017, pp. 50–61, <https://www.ust-media.com/ust-magazine/UST011/>.
- [9] Saribay, Z. B., “Analytical Investigation of the Pericyclic Variable-Speed Transmission System for Helicopter Main-Gearbox,” Phd dissertation, Pennsylvania State University, 2009.
- [10] Bradley, M. K. and Droney, C. K., “Subsonic Ultra Green Aircraft Research: Phase II - Volume II - Hybrid Electric Design Exploration,” Tech. Rep. 2015-218704, NASA, Apr. 2015.
- [11] “Fundamental Rating Factors and Calculation Methods for Involute Spur and Helical Gear Teeth,” Standard, American Gear Manufacturers Association, Alexandria, VA, Dec. 2004.
- [12] “Geometry Factors for Determining the Pitting Resistance and Bending Strength of Spur, Helical and Herringbone Gear Teeth,” Standard, American Gear Manufacturers Association, Alexandria, VA, Apr. 1989.
- [13] Radzevich, S. P., *Dudley’s Handbook of Practical Gear Design and Manufacture*, Taylor & Francis Group, Boca Raton, FL, 2012.
- [14] Command, U. A. M., *AMC Pamphlet AMCP 706-202: Engineering Design Handbook. Helicopter Engineering. Part Two, Detail Design*, Alexandria, VA, 1976.
- [15] Command, U. A. M., *AMC Pamphlet AMCP 706-202: Engineering Design Handbook. Helicopter Engineering. Part One, Preliminary Design*, Alexandria, VA, 1974.
- [16] Williams, J. F. and Hawkings, D. L., “Sound generation by turbulence and surfaces in arbitrary motion,” *Phil. Trans. R. Soc. Lond. A*, Vol. 264, No. 1151, 1969, pp. 321–342.



- [17] Farassat, F., “Linear acoustic formulas for calculation of rotating blade noise,” *AIAA journal*, Vol. 19, No. 9, 1981, pp. 1122–1130.

